

学位論文

Ion Acceleration around Quasi-Parallel Bow Shock

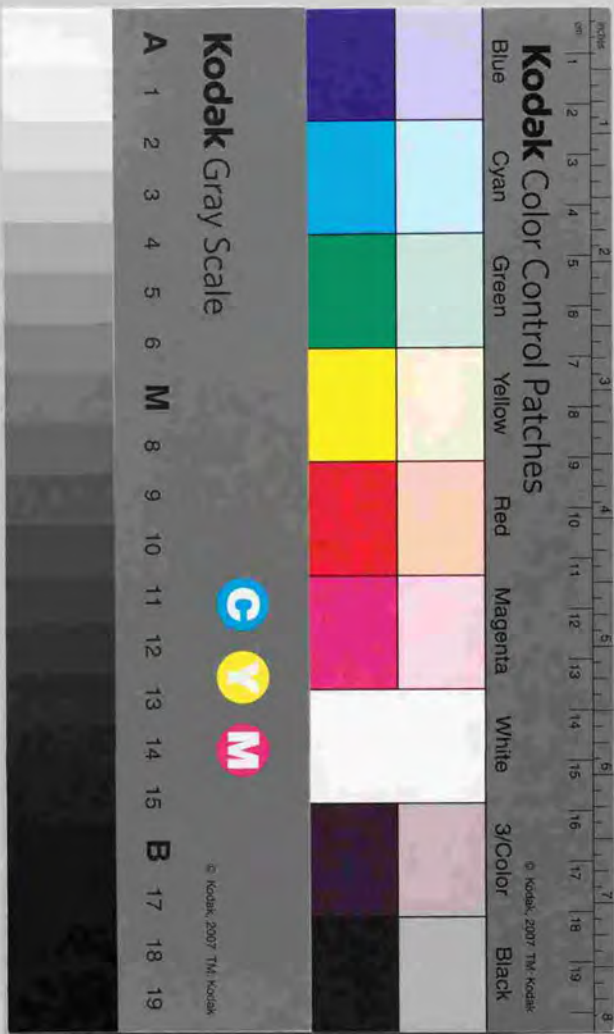
準平行衝撃波の近傍におけるイオンの加速

平成9年12月博士(理学)申請

東京大学大学院理学系研究科

地球惑星物理学専攻

杉山 徹



①

Doctor Thesis

Ion Acceleration around Quasi-Parallel Bow Shock

学位論文

準平行衝撃波の近傍におけるイオンの加速

Department of Earth and Planetary Physics
Graduate School of Science
University of Tokyo

Sugiyama, Tooru
December 1997

平成9年12月 博士(理学)申請

東京大学大学院理学系研究科
地球惑星物理学専攻

杉山 徹

Acknowledgments

I wish to express my hearty thanks to Prof. T. Terasawa for his continual guidance and stimulating supervision. Without his guidance, this work would have been all but impossible.

I also wish to express my deep appreciation to Prof. T. Mukai, Dr. M. Fujimoto, Dr. M. Hoshino and Dr. T. Hada for their valuable comments and discussions, to late Prof. T. Yamamoto and other GEOTAIL science members for providing the data.

I am most grateful to the staffs and colleagues associated with the Univ. of Tokyo and ISAS. They colleagues have been a significant contribution to the completion of this dissertation.

I thank to my father and mother for their encouragement, to my wife Harue for her mental and financial supports.

This work was supported by the Fellowships of the Japan Society for the Promotion of Science for Japanese Junior Scientists.

Abstract

Nonthermal particle acceleration processes at collisionless shocks have been widely discussed in the space physical as well as astrophysical communities. In this dissertation, we discuss physical processes around quasi-parallel/parallel collisionless shocks, especially the particle acceleration/scattering processes occurring at the earth's bow shock and its upstream region. From a comparison between in situ observations of the bow shock and an extensive numerical modeling, we present, (1) a new aspect for the interaction process between the energetic upstream ions and large amplitude magnetohydrodynamic waves, (2) an identification of a new prompt acceleration mechanism for thermal/nonthermal ions working at the shock front into which coherent large amplitude upstream waves are convected, and (3) confirmation of the above new ideas by making self-consistent hybrid simulations.

The prompt acceleration mechanism found in this dissertation can contribute to solve the "injection problem" which relates to an important question, how to produce nonthermal ions from thermal ions at astrophysical shocks.

The configuration of this dissertation is described below.

Chapter 1 gives a general introduction to the study of collisionless shocks and related particle acceleration processes.

Chapter 2 first gives an observational summary for the characteristic features of energetic ions in the bow shock upstream region, such as spatial distributions, energy spectra, and pitch angle distributions. It is shown that these ions most often show an anisotropic pitch angle distribution, occupying only the pitch angle hemisphere in the escaping direction from the shock front. Secondly, this peculiar pitch angle distribution is explained in terms of the nonlinear trapping motions of ions in nearly-monochromatic large amplitude MHD waves. A quantitative comparison between this nonlinear process and the standard quasi-linear pitch angle scattering process is also given.

In Chapter 3, trapping motions of ions in large amplitude MHD waves are further considered in the region surrounding the front of parallel shocks. It is found that ion motions depend not only on their initial pitch angle but also on their initial gyrophase angles, and that some of ions

can be accelerated promptly up to the velocity of $\sim 10 - 20$ times of the upstream Alfvén velocity. This behavior of accelerated ions is explained in terms of the different propagation speeds of MHD waves between the upstream and downstream regions of the shock front. This new acceleration mechanism is found to work much faster than the standard diffusive shock acceleration mechanism does. While the ion motions in the former mechanism are governed by the deterministic trapping process in a large amplitude coherent MHD wave with a time scale less than a few gyroperiods, those in the latter are governed by the microscopic pitch angle scattering process in a wave field consisting of many incoherent MHD waves of small amplitude with a time scale of many gyroperiods.

In Chapter 4, we confirm the new finding in the earlier chapters which are mainly based on test particle considerations, by taking into account of the reaction of accelerated ions to the electromagnetic fields.

In Chapter 5, it is concluded that the results obtained in this dissertation provides a new development for the understanding of the ion injection process, which occurs as the first step of energetic particle acceleration processes at astrophysical shock waves.

Contents

Acknowledgments	i
Abstract	ii
1 General Introduction	1
2 Pitch Angle Distribution of Diffuse Ion in the Upstream Region of the Earth's Bow Shock	7
2.1 Introduction	7
2.2 Upstream Diffuse Ion Events from GEOTAIL Observations	12
2.2.1 The GEOTAIL Mission and Instrumentations	12
2.2.2 Event Selection	13
2.2.3 Flux Intensity and Energy Spectra	16
2.2.4 Pitch Angle Distribution	20
2.2.5 Summary of Observations	22
2.3 Pitch Angle Scattering in the Large Amplitude Alfvén Waves	24
2.3.1 Difficulties in Resonance Scattering Process	24
2.3.2 Basic Equation	26
2.3.3 Pitch Angle Scattering Motion	27
2.3.4 Ion Distribution Shape in Monochromatic Alfvén Waves	34
2.3.5 Summary of Simulation	40
2.4 Summary	41
3 Ion Motion around the Parallel Shock	43
3.1 Introduction	43
3.2 Basic Equation for Acceleration Process	45

Contents

3.3 Ion Acceleration around the Shock Discontinuity	48
3.4 Ion Reflection at the Shock Surface	55
3.5 Summary and Discussion	57
4 Quasi-Parallel Shock Simulations in Hybrid Code	63
4.1 Introduction	63
4.2 Hybrid Code Simulation	66
4.3 Results	67
4.3.1 Ion Reflection at the Shock and Origin of Upstream Ions	69
4.3.2 Particle Acceleration around the Shock	74
4.3.3 Particle Distribution in the Pitch Angle Space	80
4.3.4 Wave Steepening Phenomena and Distribution Type	84
4.4 Summary	91
5 Conclusion	93
A Diffusive Shock Acceleration Process	97
A.1 Diffusion Convection Equation	97
A.2 Particle Interaction with Alfvén Wave	98
B Phase Bunching Mechanism	101
C Rankine-Hugoniot Relations	103
D Setting for the Shock Transition Layer and Wave Transmission	105
D.1 Transition Layer	105
D.2 Transmission of Alfvén Waves through a Fast-Mode MHD Shock	106
References	109

Chapter 1

General Introduction

One of the most remarkable phenomena in collisionless space plasmas is the existence of non-thermal particles. Cosmic rays and solar flare particles are well-known examples. It is now understood that shock waves play the most important role for the effective production of the non-thermal particles. Non-thermal particles are also observed in the upstream of the terrestrial bow shock. Since the detailed features of the particle distribution can be studied from *m situ* observations, the bow shock is a good laboratory to test collisionless shock acceleration theories. The results obtained from the terrestrial bow shock observation contribute not only to solar terrestrial physics but also to astrophysical plasma physics.

Since the earth's magnetosphere is an obstacle for the super-magnetosonic solar wind flow, there exists a bow shock ahead of the magnetosphere. For the line shape of the interplanetary magnetic field (IMF), the bow shock geometry is illustrated in Fig. (1-1). After the discovery of the bow shock in '60s, the shock structure has been studied extensively. The averaged stand-off distance at the sub-solar point is about $15 R_e$ (R_e is earth radii) from the center of the earth, and the distance is determined by the solar wind parameters, that is, shock Mach number, IMF conditions and so on. The shock structure is classified to two categories by the IMF direction: (quasi-)parallel ($\theta_{bn} < 45^\circ$) and (quasi-)perpendicular ($\theta_{bn} > 45^\circ$) shocks, where θ_{bn} is an angle between the upstream magnetic field and the shock normal direction.

About thirty years ago, however, it was a matter of controversy whether collisionless shock wave exists or not. The solar wind has proved to have an enormous collision mean free path to be comparable to the distance from the earth to the sun (1 AU). Since the thickness of classical shocks was determined by collision mean free path, the rarity of collisions in the space plasma would preclude the existence of such shocks. Studies have been performed what processes replace the collision. Anomalous resistivity mechanisms (e.g. by ion-acoustic waves, lower

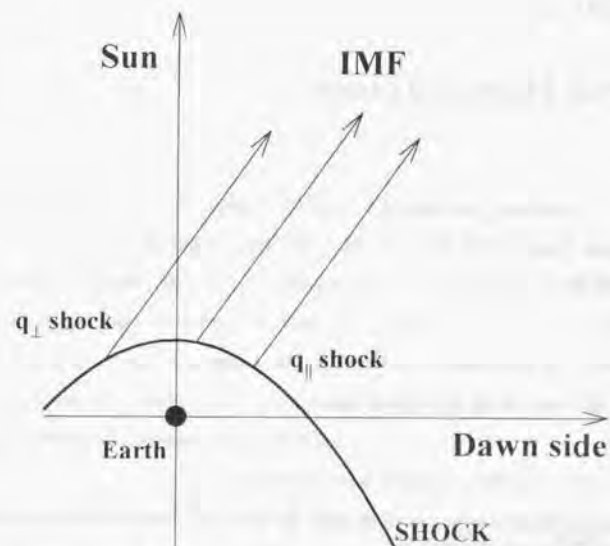


Figure 1-1. Schematic illustration of condition around the earth's bow shock. Sun is located top end. Collisionless MHD shock structures are mainly determined by the shock angle θ_{BV} : between shock normal and interplanetary magnetic field (IMF) direction. They are (quasi-)parallel (q : $\theta_{BV} < 45^\circ$) and (quasi-)perpendicular (q : $\theta_{BV} > 45^\circ$) shocks.

hybrid drift waves) solve the problem for low Mach number shocks. At high Mach number shocks, however, these mechanisms can not provide the required dissipation at the shock transition layer. Such a high Mach number shock is called a *supercritical shock*. The earth's bow shock is mainly in this category.

In late '70s to '80s, the good years to study the earth's bow shock by ISEE satellite series and numerical simulations, the dissipation mechanism for the supercritical shock is confirmed to be the particle-reflection process at the shock surface. A fraction of incoming solar wind ions is

specularly reflected, thermalized and transmitted to the downstream region. The motional electric field in the solar wind contributes the thermalization. The upward directing magnetic mirror force which comes from the magnetic field intensity compression at the shock surface, is considered as one of the components for particle reflection. At the large shock angle θ_{BV} regime, the force may act on the particles, but as θ_{BV} becomes smaller the force also becomes smaller because of weak field compression. How does a quasi-parallel shock reflect the solar wind ions? The observations show that the bow shock produces the specularly reflected ions even in the quasi-parallel shock. In the wide upstream region of the quasi-parallel bow shock, non-thermal particles have been detected. These ions have much higher energy than that of both the solar wind ions and the specularly reflected ions. After the existence of the reflected ions is shown by satellite observations, shock investigators change their interests from reflection process to acceleration process. The reflection processes have been remained unsolved. Recently, numerical simulations begin to re-investigate about the reflection process and propose that the upstream waves contribute the reflection process. Although it is found that the reflection mechanism is different from that of the quasi-perpendicular shock, the detail processes have not yet been clear because not only the mirror force decreases but also the reflection processes are concerned with the upstream wave activities.

After it is found that the shock not only produces the non-thermal particles but also accelerates them, collisionless MHD shocks have been considered as an accelerator for charged particles to high energy range in the two processes: scatter-free and statistical scattering process. In the former process called *shock drift acceleration* process (hereafter SDA process), particles gain energy near the shock surface by their drift owing to field gradient along the motional electric field. Since the electric field is caused under the condition where there is a finite angle between the magnetic field and the fluid velocity, this acceleration works mainly in a quasi-perpendicular shock. In the latter process called *diffusive shock acceleration* (hereafter DA process), particles are scattered in the wide region of the shock upstream/downstream and cross the shock surface many times. The elastic scattering process in the upstream region leads to acceleration in shock frame. Since the small shock angle enables the particles to cross easily the shock, this acceleration process has been mainly applied to a quasi-parallel shock.

For the DA process, the elastic scattering process is due to the small-angle pitch-angle

scattering by the cyclotron resonance with upstream/downstream waves. The anomalous resonance condition is described as $\omega_w = \Omega_i + k V_{\parallel}$, where ω_w , Ω_i , k and V_{\parallel} are wave frequency, ion cyclotron frequency, wave number and ion velocity parallel to the ambient magnetic field. The particles which are scattered back toward the shock can gain considerable energy in the shock frame. Under the assumption that ion distribution is isotropic in its pitch angle space, the diffusion-convection equation is treated to describe the ion transport. The observed spatial distribution and energy spectrum of the accelerated ion flux are well described by this equation. The observed wave power is also consistent with the prediction by the quasi-linear theory. Although the DA process has been shown to be consistent with the earth's bow shock acceleration process, it has not yet brought us the complete contentment in the following problems in pitch angle scattering process. First, the wave amplitude in the earth's bow shock is somewhat larger to treat the quasi-linear theory (the ratio of the wave amplitude to the ambient field intensity is over 0.5). Second, the waves are not observed in broad band frequency to satisfy the cyclotron resonance condition. The resonant particle velocity V_{\parallel} is restricted in a certain velocity determined by the narrow wave number k range, so that the isotropic distribution is not constructed. The satellite observations, however, have shown that the upstream non-thermal ions have nearly isotropic distribution. This suggests that the isotropic distribution is derived from another pitch-angle scattering process. If there is another scattering process, it is also suggested that there is another acceleration process because the DA process depends on the above resonant scattering process.

In this thesis we propose the importance of the large amplitude waves observed in the wide region around the quasi-parallel bow shock. The ion pitch angle diffusion motions in the large amplitude wave field are different from the motions from above resonant type interaction. Based on this concept, we re-consider the following three subjects in this thesis. (1) Pitch angle scattering process. (2) Reflection process of incoming solar wind ions at the shock surface. The importance of upstream waves for the reflection process has been proposed. And (3) ion acceleration process around the parallel shock.

In Chapter 2, we have made statistical study using the data from the plasma and magnetic field instruments from GEOTAIL satellite. The non-isotropic ion distribution observed in the

upstream region is the most remarkable subject. To investigate how the observational distributions are constructed, we have performed test particle simulations. The key motion is the *phase trapping*, that is, the phase angle between the wave and a particle's perpendicular velocity is restricted in a certain angle. Furthermore, we have investigated the pitch angle scattering process and found that the importance of the resonance type pitch angle scattering process is weak in the large amplitude wave field. This implies that in such a field the scatter-free process rather than the statistical scattering process should be considered as the dominant physical process.

In Chapter 3, from the scatter-free concept, it is also a good analytical method that individual particle trajectory is numerically calculated in a given shock transition layer. First, we propose a new acceleration mechanism by applying the above trapping process in the parallel shock region where the wave phase-velocity-discontinuity exists between the upstream and downstream region. The acceleration efficiency is better than DA process, for example, an ion energy increases about 10 times in the upstream Alfvén velocity unit within one gyro-motion interval. Next, we have investigated the reflection process of the incoming solar wind ions at the parallel shock surface, that is the "injection problem". The reflection process is explained by the ion motion in the large-amplitude monochromatic Alfvén wave.

In Chapter 4, to investigate the wave-particle interaction mechanism self-consistently we have performed numerical simulations in hybrid code. The above three important motions in the large-amplitude wave field have been detected in simulations as inherent process.

Chapter 2

Pitch Angle Distribution of Diffuse Ion in the Upstream Region of the Earth's Bow Shock

2.1 Introduction

Since the first discovery of the suprathermal ions of the earth's bow shock [Asbridge, 1968], the occurrence of the upstream ion events and related shock conditions have been discussed. The diffuse ion population is one of the suprathermal ion distributions, which is characterized by broad, nearly isotropic angular distribution and exponential energy spectrum extending up to ~100 keV. Fig. (2-1) shows an example of this type of upstream ion distribution [Paschmann *et al.*, 1981]. The left Panel shows the distribution in the form of count rate in two-dimensional velocity space in ecliptic plane. The tall sharp peak corresponds to the solar wind population and the broader lower peaks are the suprathermal diffuse ion population. The right Panel shows the same event in the iso-contour format of the phase space density in the same two-dimensional velocity space. The solar wind peak has been replaced by a dot to the right of the cross marking zero velocity in the satellite frame. Asterisk is the center of the broken circle. Sunward velocity lies to the left. The projection of the magnetic field on ecliptic plane is shown as an array through the solar wind dot. The distribution shows nearly isotropic around the magnetic field and including higher energy ions than solar wind ions.

There have been a number of statistical studies of the property of diffuse ion distribution and its relation to the shock condition [e.g. Ipavich *et al.*, 1981a; Bonifazi and Moreno, 1981a,b; Trattner *et al.*, 1994]. Diffuse ions are observed in the upstream region of a quasi-parallel shock where the shock angle θ_{DN} is small. Their intensity decreases exponentially from the shock

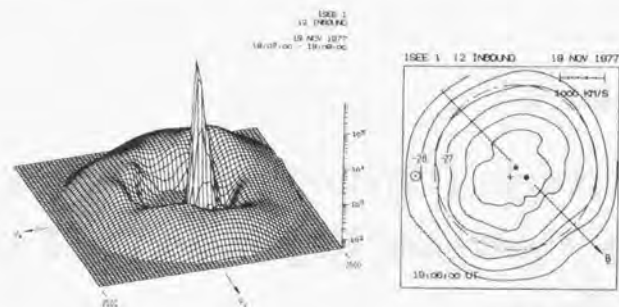


Figure 2-1. Example of upstream diffuse ion event from ISEE-1 satellite [Paschmann *et al.*, 1981]. Left Panel shows count rate in ecliptic plane. The tall sharp (solar ions) and broad (diffuse ions) distributions are shown. Right Panel shows iso-contour phase space density for the same event as Left Panel. Cross marking and dot represent satellite frame and solar wind frame center, respectively. IMF projected on the ecliptic plane is shown as an array through the solar wind dot. Asterisk is the center of the broken circle which guides the isotopic distribution.

surface along the magnetic field line with an e -holding distance of $7 \pm 2 Re$ (Re is earth radii) at 30 keV [Ipavich *et al.*, 1981a] (see Fig. (2-2a)). Their statistical analysis was made under the radial IMF direction (X direction in GSE) with 33 events. The e -holding distance increases with increasing diffuse ions' energies [Tratner *et al.*, 1994] (see Fig. (2-2b) and (2-2c)). The latter analysis included various IMF direction with increasing number of the events (~ 380). They also calculated the distance along the IMF for events with the shock angle $\theta_{sw} < 25^\circ$ and obtained an exponential decrease of the proton flux at 20 keV with a scaling distance of $4.8 \pm 0.1 Re$ (Fig. (2-2b)). At the same time, there exist low-frequency hydromagnetic waves $\sim 0.01 - 0.1 Hz$ with large amplitudes $\delta B / B_0 \sim 1$. Fig. (2-3) shows an example of the upstream waves [Fairfield, 1969]. The spatial variability of the intensity of the upstream waves has also been studied. The amplitude of the waves decreases along the IMF with an e -holding distance of 15 Re [Fairfield, 1969].

The co-existence of the diffuse ions and the waves indicates the importance of wave-particle interaction processes, including the ion acceleration from the solar wind energy to the observed

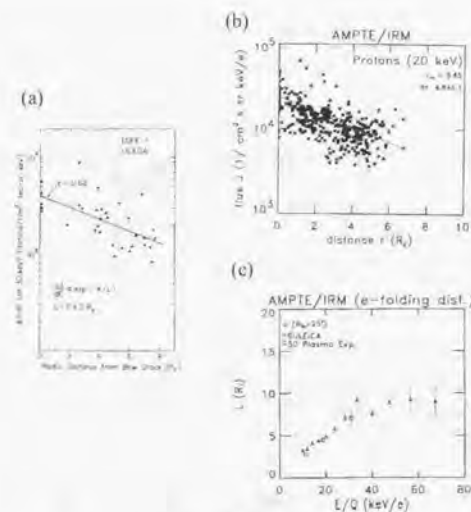


Figure 2-2. Spatial variance of the intensity of the diffuse ions along the interplanetary magnetic field (IMF). Panel (a) shows the results from ISEE-1 [Ipavich *et al.*, 1981a] when the IMF is nearly parallel to Sun-Earth line. Panel (b) shows the results from AMPTE/IRM [Tratner *et al.*, 1994] in the condition that the shock angle is smaller than 25° . In both case, the intensity decreases with increasing the distance from the shock along the IMF. Panel (c) shows the energy dependence of the e -holding distance of the intensity decreasing. The longer distance is observed in higher energy [Tratner *et al.*, 1994].

high-energy range (~ 100 keV). The most detailed theoretical acceleration model for diffuse ions is the diffusive acceleration (DA) process (see Appendix A). In this model it is assumed that the ions are scattered elastically in the upstream wave frame. The elastic scattering process is due to small-angle pitch-angle scattering by the resonant interaction with the upstream waves. The ions which are scattered back toward the shock can gain considerable energy in the shock frame. It is also assumed in this model that during the scattering process the ion pitch angle distribution becomes isotropic in the wave frame. Particles in returning hemisphere to the shock in the velocity space can re-encounter the shock. The encountering ions are possibly reflected

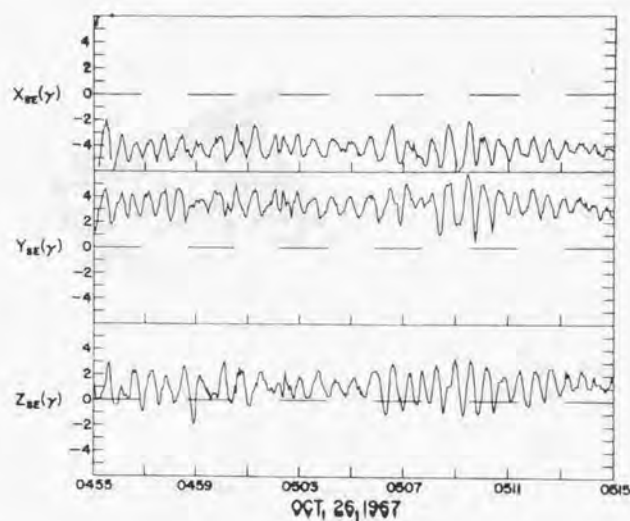


Figure 2-3. Example of upstream magnetic wave from Explorer 34 [Fairfield, 1969]. Low-frequency large-amplitude waves are seen.

back from the shock surface or downstream region. These ions are again backstreaming to the upstream region, re-scattered and gain a momentum. Repeating this cycle of process, ions are multiply accelerated. Furthermore, the observed energy spectrum shows exponential form with the same e -holding energies for protons, alpha particles, and CNOs if represented in the energy-per-charge unit (see Fig. (2-4) [Ipavich *et al.*, 1981b]). The relations between wave power and energy density of the diffuse ions are consistent with the DA model based on the quasi-linear wave-particle interaction theory [Lee, 1982; Trattner *et al.*, 1994]. Diffusive acceleration model, however, has the most important problem about pitch angle scattering process with upstream/downstream waves because the observed waves appear to be nearly monochromatic.

The another possible source of the high energy diffuse ions is leakage model. Some authors assert that all upstream diffuse ions are leaking from the magnetosheath / magnetospheric ions

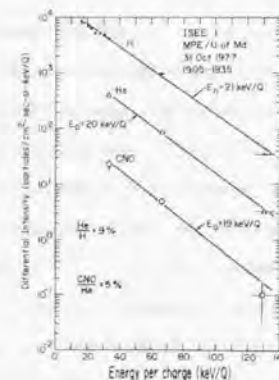


Figure 2-4. Energy spectrum of differential number flux for the diffuse ion. They are an exponential form and the e -holding energy shows nearly same value for proton, alpha, and heavy ion (CNOs) in energy per charge unit.

[e.g. Anagnostopoulos *et al.*, 1986, 1998]. These authors have shown the correlation of the diffuse ion events with geomagnetic activity. It has been confirmed [e.g. Möbius *et al.*, 1986] that magnetospheric ions such as O⁺ exist in diffuse ions population. However, it is not likely that all diffuse ions have magnetospheric origin. Even when the magnetic field passing the satellite unlikely connects the magnetosphere, diffuse ion events are observed [Gosling *et al.*, 1989; Sugiyama *et al.*, 1995]. Further, an observed correlation between the ratios of He²⁺/H⁺ for the solar wind and for the diffuse ions [Ipavich *et al.*, 1984] raises difficulty if all diffuse ions are of magnetospheric origin.

In this Chapter, first we have made statistical study about the upstream diffuse ion events. We have advantage of the sensitive detector for ion observations from LEP detector on GEOTAIL satellite and the satellite trajectory which covers the wide upstream region. We discuss the spatial profiles of the upstream diffuse ions with respect to (1) flux intensity, (2) energy spectrum index and (3) pitch angle distribution types. The flux intensity and energy spectrum of diffuse ions are consistent with the previous observations obtained in near shock region. However, our observations show that the pitch angle distribution consists of two types, which

are nearly isotropic and half-isotropic angular distributions. The half-isotropic distribution lacks of returning ions to the shock. This distribution shape is problematic because the lack of returning ions should stop the DA process. In contrast to the lacking hemisphere, ions in the escaping side are well scattered, which suggests that the wave-particle interaction takes place efficiently but without extending to the returning hemisphere. As mentioned in Appendix A, the scattering process which is derived from the cyclotron resonance condition has the limitation problem at 90° . The scattering efficiency around 90° decreases to zero. At first sight, it is considered that the observed half-isotropic distribution is the result of such interactions. If so, how the isotropic distribution is produced? So, it is remained as an unsolved question how the observed distributions are constructed by the wave-particle interaction process in the large amplitude upstream waves. Next, we discuss the wave-particle interaction process in Section 2.3.

2.2 Upstream Diffuse Ion Events from GEOTAIL Observations

2.2.1 The GEOTAIL Mission and Instrumentations

The data for this study were obtained from the GEOTAIL satellite. One of the major subjects of this satellite is to investigate the magnetotail dynamics in the ISTP campaign. The instruments are designed to observe the magnetotail plasma signature where the plasma density is more tenuous and weaker magnetic field intensity in the distant plasma sheet than those in the solar wind. With these sensitive detectors we have obtained additional/new features about the upstream suprathermal ions. We have used the GEOTAIL near-earth orbit interval from February, 1995 to April, 1997. The apogee is about 30 Re in the elliptic plane, so that the GEOTAIL surveys more extensive region than previous satellites (e.g. ISEE-1,2 $\sim 17 Re$, AMPTE/IRM $\sim 19 Re$). We have a better coverage to investigate the spatial distribution of the character of the diffuse ions.

Low Energy particle instrument (LEP)

The plasma data were obtained from the three-dimensional (3D) electrostatic low energy particle (LEP) instrument. The LEP selects incoming ions according to their energy per charge. The LEP has two alternative energy modes to measure positive ions (the low energy mode covers from 32 eV/q to 40 keV/q, and high energy mode from 5 keV/q to 42 keV/q). Only data in the high energy mode have been used in this statistical study. Seven detectors are placed at the positions corresponding to the incident elevation angles of 0° , $\pm 22.5^\circ$, $\pm 45.0^\circ$, and $\pm 67.5^\circ$ from the satellite spin plane. As the spin axis is set almost parallel (within 3°) to the GSE Z axis (north-south line), the observation in azimuthal direction is provided by the spin. One spin period (~ 3 sec.) is divided into 16 sectors. In each sector, the energy scan is made by stepping the analyzer voltage in 32 logarithmic steps. One set of the LEP data consists of 32 (Energy) \times 16 (Azimuth) \times 7 (Elevation) points obtained in one spin period. The 3D data set are summed for four-spin period (~ 12 sec.) on the satellite. For a detailed description of the instrument see *Mukai et al.*, [1994].

Magnetometer (MGF)

The magnetic field measurements were obtained from the triaxial fluxgate magnetometer. The three components of the magnetic field are sampled 128 times per seconds, and averaged to 16 vectors per second on the satellite. Data for all periods used in this statistical study were 4 spin averaged as the LEP data were. For a detailed description of the instrument see *Kokubun et al.*, [1994].

2.2.2 Event Selection

A typical example from the diffuse upstream ion events selected for this study is shown in Fig. (2-5). Plotted is the differential number flux [$1/\text{cm}^2 \text{ sec str keV/q}$] for ions between 9 and 11 keV per charge, from 1:15 to 2:15 UT on 10 August, 1996, (X $\sim 10 Re$, Y $\sim -22 Re$, Z $\sim -3.0 Re$). In this thesis we use the GSE (geocentric solar ecliptic) coordinate system. We presume that all the ions are protons. Since the flux ratio of heavy ions to protons is typically less than several percent [*Ipavich et al.*, 1984], our presumption should not cause any serious

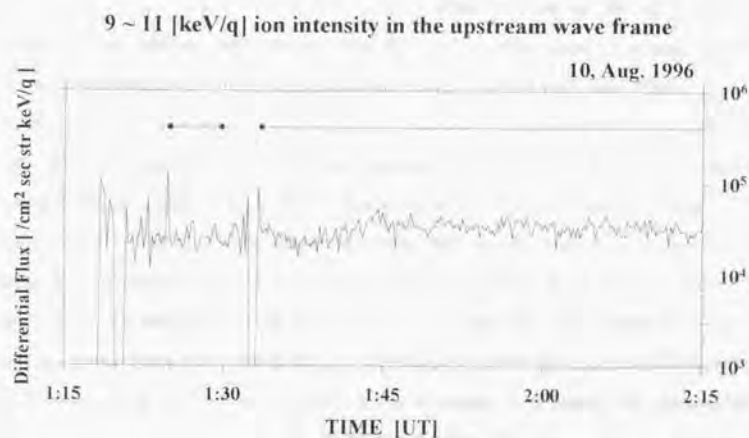


Figure 2-5. Example of the intensity profiles in time for upstream diffuse ion events observed from GEOTAIL-LEP instrument. Plotted is for the differential number flux between 9-11 keV/q in upstream wave frame (see text for transportation procedures). The upper bars show the selected data interval for our statistic study.

mis-interpretation. The flux level remained high after 1:18 except a few dropouts (at 1:20 and 1:33). The sudden onset of the particle flux and flat-topped flux profile are characteristic in the upstream diffuse ion events for the energy range less than several tens keV. For our statistical study, we have chosen such diffuse ion events by the following selection procedures: First, we have transformed the LEP measurements from the satellite frame to the upstream wave frame. We treat the upstream wave as the Alfvén wave propagating upstream direction along the IMF in solar wind frame. From the solar wind parameters (field direction, intensity, and density) we have set the center of the upstream wave frame. Next, the ion flux whose pitch angle is between 70° (100°) and 80° (110°) for positive (negative) X component of the interplanetary magnetic field (IMF) is averaged per 10 samples (~ 2 min.) in the upstream wave frame. This restriction is to distinguish the diffuse ion distribution from "reflected beam ion" distribution. For selecting the stable events, a ratio of maximum to minimum differential flux in the 10

samples should be less than a factor of 3. This averaging makes one datum. This averaging procedure is to avoid ambiguity due to the low count rate. The intensity of the flux in Fig. (2-5) is shown in the upstream wave frame. Horizontal bars in Fig. (2-5) show the selected data interval. We try above selection for LEP data from 5 to 31 keV every 2 keV.

GEOTAIL Positions (GSE X-Y plane)

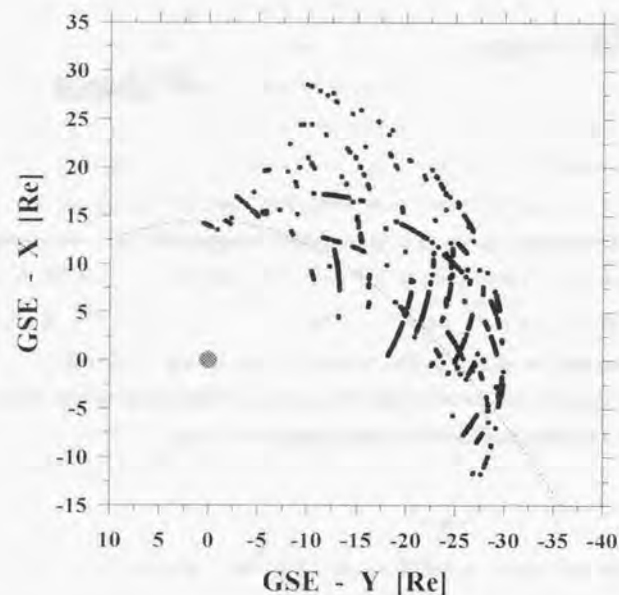


Figure 2-6. GEOTAIL positions during selected events for 15-17 keV/q ions in the eclipse plane in GSE coordinate system. The Sun is located to top and right is dawnside. The dotted curve shows nominal shock location [Fairfield, 1971].

2.2.3 Flux Intensity and Energy Spectra

Previous observations have shown that the differential particle flux depends on the distance from the shock [Ipavich *et al.*, 1981a; Trattner *et al.*, 1994]. We have also studied the spatial profile about the flux intensity in the wider region than previous studies, so that we have gotten the spatial dependence on the distance both along the IMF direction and along the X axis in GSE coordinate. We have adopted following criteria in addition to above data selections in Section 2.2.2. The 2-minutes time-averaged IMF direction ($\bar{\theta}$ for elevation angle, $\bar{\phi}$ for longitudinal angle) have $-20^\circ < \bar{\theta} < 20^\circ$ and $(135 - 20)^\circ < \bar{\phi} < (135 + 20)^\circ$ or $(315 - 20)^\circ < \bar{\phi} < (315 + 20)^\circ$. For example, we have selected 1513 data set for 15 - 17 keV ions (hereafter 16 keV ions). Fig. (2-6) shows the GEOTAIL satellite positions during the occurrence of the events for 16 keV ions. The dotted curve shows nominal bow shock position [Fairfield, 1971]. The observed positions are widely distributed over the bow shock.

Hereafter, for convenience to show the upstream distance, we set a two-dimensional coordinate system in the ecliptic plane: X_s and D_s axis. X_s is the X coordinate of the shock foot point of the IMF line. D_s is the distance from the bow shock along the IMF direction. The geometry is illustrated in Fig. (2-7). We use the bow shock model of Peredo *et al.* [1995], which includes the effects of the solar wind ram pressure, Alfvén Mach number and the IMF cone angle (the angle between the IMF line and X direction in GSE).



Figure 2-7. The geometry of the definition of X_s and D_s .

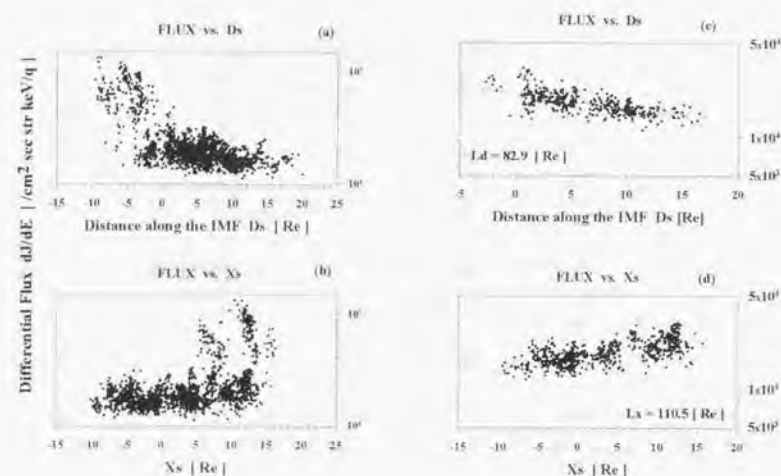


Figure 2-8. The differential number flux versus D_s (Panel (a)) and X_s (Panel (b)) for 16 keV events. The differential number flux versus D_s (Panel (c)) for $0 \text{ Re} < X_s < 5 \text{ Re}$ events with least square fitting results (dotted line) of the functional form of Eq. (2.1). The v -holding length is 82.9 Re with correlation coefficient 0.65. The differential number flux versus X_s (Panel (d)) for $3 \text{ Re} < D_s < 8 \text{ Re}$ events with least square fitting results (dotted line) of the functional form of Eq. (2.2). The v -holding length is 110.5 Re with correlation coefficient 0.66. The intensity decreases exponentially with both increasing of D_s and decreasing of X_s .

Fig. (2-8) shows the differential number flux at 16 keV as a function of D_s (Panel (a)) and X_s (Panel (b)). The intensity weakly decreases with increasing D_s and with decreasing X_s . The flux intensity seems to depend on both D_s and X_s . To show the real dependence on X_s and D_s , the data sets are subdivided into 5 Re by each X_s and D_s axis. The flux profile versus D_s for the data with $0 \text{ Re} < X_s < 5 \text{ Re}$ is plotted in Fig. (2-8c), and the flux profile versus X_s for the data with $3 \text{ Re} < D_s < 8 \text{ Re}$ is plotted in Fig. (2-8d). In these figures it is clearly shown that the intensity exponentially decreases as reported in previous works. The dotted lines show the result of the least square fitting of the functional form of

Energy [keV/q]	L_d [Re]	Number of events	Correlation Coefficient
6	25.6	208	0.78
8	34.8	399	0.84
10	42.0	444	0.85
12	50.0	446	0.81
14	64.6	430	0.74
16	82.9	378	0.65
18	107.8	296	0.54
20	171.0	207	0.35
22	183.7	101	0.31
24	300.2	61	0.23
26	107.8	30	0.63
28	903.2	14	0.11
30	91.5	5	0.79

Table 2-1. Scale length L_d , number of events and correlation coefficient for the fitting of L_d for 13 energy ranges.

$$A \exp(-Ds / L_d) \quad (2.1)$$

for Panel (c) and

$$A \exp(-Xs / Lx) \quad (2.2)$$

for Panel (d) with calculated scale length (L_d and Lx). The scale length is $L_d = 82.9 Re$ with correlation coefficient 0.65, and $Lx = 110.5 Re$ with 0.66, respectively. The summary of the scale length L_d and number of the data set are tabulated in Table (2-1). GEOTAIL results show relatively larger scale length than previous works ($7 Re$ for 30 keV ion [Ipavich *et al.*, 1981a] and $4.8 Re$ for 20 keV ion [Iratner *et al.*, 1994]). These differences are discussed later. A general trend is an increasing of L_d with increasing of energy.

The larger scale length L_d for the higher energy ions suggests that the energy spectra get harder with increase of Ds . The energy spectra of the diffuse ions in the selected pitch angle ($70^\circ \sim 80^\circ$ for positive B_x , $100^\circ \sim 110^\circ$ for negative B_x) are shown in Fig. (2-9). The solar wind distribution is excluded in these plots. These are obtained in different Ds from the data set in Fig. (2-8c). Panel (a) is at $Ds \sim 2.0 Re$, Panel (b) is at $Ds \sim 12.1 Re$. The data points form straight lines in both Panels, indicating that the energy spectrum has an exponential form. Assuming a functional form

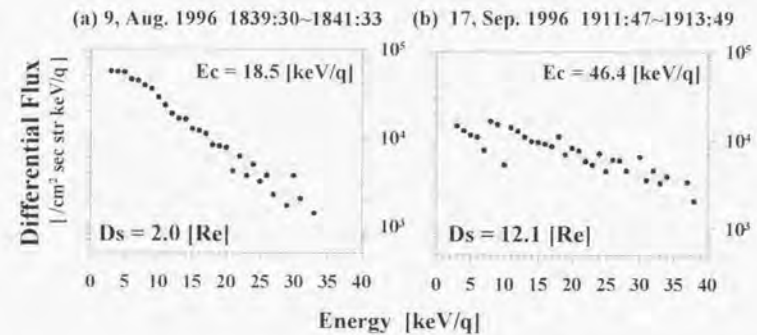


Figure 2-9. Energy spectrum for the diffuse ion events in the near upstream region (Panel (a) $Ds = 2.0 Re$) and in the far upstream region (Panel (b) $Ds = 12.1 Re$). The dotted lines are results of the least square fitting with exponential function (Eq. (2.3)) over 10 keV. E_c is the characteristic energy. The spectrum in the near upstream region ($E_c = 18.5$) is softer than that in the far upstream region ($E_c = 46.4$).

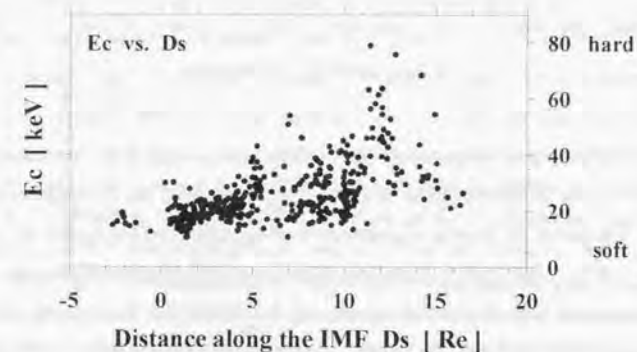


Figure 2-10. The characteristic energy (E_c) versus Ds for data $0 Re < Xs < 5 Re$. The energy spectrum becomes harder with increasing of Ds .

$$\frac{dJ}{dE} \propto \exp(-E/E_c) \quad (2.3)$$

we have calculated the characteristic energy E_c . The dotted lines in Fig. (2-9) are the results of the least-square fitting. We can see the harder spectrum in large Ds as expected from the energy dependence of Ld (The E_c value is 18.5 keV for Panel (a), 46.4 keV for Panel (b)). The characteristic energy E_c of diffuse ion events from the data set in Fig. (2-8c) are plotted in Fig. (2-10) against Ds . Although the data becomes more scattered in large Ds , the trend shows increasing of E_c with increasing Ds .

2.2.4 Pitch Angle Distribution

In this section we investigate the angular distribution of the upstream diffuse ion events. Paschmann *et al.*, [1981] presented a two-dimensional distribution of diffuse ions, (Fig. (2-1)) which is characterized by the nearly isotropic around the ambient magnetic field. However, our observations have shown that the distribution consists of two types, that are nearly isotropic and half-isotropic angular distributions. Fig. (2-11) shows examples of these two types of distributions in the satellite (\sim shock) frame in the plane including the parallel direction to the magnetic field and one of the perpendicular directions to the field (the same events as Fig. (2-9)). The vertical axis is the velocity parallel to magnetic field line (V_{\parallel}) and positive V_{\parallel} directs from shock to upstream side. A solid curve shows iso-contour level of the phase space density ($1 \times 10^{-16} [\text{s}^3 \text{m}^{-6}]$). A gray triangle represents the solar wind velocity. From the shape in Panel (b) we call this type of distribution as 'mushroom' type. Note that the incompleteness of the 'mushroom'. The part of the 'stem' is contaminated with the solar wind heavy ions (thin curve in Panel (b) around $V_{\parallel} \sim -800$ [km/s]). Therefore, diffuse ions can be identified only in the cap part. The cap part consists of the ions which are escaping from the shock. This smooth curve in the cap part suggests that the scattering process by the wave occur efficiently. To visualize the lacking in the returning hemisphere, we have fitted an ellipse function to the escaping half-hemisphere part,

$$a(V_{\parallel} - V_{\parallel c})^2 + b(V_{\perp} - V_{\perp c})^2 = 1 \quad (2.4)$$

where $(V_{\parallel c}, V_{\perp c})$ is the center velocity of the ellipse. As seen in Fig. (2-11b), the ellipse shown by a dashed curve clearly has a lacking part in the returning side. This suggests that the scattering efficiency against the returning ions is weaker than that against the escaping ions.

When the pitch angle distribution is plotted in a certain energy range, the width of the pitch angle distribution calculated from upstream-ward magnetic field direction determines the distribution shape. 180° (90°) pitch angle width constructs the isotropic (half-hemisphere)

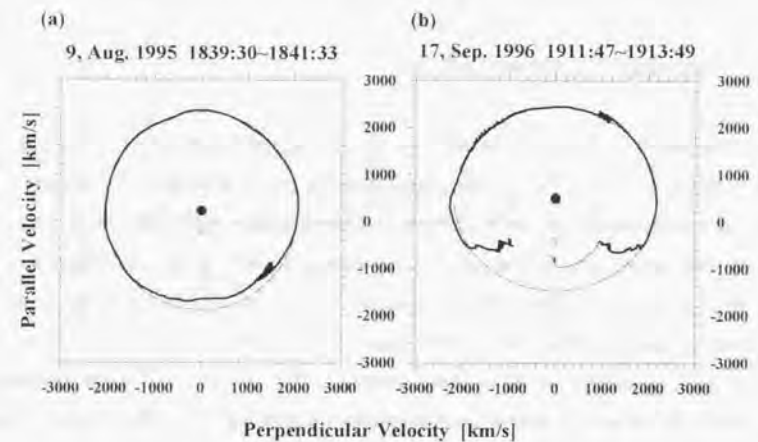


Figure 2-11. Example of angular distribution of diffuse ions for the same events as Fig. (2-9). The 3D observation data is sliced in the plane including the magnetic field and one of the V_{\perp} directions. The vertical axis is the velocity parallel to magnetic field line (V_{\parallel}) and positive V_{\parallel} directs from shock to upstream side. Thick curve shows iso-contour level at $1 \times 10^{-16} [\text{s}^3 \text{m}^{-6}]$ for diffuse ions. Note that the distribution in Panel (b) is contaminated by solar wind heavy ions (thin curves). Gray triangle represents the solar wind center. In the near upstream region (Panel (a)), nearly isotropic distribution is observed, on the other hand, in the far upstream region (Panel (b)) 'mushroom' type distribution is observed. Dashed curved shows the fitted ellipse for upper hemisphere (flowing to upstream side) of each distribution. Each black circle shows the center of the fitted ellipse. A hemisphere of returning part in the 'mushroom' distribution is clearly cut off.

distribution. In order to investigate the dependence of angular distributions on the Ds , Fig. (2-12) shows the maximum pitch angle width of the LEP instrument detection (> 1 count/sample). The data set are four different energy range (10, 16, 22, 28 keV) in $0 Re < Xs < 5 Re$. The pitch angle is calculated in the upstream wave frame. The pitch angle width becomes narrower in all energy levels with increasing of Ds , so that the distribution shape changes from nearly isotropic to mushroom type. In the near upstream region, the diffuse ions are observed in nearly isotropic, which is consistent with previous observations. In the far upstream region, the density of the returning hemisphere becomes smaller, which results in the 'mushroom' distribution.

2.2.5 Summary of Observations

We have analyzed the upstream diffuse ion events of the quasi-parallel shocks in the dawn side upstream region. In summary we have shown the following: 1. The differential flux intensity of the diffuse ions becomes weaker as the observation location goes away from the shock surface along the IMF (going positive Ds) and into pre-dawn upstream region (going negative Xs direction). 2. The energy spectra have exponential dependence and become harder as the observation location goes into a far upstream region. 3. The 'mushroom' type distributions are observed more frequently in a far upstream region. 4. The smooth curve in the escaping hemisphere of the 'mushroom' distribution suggests that the pitch angle changing process by the upstream wave occurs efficiently.

While the dependence of the scale length ld on the ion energy resembles with those in a previous work [Tratner *et al.*, 1994], scale length ld is longer in all energy range. The possible reasons may be the following. As seen in Section 2.2.4 distribution shapes of the diffuse ions are not always isotropic and they consist of nearly isotropic with weak expansion to perpendicular direction and 'mushroom' type. If it is assumed that the distribution of the diffuse ions is isotropic and the intensity is averaged all over the direction, the flux intensity is underestimated because of the existence of the lacking hemisphere. Since the 'mushroom' distribution with a lacking hemisphere is observed in the far upstream region, the flux intensity is further under-estimated in the far upstream region. This leads to the smaller scale length ld in previous results.

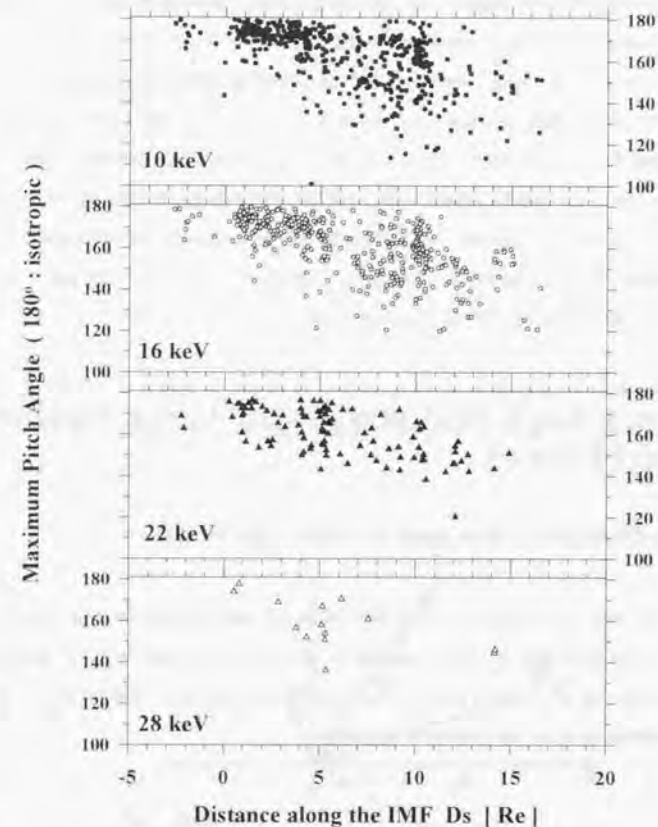


Figure 2-12. Pitch angle width for the diffuse ion distribution. The width is defined as the maximum pitch angle based on the upstream-ward field aligned direction. The 180° (90°) angle correspond to a nearly isotropic (half-hemisphere) distribution. The pitch angle is calculated in the upstream wave frame in the four energy range (10, 16, 22, 28 keV). In the further upstream region along the IMF, the width becomes narrower, which suggests that the 'mushroom' distribution is frequently observed in the further upstream region.

The energy spectrum also represents an exponential shape in the far upstream region, but the slope is harder. These results suggest that high energy ions are more easily extending to the upstream region or hard to be scattered back to the shock.

The wider observation regions than the ISEE and AMPTE/IRM satellites enable us to find the non-isotropic distribution 'mushroom' type. Since the 'mushroom' type distribution is observed in the far upstream (Fig. (2-12)), the previous observations were hard to detect them. From the smooth curve in the escaping half-hemisphere, it is suggested that the wave-particle interaction process works efficiently. In next section, we investigate the ion motions in the large amplitude Alfvén waves by means of a test particle simulation, and explain the dependence of the distribution shapes on the distance from the shock.

2.3 Pitch Angle Scattering in the Large Amplitude Alfvén Waves

2.3.1 Difficulties in Resonance Scattering Process

In the previous observations near the shock, the diffuse ions have a nearly isotropic distribution. It has been considered that ions are scattered by the upstream waves with the small-angle pitch-angle scattering process (the quasi-linear scenario) in which the parallel velocity V_{\parallel} should satisfy the anomalous cyclotron resonance condition,

$$\omega_w = \Omega_i + k_{\parallel} V_{\parallel} \quad (2.5)$$

The waves are excited by the ion-beam instability between the solar wind cold ions and reflected beam ions which is produced at the quasi-perpendicular shock region. The excited waves are right-hand polarized with a nearly monochromatic peak at the low frequency ($<$ proton gyro-frequency), propagating upstream direction (the same direction as the reflected beam ions) along the ambient magnetic field in the plasma rest frame. Exactly speaking, the resonance is anomalous type. The observed wave amplitude is very large (the ratio of the wave amplitude to ambient magnetic field intensity is over 0.5). Since the solar wind speed is super-Alfvénic, the waves are convected toward the shock and observed in satellite frame with a left-

hand polarization (anomalous Doppler-shift effect). The wave number of the largest growth rate is mainly determined by the density and velocity of the reflected beam ions. From the observational results and the linear calculation for the instability, the wave length for the typical upstream parameters is about 50 in the ion inertia length unit.

When the above quasi-linear scenario applies for the ions' pitch angle scattering process, waves should consist of multi-components and the wave phase also should distribute randomly. Observed upstream waves, on the contrary, often show a nearly monochromatic feature which is at variance with this request. And also the observed diffuse ion distribution is not always isotropic. In this section 2.3, we propose an alternative scenario for the pitch angle changing process. In a large amplitude monochromatic wave, ions are phase trapped and subjected to a large pitch angle changing, even though the cyclotron resonance condition is not satisfied. We present an overview for the equations to describe the trapping process in Section 2.3.2, show example of test particle motion in Section 2.3.3, and then give the consequent pitch angle distribution in Section 2.3.4.

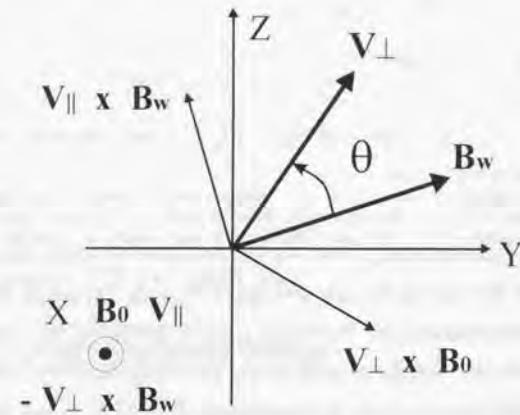


Figure 2-13. The geometry of the forces acting on the ion in the wave frame. Ambient magnetic field vector B_0 and the wave vector k are aligned to X axis. B_w is wave component. Three Lorentz forces are acting on an ion running parallel to B_0 . θ is an important parameter to determine an ion motion defined as the phase of V_{\perp} relative to B_w in the plain perpendicular to B_0 .

2.3.2 Basic Equation

Here we consider an ion motion in the large amplitude monochromatic Alfvén wave. From the linear calculation of the ion beam instability, the excited waves are right-hand circularly polarized and propagating along the ambient magnetic field \mathbf{B}_0 . So, we set in 1-dimensional space and the spatial axis is set in \mathbf{X} ($\mathbf{B}_0 // \mathbf{k} // \mathbf{X}$). Let \mathbf{B}_w be the magnetic field vector of the Alfvén wave. The equation of motion of an ion in the wave frame is simply given by [e.g. *Sudan and Ott, 1971; Matsumoto et al., 1974* for electrons in whistler waves, and *Hoshino and Terasawa, 1985* for ions in MHD waves]

$$\frac{d\mathbf{v}}{dt} = \frac{e}{m} \mathbf{v} \times (\mathbf{B}_0 + \mathbf{B}_w) \quad (2.6)$$

where m , e and \mathbf{v} are the ion mass, charge and velocity. In terms of the velocity components, we have

$$\frac{dv_{\perp}}{dt} = -\Omega v_{\parallel} \sin \theta \quad (2.7)$$

$$\frac{dv_{\parallel}}{dt} = \Omega v_{\perp} \sin \theta \quad (2.8)$$

$$\frac{d\theta}{dt} = -\Omega_0 - k v_{\perp} + \Omega \frac{v_{\parallel}}{v_{\perp}} \cos \theta \quad (2.9)$$

where $v_{\perp} = \sqrt{v_x^2 + v_y^2}$, $\Omega_0 = eB_0 / m$, $\Omega = eB_w / m$ and θ is the phase angle between \mathbf{v}_{\perp} and \mathbf{B}_w as shown in Fig. (2-13).

The Lorentz force acting on the ion may be decomposed into three elements, $\mathbf{v}_{\perp} \times \mathbf{B}_0$, $\mathbf{v}_{\parallel} \times \mathbf{B}_w$ and $\mathbf{v}_{\perp} \times \mathbf{B}_w$, as illustrated in Fig. (2-13). The first one causes the usual cyclotron motion and is represented in the first term on the right hand side of Eq. (2.9). The second force accelerates the ion in the parallel direction to \mathbf{B}_0 . The motion is treated through Eq. (2.7), and changes the phase θ by Doppler-shift represented in the second term on the right hand side of Eq. (2.9). The third force accelerates the ion in the perpendicular direction to \mathbf{B}_0 and also changes the phase angle θ , which is represented in the third term on the right hand side of Eq. (2.9). As seen in Eqs. (2.7) ~ (2.9), ion motion strongly depends on phase angle θ and amplitude of waves B_w through Ω .

Fig. (2-14) shows how an ion moves in the velocity space (v_{\perp} , v_{\parallel}). An ion changes its velocity

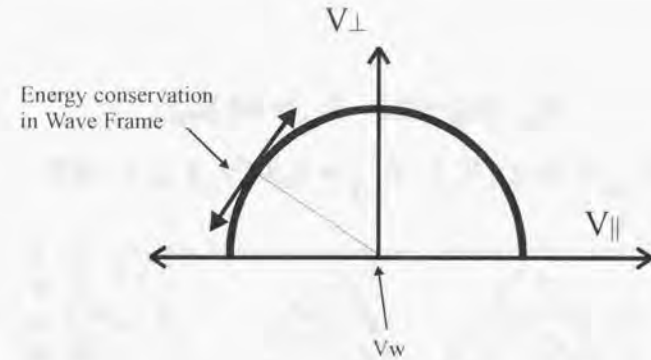


Figure 2-14. The geometry of an ion trajectory in velocity space. Since an ion energy is conserved in wave frame, the motion is restricted on the circle whose center is the wave phase velocity V_w .

components in time but the motion is restricted on a circle whose center is wave phase velocity V_w because ion energy is conserved in the wave frame,

$$\frac{d}{dt} [v_{\perp}^2 + v_{\parallel}^2] = 0 \quad (2.10)$$

Under a constant and uniform ambient magnetic field B_0 with large amplitude wave, the phase θ of ion is bunched in a certain angle [e.g. *Sudan and Ott, 1971; Matsumoto et al., 1974; Hoshino and Terasawa, 1985*] (see Appendix B).

2.3.3 Pitch Angle Scattering Motion

To derive how much the ions can change their pitch angle in the large amplitude monochromatic MHD wave field, numerical computations of the basic Eqs. (2.7) ~ (2.9) are performed for various initial parameters in 1-dimensional space. The velocity, time and length are normalized to Alfvén velocity V_A , inverse proton gyro-frequency Ω_p^{-1} , and ion inertia length λ_i in the normalized density and magnetic field intensity space. To simplify the particle

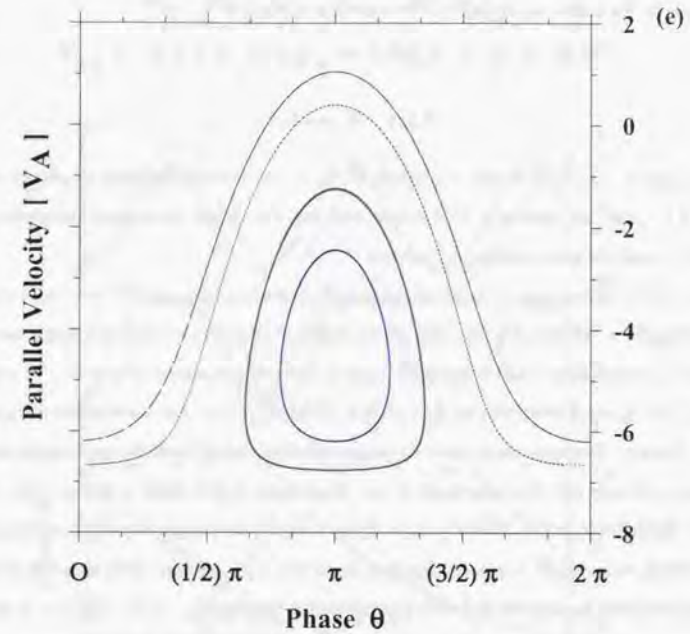
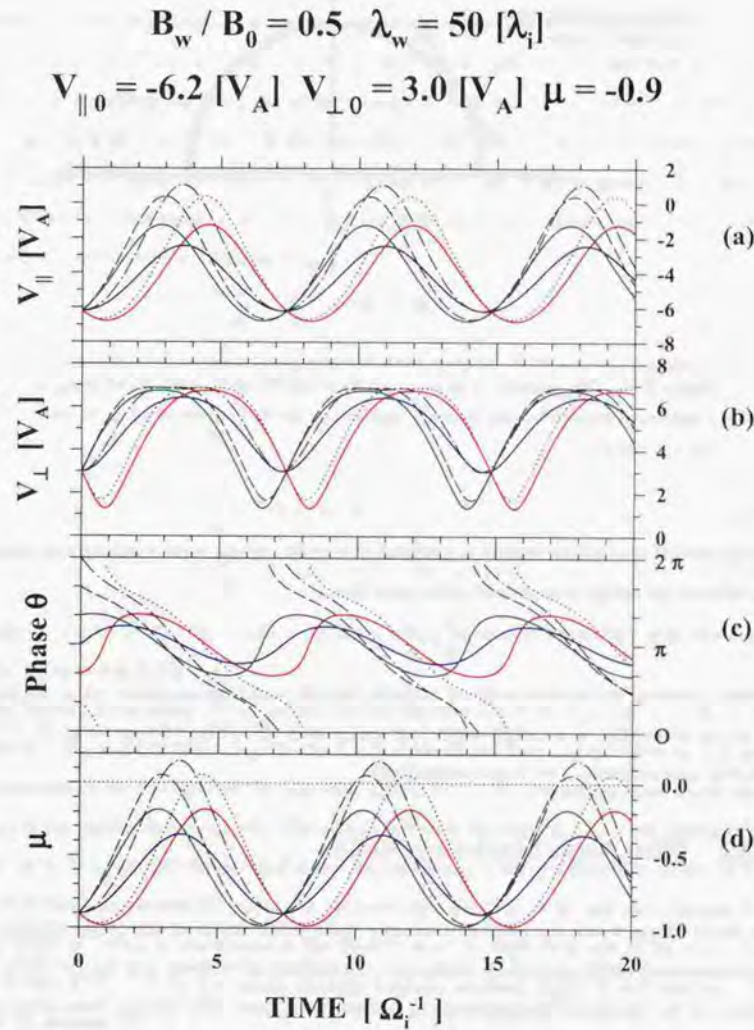


Figure 2-15. Time profile of parallel v_{\parallel} (Panel (a)), perpendicular v_{\perp} (Panel (b)) velocity phase angle θ (Panel (c)) and pitch angle cosine μ (Panel (d)). Their initial pitch angle is -0.9 which consists of $v_{\parallel 0} = -6.2 V_A$ and $v_{\perp 0} = 3.0 V_A$. Six curves correspond to $\theta_0 = (1/3)\pi, (2/3)\pi, \dots, 2\pi$, which can be distinguished from others by line style shown in Panel (c). The wave amplitude and wave length are $B_w / B_0 = 0.5$ and $50 \lambda_i$. In this case, the resonance velocity V_R is about $-8 V_A$. Although ions do not cross V_R , their pitch angle vary in wide range (from -1 to 0.15). Panel (e) shows the trajectory in the parallel velocity and phase θ plane. The ions whose initial phase angle has $\theta_0 = (2/3)\pi$ and $\theta_0 = (4/3)\pi$ move the same trajectory in this plane (e). And also the pair of $\theta_0 = (1/3)\pi$ and $\theta_0 = (5/3)\pi$ moves the same trajectory.

motion, the orbits are calculated in the wave frame where the motional electric field is vanished. The ambient magnetic field directs to positive X. The steady right-hand polarized MHD waves are given by the following equations with the wave number k ,

$$B_y(x) = B_w \cos(kx) \quad (2.11)$$

$$B_z(x) = B_w \sin(kx) \quad (2.12)$$

In this Chapter, the wave length is constant at $50 \lambda_{i\perp}$, so that the cyclotron resonance velocity $V_R \sim -8 V_A$. Ions are injected at $X=0$ at time zero with their initial parameters: the phase θ_0 , the parallel $v_{\parallel 0}$ and the perpendicular $v_{\perp 0}$ velocity.

Fig. (2-15) shows one of the trajectories of ions about the parallel v_{\parallel} (Panel (a)), the perpendicular v_{\perp} (Panel (b)) velocity, phase angle θ (Panel (c)) and pitch angle cosine μ (Panel (d)) versus time. Their initial pitch angle is -0.9 which consists of $v_{\parallel 0} = -6.2 V_A$ and $v_{\perp 0} = 3.0 V_A$. Six curves corresponds to $\theta_0 = (1/3)\pi, (2/3)\pi, \dots, 2\pi$. The wave amplitude is $B_w / B_0 = 0.5$. The ion velocity varies in the wide range with time, which leads the pitch angle changing as shown in Panel (d). The time-scale is very short about a gyro-motion period (2π). This is one of the different points from the quasi-linear scenario where the scattering motion occurs quite slowly as averaged in gyro-period (see Appendix A 2). Another different point is that the parallel velocities have never had cyclotron resonance velocity $V_R \sim -8 V_A$. The ion motions are not concerned with the resonance process but related with the phase trapping motion as noted in Appendix B. Some ions are trapped about their phase angle θ around π (Panel (c)). Under these initial parameters, the ions whose initial phase θ_0 is $(2/3)\pi, \pi, (4/3)\pi$ are the case (colored curves). Panel (e) shows the same motions in the parallel velocity and phase θ plane. The variance width of parallel velocity for trapped ions is smaller than that of the other full-rotating ions, which leads small variance in their pitch angle. So, the pitch-angle changing strongly depends on their initial phase θ_0 . Fig. (2-16) shows another example in the same format in Fig. (2-15 (a)-(d)) in which the initial parallel velocity is larger than that of the previous case. Although the parallel velocities pass the V_R , the motions are the same as previous case. Thus in the large amplitude wave, the importance of the resonance velocity is weak. (In the region $v_{\parallel} \gg v_{\perp}$, the V_R has some meaning as shown in Appendix B, but now v_{\parallel} and v_{\perp} are comparable.) Although the resonance condition is not satisfied, the pitch angle

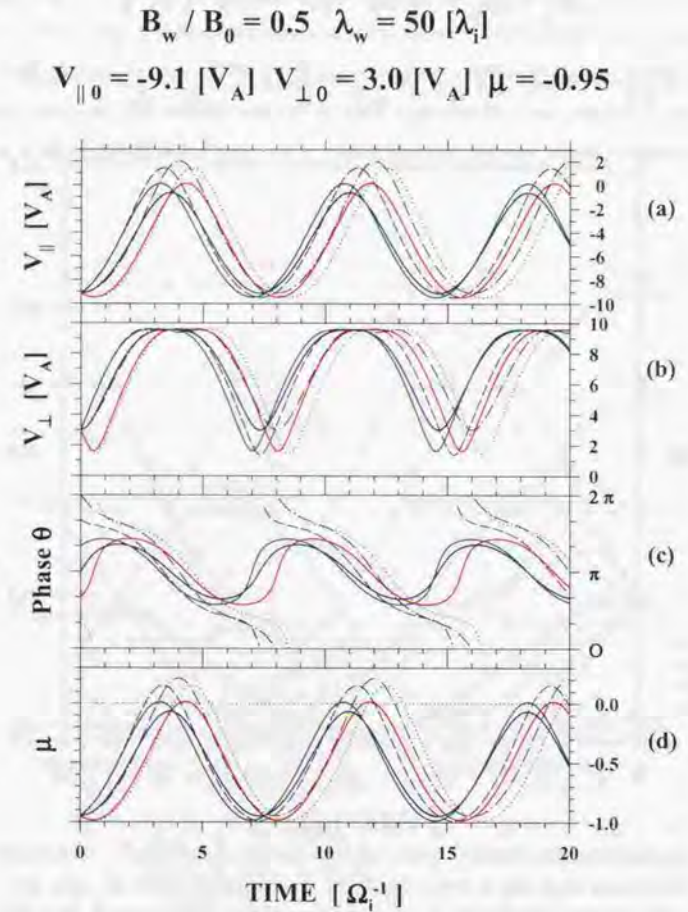


Figure 2-16. The same format as Fig.(2-15) (Panel (a)-(d)) for the ions whose initial pitch angle is -0.95 which consists of $v_{\parallel 0} = -9.1 V_A$ and $v_{\perp 0} = 3.0 V_A$. Even though ions cross the resonance velocity, the trajectories are the same as previous ones (Fig.(2-15)).

$$B_w / B_0 = 0.05 \quad \lambda_w = 50 [\lambda_i]$$

$$V_{\parallel 0} = -6.2 [V_A] \quad V_{\perp 0} = 3.0 [V_A] \quad \mu = -0.9$$

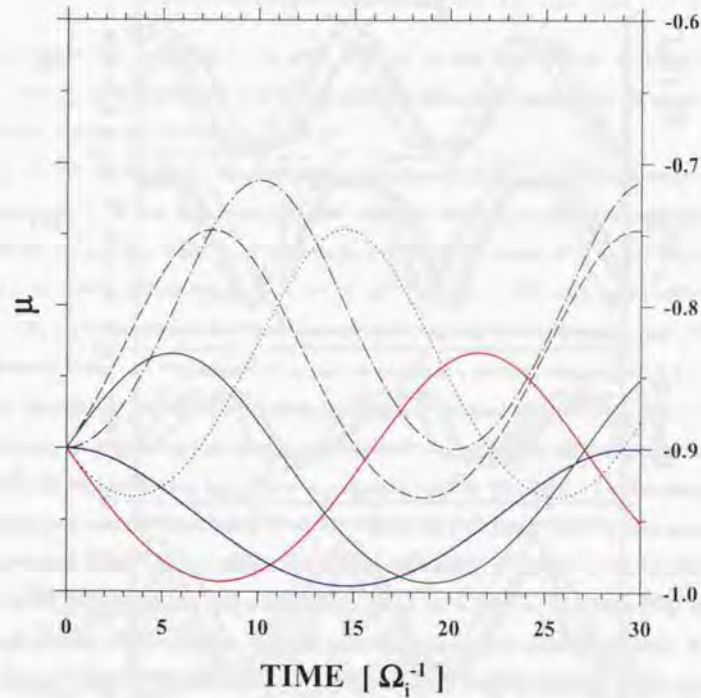


Figure 2-17. The same format as Fig. (2-15) (panel (d)) for the ions whose initial pitch angle is the same as Fig. (2-15) but wave amplitude is one order smaller ($B_w / B_0 = 0.05$). The variance width in μ depends on the wave amplitude.

widely distributes from -1 to 0.15. Fig. (2-17) shows the case where the wave amplitude is weak $B_w / B_0 = 0.05$. The pitch angle changing width becomes small and the pitch angle distributes from -1 to -0.7. Since the forces working on the ion are proportional to the wave amplitude as shown in Eqs. (2.7) ~ (2.9), the velocity variance becomes smaller as the amplitude decreases. The variance width of the pitch angle also decreases with the amplitude.

In the small amplitude wave case, it is expected that only the ions whose parallel velocity

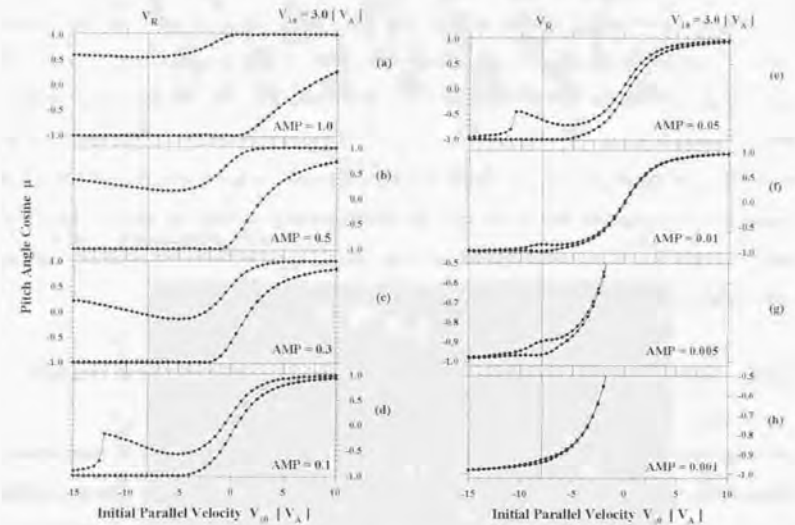


Figure 2-18. The pitch angle variance width for various amplitude condition (Panel (a) ~ (h)) versus the initial parallel velocity. The dotted curves in each panel show initial pitch angle. Maximum and minimum pitch angle (μ) are plotted with square and circle dots, respectively. The vertical solid line at the $v_{\parallel 0} \sim -8 V_A$ represents the cyclotron resonance velocity. In the large amplitude case, all the ions have changed their pitch angle. As amplitude becomes smaller, the interaction region is restricted around the resonance velocity which shows usual cyclotron resonance phenomena.

satisfies the resonance condition changes their pitch angle. Fig. (2-18) shows the variance width of the ions' pitch angle cosine (μ) versus their initial parallel velocity $v_{\parallel 0}$ for various amplitude conditions (Panel (a) ~ (h)). Since the initial perpendicular velocity is constant at $v_{\perp 0} = 3.0 V_A$, the initial pitch angle is not constant as represented by dotted curves in each panel. The vertical solid line in each panel at the $v_{\parallel 0} = -8 V_A$ represents the cyclotron resonance velocity V_R . Lower (upper) curve in each panel with circles (squares) shows the maximum (minimum) pitch angle cosine μ . Ions are oscillating in pitch angle between these two boundaries. In the small amplitude case, the pitch angle shows small change only around the V_R and the width between maximum and minimum angle is also small. As the amplitude increase, the width becomes wider and the influenced velocity range also becomes wider. When the amplitude is over 10 percent of the ambient field intensity, all the ions have been interacted by the wave and changed their pitch angle. The step like boundary feature at $v_{\parallel 0} = -12 V_A$ for Panel (d) and $-11 V_A$ for Panel (e) are reflection of the phase trapping effects. If the parallel speed is faster than this boundary, the trapping feature disappear and all the ions are phase rotating, so that the parallel velocity is nearly constant. When the wave amplitude is large, the boundary velocity gets faster because, as explained above, the force working on the ions becomes larger.

2.3.4 Ion Distribution Shape in Monochromatic Alfvén Waves

Following the ion trajectories, the pitch angle distribution is calculated in the monochromatic Alfvén waves. Fig. (2-19a) shows the pitch angle distribution versus time. The density in pitch angle space is color-coordinated in arbitrary unit. The initial velocities of these ions are set $|v| = 6 V_A$ with pitch angle between -1 and -0.8 every 0.02 , and $\theta_0 = (1/3)\pi, (2/3)\pi, \dots, 2\pi$. The wave parameters are the same as previous one, that is, wave length is $50 \lambda_i$, and wave amplitude is 0.5 . The pitch angle can extend over 90° ($\mu = 0$) and distribute in the wide range from $\mu = -1 \sim 0.2$. However, the distribution is not isotropic but bunched in time. The nearly isotropic distribution in the range $-1 < \mu < 0.2$ is observed if these ions are continuously injected over the time scale of this phase bunching interval ($> 6 \sim 7 \Omega_i^{-1}$), which is about 10 [sec.] in the actual upstream condition. As a result, the 'mushroom' distribution can be expected even in the monochromatic Alfvén waves.

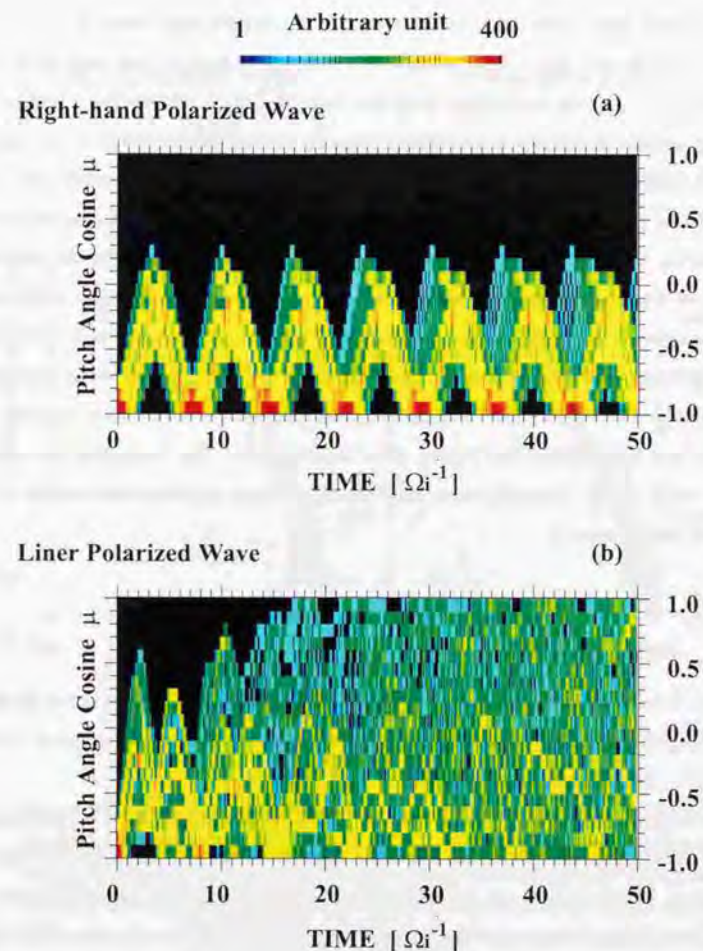


Figure 2-19. Pitch angle distribution versus time. The density in pitch angle space is color-coordinated in arbitrary unit. The initial velocities of these ions are set $|v| = 6 V_A$ with pitch angle between -1 and -0.8 every 0.02 , and $\theta_0 = (1/3)\pi, (2/3)\pi, \dots, 2\pi$. (a) The wave is right-hand circularly polarized form whose wavelength is $50 \lambda_i$ and amplitude is 0.5 . The distribution is not isotropic but bunched in time in the range $-1 < \mu < 0.2$. (b) The wave is linear polarized form whose wavelength is $50 \lambda_i$ and amplitude is 0.5 . The distribution has extended $\mu = 1$ in a short time interval ($\sim 18 \Omega_i^{-1}$ ~ three gyro-motion periods) and almost isotropic.

On the other hand, nearly isotropic distribution in the all pitch angle range $-1 < \mu < 1$ is observed near the bow shock. Since the width of the scattering range in pitch angle space does not reach $\mu = +1$ even in the large amplitude case $B_w / B_0 = 1.0$ (see Fig. (2-18a)), the complete isotropic distribution is not produced. But the minimum range reaches $\mu = -1$ even in the small amplitude case, which suggests that contribution of a opposite polarized wave may extend to the pitch angle distribution up to $\mu = +1$. The wave is left-hand polarized wave. Co-existence both the right and left-hand polarized waves may produce the isotropic distribution. The co-existence wave is liner polarized wave if the each wave length is the same. The observation in the upstream region of Giacobini-Zinner comet [Tsurutani *et al.*, 1987] and earth's upstream region [Elaoufir *et al.*, 1990] have detected liner polarized waves. Numerical simulations have also shown that the steepening of the circularly polarized wave results in the liner polarized wave [Omidi and Winske, 1990, Scholer, 1993]. The linear polarized wave is realistic feature in the upstream region. Here we set the linear polarized wave instead of the circularly polarize wave as

$$B_x(x) = B_w \cos(kx) \quad (2.13)$$

$$B_z(x) = 0 \quad (2.14)$$

where B_w is wave amplitude which is generally different from B_w . Fig. (2-19b) shows the pitch angle distribution in the same format as Fig. (2-19a) for $B_w = 0.5$. The μ reaches at +1 in a short time ($\sim 18 \Omega_i^{-1}$) and almost isotropic.

In the real upstream region of the Earth's bow shock, the difference in the wave polarization spectrum is also observed. Fig. (2-20) shows the observed wave spectrum in the two cases of observations. The spectrum in the left (right) Panel is observed when the distribution shape of the upstream diffuse ion is isotropic (mushroom) type. As expected above, the wave form when the mushroom diffuse ion distribution is observed, shows strong left-hand polarized wave. The wave simultaneously observed with the isotropic diffuse ion, on the other hand, shows nearly same power level in both right and left-hand components.

The observed wave spectra have high-frequency tail which is corresponding to the short wavelength tail in a real space. By calculating ion trajectories in the wave field whose spectrum is based on the observed form, we confirm such contribution of background wave components

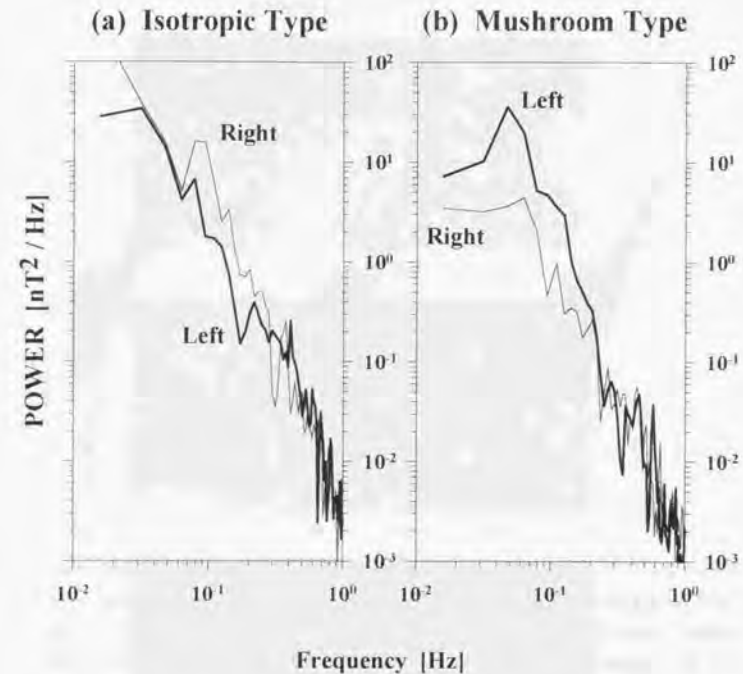


Figure 2-20. Power spectrum of upstream waves observed by GEOTAIL for the case simultaneously observed a nearly isotropic distribution (left) and a mushroom distribution (right). Nearly balanced powers in right- and left-hand polarized wave are seen in left Panel, on the other hand, strong left-hand polarized wave is observed in right Panel. Since the waves are convected by the solar wind flow, the observation is effected by the Doppler-shift.

is weak and the pitch angle changes mainly come from the ion trapping motion in the large amplitude wave. Fig. (2-21) shows the wave spectrum in wave number space. Panel (a) shows the case where dominant right-hand components are superposed with background components.

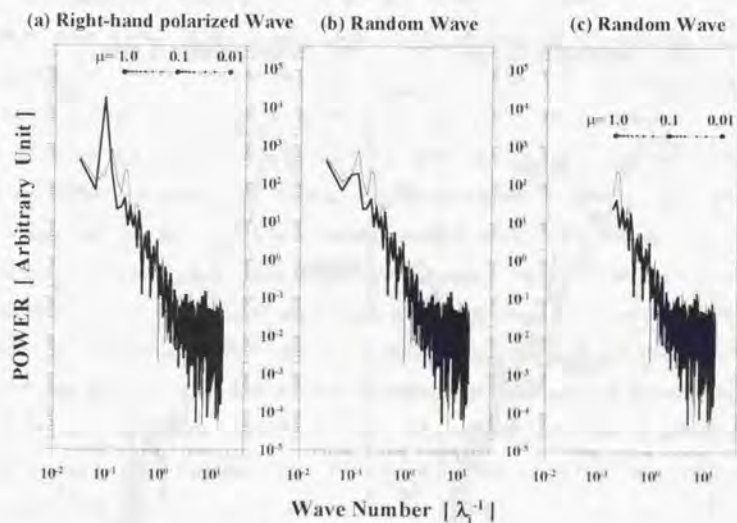


Figure 2-21. Wave spectrum in wave number space for the test particle simulations. Panel (a) is in the case of dominant right-hand waves with background nearly power-law spectrum. Panel (b) is in the case of only the background spectrum. Panel (c) is in the case for selected wave number range in the background spectrum. The lower cut-off range in Panel (c) is determined by the ion with $\mu = \pm 1.0$ and $|v| = 5.0 V_A$. The power of background components is the same in each panel and there is no compressional component ($B_x = \text{const.}$). The wave phase is randomly distributed. The power density of the dominant component in Panel (a) is about 5.8 times larger than that of the total background components.

Panel (b) shows the case where waves are constructed by only background components. The energy densities of background components are the same in (a) and (b), and the waves have random phase spectrum. There is no compressional component ($B_x = \text{const.}$) Fig. (2-22a) – (2-22c) show the pitch angle distribution in the same format as Fig. (2-19) for the waves in Fig. (2-21a) – (2-21c), respectively. The density profile for the dominant right-hand polarized wave

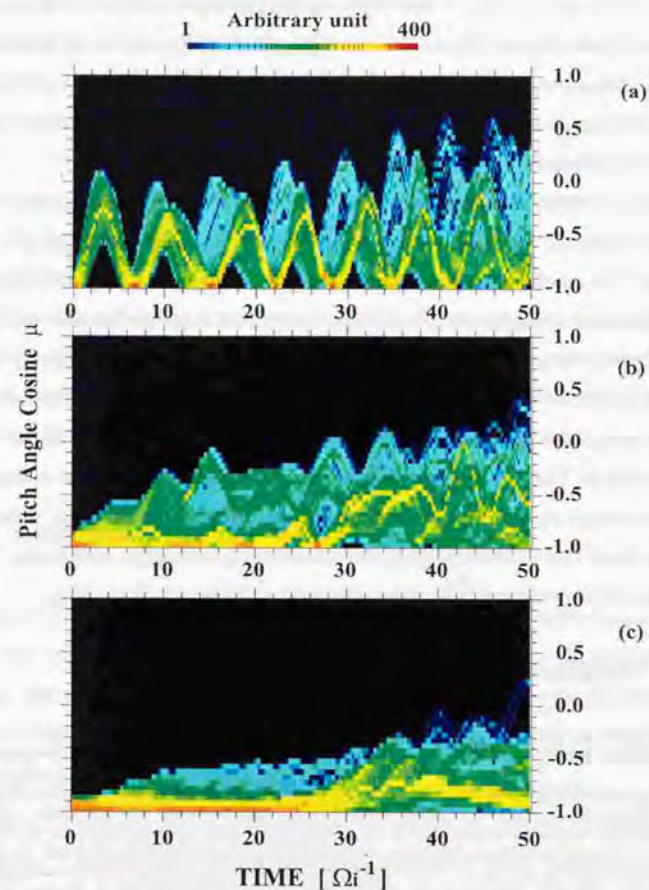


Figure 2-22. Pitch angle distribution versus time in the same format as Fig. (2-19) for the wave given in the wave spectrum in Fig.(2-21). The density profile for the dominant right-hand polarized wave (Panel (a)) is bunched in time which resemble with Fig. (2-19a). The contribution of the background component is weak. With only the background components, ions' pitch angle is changed more slowly and narrower than those of the right-hand polarized wave case (Panel (a)). But the pitch angle changing in Panel (b) is derived from the trapping process, which is confirmed by the comparing with the results of Panel (c). From the difference between Panel (b) and (c), lower wave length components below the $\mu = \pm 1.0$ contribute to the pitch angle changing in Panel (b).

(Panel (a)) is bunched in time as is observed in Fig. (2-19a). The contribution of the background components is still too weak to invalidate the trapping scenario. In contrast, the profile in Panel (b) does not extend to wide region. With only the background components, ions' pitch angle changes more slowly and the distribution is narrower than that of the dominant right-hand polarized wave (Panel (a)) because the wave amplitude is small.

According to the quasi-linear scenario, the short wavelength components contribute to the pitch angle scattering, especially to the ion which have slow parallel velocity or $\mu \sim 0$ in the wave frame. The contributions of the long wavelength components are not treated. Here we set the wave spectrum as only the short wavelength components which can resonate with ions (Fig. (2-21c)). The lower cut-off range corresponds to the longest wavelength determined by the pitch angle cosine $\mu = 1$ for $|v| = 5 V_A$, as denoted upper bar in Fig. (2-21). Again the energy density of background components are the same in (b) and (c). Fig. (2-22c) shows the pitch angle distribution. The diffusion time scale is consistent with the quasi-linear scenario. Ions' pitch angle changes more slowly and the distribution is narrower than that of the random phase wave case (Panel (b)) which is including non-resonant long wavelength components. Thus we confirm that the non-resonance waves strongly work on the pitch angle changing.

2.3.5 Summary of Simulation

In this section, we have performed test particle simulations to investigate the pitch angle changing process in the various wave forms, especially in large amplitude wave fields. In a large-amplitude monochromatic wave, the changing is due to phase-trapping oscillation as shown in the trajectory in Fig. (2-15e), which is different from the quasi-linear scenario because in the small amplitude wave the changing is derived from the pitch angle diffusion. So these two processes of oscillation and diffusion are distinct each other, that is, the oscillation is concerned with a non-scattering motion and the diffusion process is concerned with a scattering motion. The results we have first shown in this section 2.3.3 are the pitch angle changes derived from non-scattering process. The important difference between non-scattering (phase-trapping scenario) and the scattering (quasi-linear scenario) process is the time scale for the pitch angle changing. The pitch angle changing in the trapping motion occurs as fast as the gyro-motion

which is about 10 [sec.] for the actual upstream parameters.

We insist that the formation mechanism of the ion pitch angle distributions for the upstream diffuse ions is different from the conception of diffusion. If the ions are injected for a quite limited short-time interval in contrast to the continuous injection assumed in previous section, the pitch angle distribution varies in time and does not show 'mushroom' but bunched distribution in a certain pitch angle range in early time stage ($<$ several tens Ω_i^{-1}) as shown in Fig. (2-15d) (around $\Omega_i t \sim 4, 11, 18$, their pitch angle are restricted between -0.5 and 0.1). The 'mushroom' distribution is produced (1) in later time (\geq several tens Ω_i^{-1}) because the bunching period is different each other for initial phase θ_{i1} , and (2) under the assumption that the ions are injected continuously. And also if the observation is made with lower-time resolution instrument than ion gyro-period, these phase trapped oscillation is smeared out and the ions can show the 'mushroom' type pitch angle distribution.

2.4 Summary

From the GEOTAIL observation we have shown that the 'mushroom' distribution exists in the far upstream region. This is characterized by the half-hemisphere on the escaping side by seemingly well 'scattered' distribution. On the other hand, near the shock, the distribution shows isotropic. Within about 30 Re distance from the earth, the wave activity is enough large to change the ion pitch angle.

We have concluded that the wave-particle interaction process working in the earth's upstream region is not the scattering process derived from the cyclotron resonance process but the non-scattering motions in the large amplitude waves which are concerned with the phase trapping motion. In the circularly polarized monochromatic waves, the ions change their pitch angle to be observed as a 'mushroom' distribution if the amplitude is large enough (in this case, $B_w / B_0 > 0.1$). One of the contribution processes to distribute the ions' pitch angle to be isotropic (i.e. from $\mu = -1$ to $+1$), is co-existence of the right-hand and left-hand polarized waves. The co-existence wave is the linear polarized wave. The linear polarized waves can be excited from the wave steepening process of the upstream waves if the wave amplitude is large enough and the

wave is propagating oblique direction. Since it has been reported in some numerical simulations [e.g. Scholer *et al.*, 1992] that the waves are propagating oblique direction near the shock, the linear polarized waves are excited near the shock region and the isotropic distribution are frequently observed in this region.

Chapter 3

Ion Motion around the Parallel Shock

3.1 Introduction

Collisionless MHD shocks have been considered as an accelerator for charged particles to high energy range in the two different processes: scatter-free and statistical scattering process. In the former process called *shock drift acceleration* (SDA), particles gain energy near the shock surface by their drift owing to field gradient along the motional electric field [e.g. Armstrong 1985, Decker 1988 for review]. Since the electric field appears under the condition that there is a finite angle between the magnetic field and the fluid velocity, this acceleration works mainly in a quasi-perpendicular shock. In the latter process called *diffusive shock acceleration* (DA), particles are scattered in the wide region of the shock upstream/downstream and cross the shock surface many times [e.g. Blandford and Eichler 1987 for review]. The elastic scattering process in the upstream region leads to acceleration in shock frame. Since the small shock angle enables the particles to cross easily the shock, this acceleration process has been mainly applied to a quasi-parallel shock. These two processes do not imply a conflict problem because they are conceptually different methods and are used differently, and sometime used for co-existing processes in a quasi-perpendicular shock [Decker and Vlahos, 1985, 1986]. At the method level, for studies of SDA process it is a good analytical method that individual particle trajectory is numerically calculated in given field configuration. For studies of DA process the diffusion-convection equation is used to find analytical solution under the assumption of the isotropic ion distribution. Monte-Carlo simulation applies to find numerical solutions [Ellison, 1985].

Although DA process has been only treated in the quasi-parallel shock, it is recently presented by numerical simulations in hybrid code that the SDA mechanism works even in the

quasi-parallel shocks [Scholer, 1990; Kucharek and Scholer, 1991]. Large amplitude upstream waves which are excited by accelerated ions themselves are convected to the shock surface, and let the local instantaneous shock angle θ_{ion} oscillate with the wave frequency. Since the wave amplitude is the same order as the ambient magnetic field, θ_{ion} exceeds 45° even if the wave-phase-averaged shock angle $\langle \theta_{\text{ion}} \rangle$ is $\ll 45^\circ$. In addition, the wave frequency is the same order as the proton cyclotron frequency, so that ion motions around the shock are affected by the existence of the wave. In this chapter, we reconsider the following two topics: (1) ion acceleration process and (2) ion reflection process of the incoming ions at the shock surface. Scholer [1990] and Kucharek and Scholer [1991] have suggested that even in the quasi-parallel shock region, ions are accelerated by the SDA process because of this modification of θ_{ion} . They observed that ions are staying for a long period of time (about 50 ion gyro-periods) close to the shock, and are accelerated during this time interval. Lyu and Kan [1993] has shown that the reflection process depends on the phase angle of the magnetic field in the shock tangential plane. As is shown in what follows, the acceleration process observed by Scholer [1990] and Kucharek and Scholer [1991] and reflection process observed by Lyu and Kan [1993] can be understood in term of scatter-free motion of ions being trapped by large amplitude waves convected from upstream to downstream across the shock surface.

In the previous Chapter we have shown that the importance of the resonance type pitch angle scattering process is weak in the large amplitude wave field. This implies that in such field the scatter-free process is more important than the statistical scattering process. This implication leads us to start a test particle simulation where ion motions around the parallel shock are followed in the presence of a monochromatic large amplitude waves.

The equation of ion motion is the same as the previous Chapter. In contrast to the studies in the uniform field in the previous Chapter, here we have set the shock discontinuity in the simulation box where the wave phase velocity is reduced and the amplitude is increased from an upstream to a downstream side. In section 2, we show the basic conception for the acceleration process which is different from both the shock drift acceleration and the diffusive shock acceleration processes. Following the ion motions in the given wave field we calculate the velocity increasing phenomena in section 3, and the reflection phenomena of the incoming solar wind ion in section 4.

3.2 Basic Equation for Acceleration Process

The basic ion motion is the same as the section 2.3. 1-dimensional space is set in \mathbf{X} axis. The monochromatic Alfvén wave is circularly polarized and propagating along the ambient magnetic field \mathbf{B}_0 ($\mathbf{B}_0 \parallel \mathbf{k} \parallel \mathbf{X}$) with local Alfvén velocity V_A . The velocity, time and length are normalized to the upstream Alfvén velocity V_{A1} , inverse proton gyro-frequency Ω_i^{-1} , and ion inertia length λ_i . In this Chapter, instead of the wave frame, ion motions are calculated in the shock frame. A plane shock is located at $x = 0$ and $+\mathbf{X}$ directs from upstream to downstream side. In the upstream region, the Alfvén wave is propagating upstream-ward ($-\mathbf{X}$ direction) in the solar wind fluid frame. Since the solar wind speed is super-Alfvénic (Mach number = M_A), the wave is convected to the shock. The phase velocity of the upstream Alfvén wave V_{w1} in the shock frame is $V_{w1} = (M_A - 1)$.

The equation of motion of an ion in the shock frame is given by

$$\frac{dv}{dt} = -\Omega v \sin \theta \quad (3.1)$$

$$\frac{dv_{\parallel}}{dt} = \Omega(v_{\parallel} - V_w) \sin \theta \quad (3.2)$$

$$\frac{d\theta}{dt} = -\Omega_i - k(v_{\parallel} - V_w) + \Omega \frac{(v_{\parallel} - V_w)}{v_{\perp}} \cos \theta \quad (3.3)$$

Particle energy is described in the shock frame,

$$\frac{d}{dt} [v_{\perp}^2 + v_{\parallel}^2] = -\Omega V_w v_{\perp} \sin \theta = V_w \frac{dv}{dt} \quad (3.4)$$

and is conserved in the local wave frame,

$$\frac{d}{dt} [(v_{\parallel} - V_w)^2 + v_{\perp}^2] = 0 \quad (3.5)$$

As shown in Fig. (2-14), an ion changes its velocity components in time but motions are restricted on a circle whose center is the wave phase velocity V_w .

Here we apply this motion to shock discontinuity region. Since the fluid velocity is reduced at the shock, the wave phase velocity also reduces from V_{w1} (upstream) to V_{w2} (downstream). This difference in V_w leads to the subsequent acceleration of ions as described in Fig. (3-1). Consider an ion in the upstream region which is moving on the thin solid circle whose center is V_{w1} . Note that a positive parallel velocity directs from upstream to downstream direction.

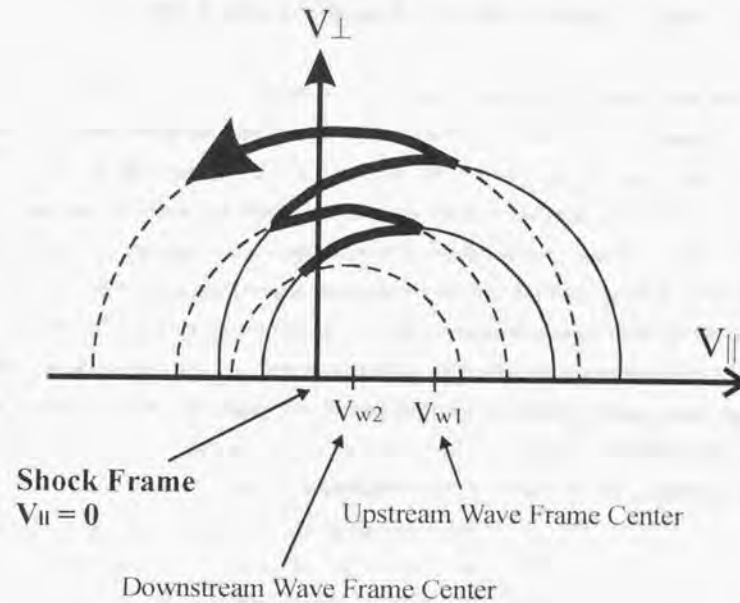


Figure 3-1. In the same format as Fig. (2-14). In the upstream region an ion is moving on a circle (thin curves) centered by V_{w1} . After shock crossing from upstream to downstream region, the ion trans-ride to another circle (dotted curves) centered by V_{w2} . Repeating the trans-riding motion, the total velocity is accelerated in the shock frame.

When an ion moving in the upstream region is accelerated in shock frame, its parallel velocity (v_{\parallel}) increases and it eventually crosses shock surface to the downstream region. To come back to the upstream region, this ion should get a negative v_{\parallel} during its motion in the downstream region (dashed curves centered at V_{w2}). This is what is drawn by thick curve with arrow along which the ion is accelerated. While this picture at first sight looks similar to the second-order Fermi acceleration in an MHD turbulence, there are important differences. First, in a usual second-order Fermi process, there is a finite probability for an ion to move on the same

trajectory (thick curve) with in the opposite direction so as to lose its energy. In the present process, such an energy-losing trajectory does not appear. Along such energy-losing trajectory, ions should have positive v_{\parallel} to cross the shock from downstream to upstream region. With positive v_{\parallel} , however, ions do not cross the shock to upstream region because they are moving to downstream direction. Second, the bouncing motion between upstream and downstream region is not derived from the scattering motion but non-scattering motion.

To cross the shock many times ions have to be trapped around the shock region. If the phase angle θ is bunched and oscillated around 0 or π , the parallel velocity also oscillated around 0 because a sign of the parallel velocity is determined by phase angle θ though $[\sin \theta]$ (Eq. (3.1)). The dependence of the velocity changing on θ and v_{\parallel} is illustrated in Fig. (3-2). The ion whose phase θ is $\pi < \theta < 2\pi$ ($0 < \theta < \pi$) in the upstream (downstream), is oscillating around $v_{\parallel} = 0$ so that, the ion is oscillating and staying around the shock. At the same time, the perpendicular velocity increases as described in Fig. (3-1)

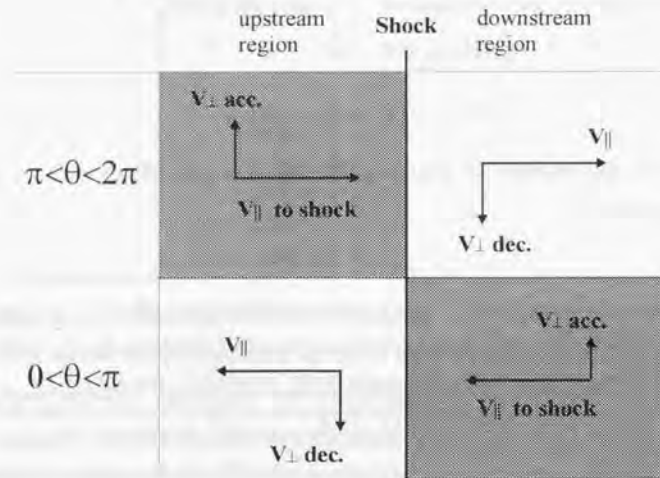


Figure 3-2. Categories of ion motion determined by phase θ . Ions in hatched area can return to the shock region and are accelerated in perpendicular region. If ions can not enter the hatched area, they are injected to far upstream/downstream region.

3.3 Ion Acceleration around the Shock Discontinuity

We perform the test particle simulations to study ion acceleration process described in previous section. To investigate only the effects of the wave-phase-velocity difference between an upstream and a downstream side, purely parallel shock case ($\theta_{0N} = 0^\circ$) is investigated.

Shock transition profile is determined to satisfy the Rankine-Hugoniot relations (hereafter R-H relations). Parameters to determine the shock structure are Alfvén Mach number M_A and upstream plasma β_1 . Parameters to determine the upstream wave are wave length λ_1 and amplitude B_{w0} . Downstream parameters are determined from these upstream values using R-H relations. The values between upstream and downstream side are connected by tangent hyperbolic function with the shock scale length E_s . The detail equations for R-H relations and the tangent hyperbolic function are described in Appendix C and D. Fig. (3-3) shows example of a shock transition profile for $M_A = 6$, $\beta_1 = 1.0$, $\lambda_1 = 50 \lambda_i$, $B_{w0} = 0.5$ and $E_s = 0.5$. Shock is located at $X = 0$.

The right-hand polarized wave are given by the following equations

$$B_y(x, t) = B_w \cos(kx - \omega t) \quad (3.6)$$

$$B_z(x, t) = B_w \sin(kx - \omega t) \quad (3.7)$$

Note that the wave frequency ω is constant, that is the wave phase velocity and wave number satisfy the relation

$$\omega = V_w(x)k(x) \quad (3.8)$$

To derive how long the ions can stay near the shock and how much they are accelerated, numerical computations of the basic Eqs. (3.1) ~ (3.3) are performed for various initial phase angle θ_0 . To describe the basic motion around the shock discontinuity we first set simple shock transition profiles where the downstream waves excited by the upstream waves are only negative propagating waves ($\partial B_z^+(x) / \partial B_1 = 0$, see Appendix D). Later positive propagating waves are included. Fig. (3-4) shows one of the trajectories versus time (Panel (a)). From Panel (b) to (e), parallel, perpendicular components of velocity, total ion velocity $|v|$ (thin curve in shock frame and thick curve in wave frame), and phase θ are plotted versus its position relative

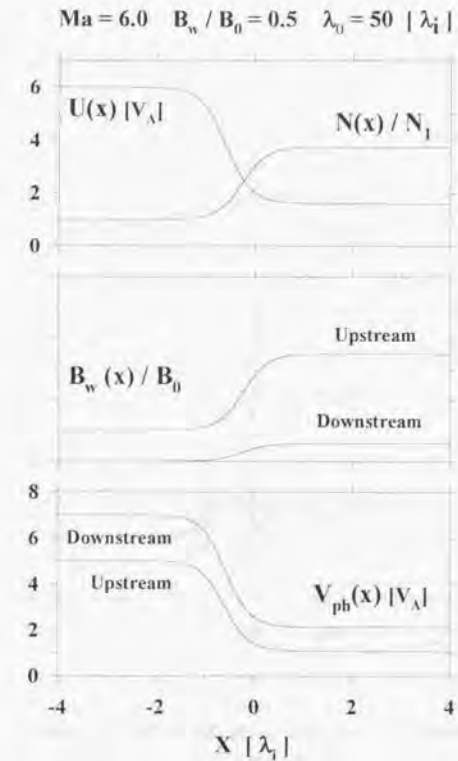


Figure 3-3. Profiles of fluid velocity $U(x)$, density $N(x)$, wave amplitude $B_w^+(x) / B_0$ and wave phase velocity $V_{ph}(x)$ for our test particle simulations. Shock is located at $X = 0$. The 'downstream' ('upstream') means the waves propagating to downstream (upstream) direction. The upstream propagating upstream waves excite two waves in the downstream region (see Appendix D). Fluid velocity is connected by tangent hyperbolic function between upstream and downstream side (see Appendix D). The parameters are shock Mach number $M_A = 6$, upstream wave amplitude $B_{w0} = 0.5$ upstream wave length $\lambda_1 = 50 \lambda_i$, upstream plasma $\beta_1 = 1.0$ and shock scale length $E_s = 0.5$. Density and total field intensity are normalized by far upstream value. Scale is normalized by ion inertia length (λ_i).

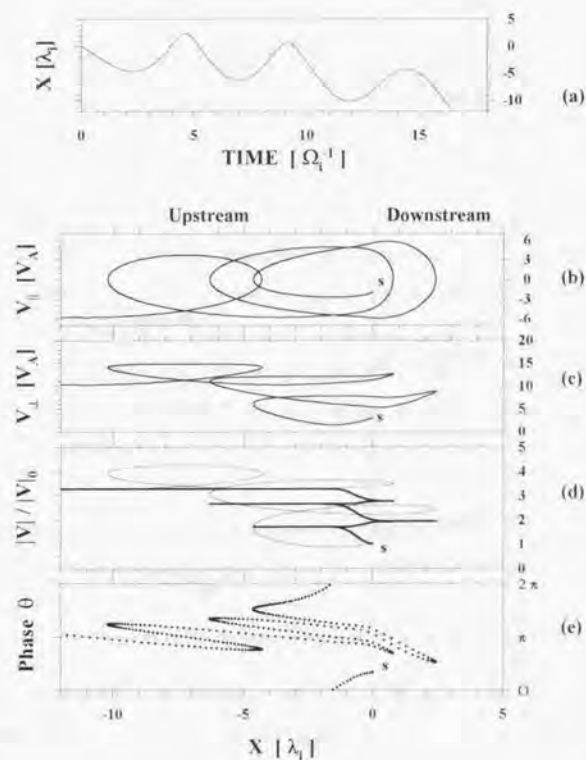


Figure 3-4. One of ion motions calculated in test particle simulations. Plotted are orbit in real space versus time (Panel (a)), velocity components, total velocity and phase θ versus position (Panel (b) - (e)). Trajectories start from $X = 0$ denoted by symbol "s". Initial values are $v_{\parallel} = -2.0 V_A$, $v_{\perp} = 3.0 V_A$ and $\theta_0 = 60^\circ$. Ion energy is calculated in wave frame (thick curve) and shock frame (thin curve) in Panel (d). They are normalized by their initial value. Phase angle is plotted by every $0.05 \Omega_1^{-1}$. The parallel velocity is oscillating around $v_{\parallel} = 0$ which is enable to cross the shock many times. When the ion goes out of upstream system boundary ($-12 \lambda_1$), the velocity intensity is about three times larger than that at the initial value and phase angle is restricted around π .

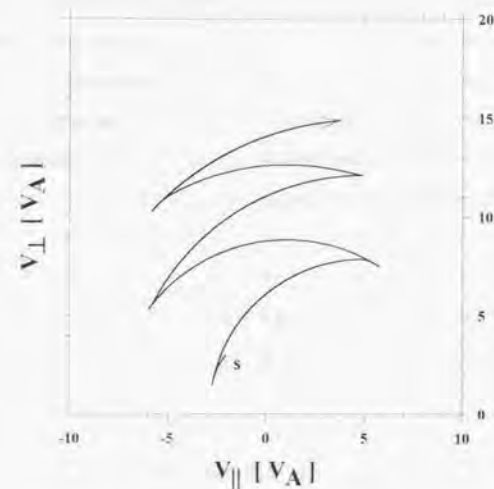


Figure 3-5. Motion in velocity space (v_{\perp} , v_{\parallel}) for the ions described in Fig. (3-4). The particle energy is mainly increasing in perpendicular direction.

to the shock. Fig. (3-5) shows the trajectory in velocity space in the same format as Fig. (3-1). The ion total velocity $|v|$ is normalized by its initial value. Phase angles are plotted every $0.05 \Omega_1^{-1}$. The trajectories start from $X = 0$ denoted by the symbol "s" with velocity $v_{\parallel 0} = -2.0 V_A$, $v_{\perp 0} = 3.0 V_A$ and $\theta_0 = 60^\circ$. At the end time the ion is going out from upstream boundary ($x = -12 \lambda_1$). The parallel velocity is oscillating around zero to cross the shock several times. The perpendicular component, on the other hand, is considerably increased. Acceleration takes place when an ion crosses the shock as illustrated in Fig. (3-1) (compare Fig. (3-1) with Fig. (3-5)). The gradual increase of $|v|$ in wave frame around $-0.5 < X < 0.5$ is caused by shock transition layer. For oscillating motion of the ion, its phase must be in condition $0 < \theta < \pi$ ($\pi < \theta < 2\pi$) in downstream (upstream) region (Fig. (3-2)). Since the wave length (equivalent with wave phase velocity) is changed at the shock surface, the trajectory of the

phase is bent after shock crossing and satisfies the above phase conditions. The phase angle, however, is not kept at the same angle at $X = 0$ but shifting toward negative. This is because the perpendicular velocity is gradually increasing. Since the trapping feature is determined by the perpendicular velocity as seen in Appendix B, the ion is easily trapped with increasing its energy and is gradually shifting toward π . This shifting leads to the decreasing of the value $[\sin \theta]$, so that the parallel force to oscillate the ion around the shock becomes weaker (Eq. (3-1)), when relative increasing of v_{\perp} is smaller than the decreasing of $[\sin \theta]$.

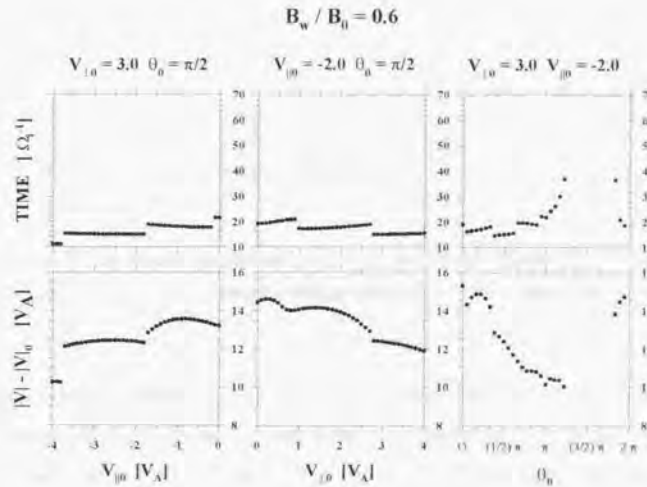


Figure 3-6. A staying time interval around the shock region (upper Panel) and the velocity difference between the final and initial velocity (lower Panel) are plotted versus initial parallel velocity (left Panel), perpendicular velocity (middle) and phase angle (right). These results show for the ions which eventually cross the upstream boundary ($-12 \lambda_s$). As decreasing the staying time interval, the velocity difference becomes also decreasing in left and middle Panels, which comes from the shock crossing number. The dependence on the initial phase angle is drastic. The ion around $\theta_0 = (3/2)\pi$ are injected to downstream region (crossing the downstream boundary at $10 \lambda_s$).

The trajectory in Fig. (3-1) implies that the shock crossing leads the increasing of the energy and the ions which stay for a long time around the shock are highly accelerated. In Fig. (3-6) we check such relation between staying-time-interval and velocity increasing. In the upper Panels show the staying time interval in the simulation box bounded between upstream ($-12 \lambda_s$) and downstream ($10 \lambda_s$) boundary. In the lower Panels shows the velocity increasing of the final velocity from its initial velocity. These are plotted versus initial parallel (left Panel), perpendicular velocity (middle) and phase angle (right). Ions are released at $X=0$ with initial velocity denoted at the top of each panels with the wave amplitude $B_w / B_0 = 0.6$. The ions which eventually cross the upstream boundary are only plotted. The relation between the time interval and acceleration is seen in the left and middle Panels with step-like profile against the initial velocity in v_{\parallel} and v_{\perp} which are the effects of crossing number dependence. But the

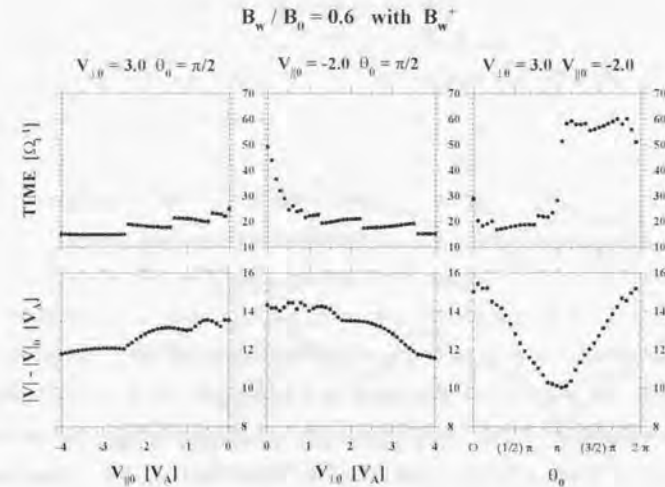


Figure 3-7. Same as Fig. (3-6). The downstream propagating waves are included. The velocity dependence is same as Fig. (3-6). The ion around $\theta_0 = (3/2)\pi$ are back to upstream boundary.

relation is not clear in the right Panel. This is because ion motions are strongly affected by phase angle conditions rather than velocity components. The initial phase dependence also affects the ions' orbit. The lacking of dots around $(3/2)\pi$ in right Panels is caused by the ions which do not cross the upstream boundary but eventually cross the downstream boundary. Whether ions are injected to upstream or downstream region is mainly determined by the phase angle. The velocity increase about $10 \sim 15 V_{A1}$ in $10 \sim 20 \Omega_1^{-1}$ ($\sim 2 \sim 3$ gyro-motion), which is as fast as SDA process.

Next we show the results including the positive propagating wave ($\partial B_z(x) / \partial B_1$). Fig. (3-7) shows the results in the same format as Fig. (3-6). Both time interval and velocity increasing resemble with no positive wave case which suggests that the effects of the positive waves is weak. The effects are seen in (1) lower perpendicular velocity in middle Panel and (2) phase

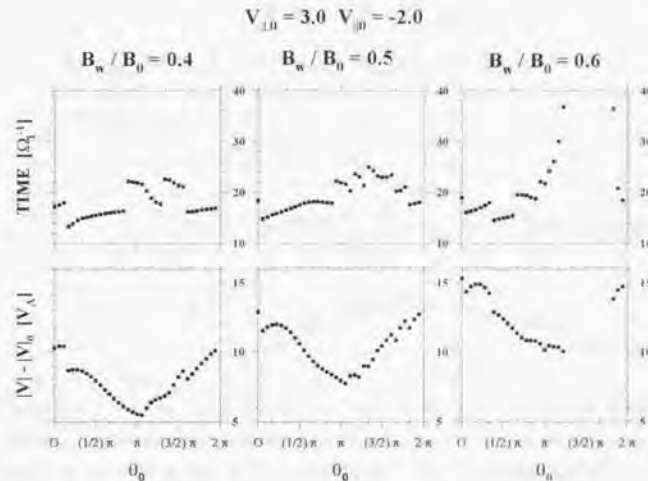


Figure 3-8. The amplitude dependence in the same format as right Panels in Fig. (3-6). Amplitude is $B_w / B_0 = 0.4$ for left, 0.5 for middle and 0.6 for right Panels, respectively. As the amplitude becomes larger, the velocity increases larger.

angle around $(3/2)\pi$ in the right Panels which can cross the upstream boundary instead of downstream boundary. This is because the modulations of the phase angle in the shock transition region or downstream region.

Since the force working on ions is proportional to the wave amplitude through Ω (see Eqs. (3.1) - (3.3)), we expect that the acceleration efficiency increases as B_w becomes large. We have found that this is the case: Fig. (3-8) shows the accelerated values in the same format as the right Panels in Fig. (3-6) for the case of $B_w / B_0 = 0.4, 0.5$ and 0.6 , respectively. Larger amplitude waves clearly accelerate the ions to high energy.

3.4 Ion Reflection at the Shock Surface

The previous observation have shown that a fraction of the incoming solar wind ions are specularly reflected at the quasi-parallel shock surface and confirm ring-like distribution in the velocity space [i.e. Gosling et al., 1982]. Here we investigate ion motions which are released in the upstream region with incoming (positive parallel) velocity. The field profile is the same as previous section where the positive waves are excluded.

Fig. (3-9) shows two typical trajectories to illustrate how the incoming solar wind ions behave at their first arriving at the shock transition layer. From top to bottom, parallel, total velocity, phase, perpendicular positions and perpendicular velocity components are plotted versus their position relative to the shock. The upstream wave amplitude is 0.6. Ions are released in upstream region at $-1 \lambda_c$ with $v_{\parallel} = 5.0 V_{A1}$, $v_{\perp} = 2.0 V_{A1}$ and initial phase $\theta_0 = \pi ((4/3)\pi)$ for left (right) Panel. In the left Panel reflected trajectories are presented. These motions well resemble the trajectories obtained in a perpendicular shock where the reflection and acceleration are described by the SDA process [e.g. Burgess, 1987b]. But the ion is not drifting any perpendicular direction (see bottom two Panels) while it is staying around the shock region. The phase angle of the ion is trapped around π . When it is injected to upstream region, the phase angle is restricted narrow angle around π . In right Panel transmitted trajectories are presented. The ion is not phase trapped but phase rotating and velocity does not increase. From these Panels, it is shown that the initial phase angle is one of the important parameter for the

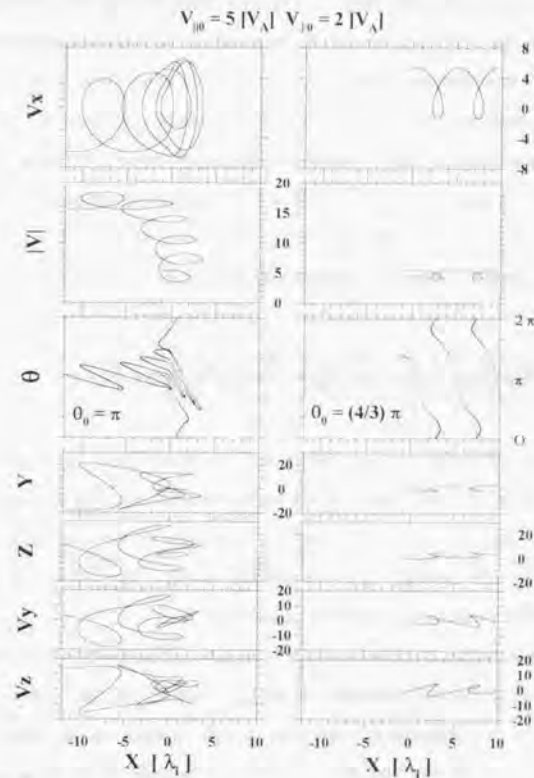


Figure 3-9. Two typical trajectories after their first arriving at the shock transition layer. From top to bottom, parallel, total velocity, phase, perpendicular positions and perpendicular velocity components are plotted versus its position relative to the shock. Ions are released in upstream region at $-1 \lambda_1$ with $v_{\parallel} = 5.0 V_A$, $v_{\perp} = 2.0 V_A$ and initial phase $\theta_0 = \pi$ ($(4/3)\pi$) for left (right) Panel. The upstream wave amplitude is 0.6. The ion in left Panels is reflected and accelerated around the shock. When ion is injected to upstream region, the phase angle is trapped around the π . The orbit resemble with the orbit shown in the shock drift acceleration process (e.g. Burgess, 1987b), but ion does not drift to shock tangential direction. The ion in right Panels is not reflected but transmitted to downstream region without any acceleration.

ion reflection. So, Fig. (3-10) shows the dependence on both initial parallel velocity and phase angle. Plotted region in upper (lower) Panel shows the reflected (transmitted) ion population for their initial parameters. In addition color-coordinated scale shows how the velocity increases from its initial velocity. Black region means deceleration. Their initial perpendicular velocity is $2.2 V_A$. The reflected ions come from a restricted part of the incoming solar wind ion population. Before ions are injected to upstream region, they are accelerated about $10 V_A$. On the other hand, the transmitted ions are not strongly accelerated as seen in Fig. (3-9), and some ions are decelerated.

3.5 Summary and Discussion

We have investigated the ion acceleration and reflection processes by applying the ion motions in the large amplitude monochromatic waves to the shock discontinuity region where the wave phase velocity is different in both side of the shock. The motions strongly depend on their initial condition especially the phase angle θ_0 . Whether ions can stay and cross the shock in many times or not, and how much the ions are accelerated, are mainly determined by θ_0 . Since the phase angle is determined by the accelerated perpendicular velocity, the velocity and phase angle are complexly connected each other. The velocity-increasing-value becomes larger with the larger wave amplitude, which is written in the equation of motion. The forces is proportional to the wave amplitude though Ω . The velocity increases about $10 \sim 15 V_A$ in $10 \sim 20 \Omega^{-1}$ ($\sim 2 \sim 3$ gyro-motion), which is as fast as SDA process. After the interactions of ions with the shock discontinuity, they are injected to upstream region with phase angle trapped around π . This suggests that bunched ions are observed near the parallel shock region. If the observation averaged over the wave frequency (~ 10 sec.), the bunched ions are observed nearly ring shape distribution [Gosling et al., 1982].

In this calculation the ambient magnetic field directs positive direction and the Alfvén wave is propagating to negative direction. From Walén relation, the incoming ions' fluid velocity is in the same phase as the upstream waves, that is, most of the incoming ions distribute around $\theta \sim 0$. On the other hand, the reflection process is seen for a portion of the incoming solar

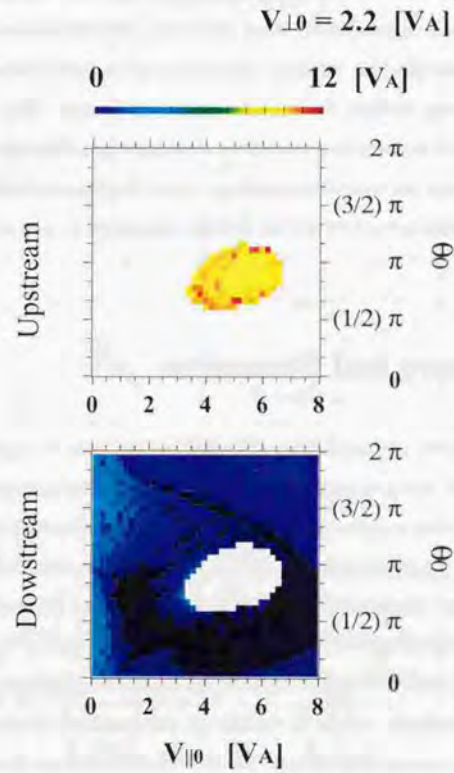


Figure 3-10. The dependence of ions' reflection motion on their initial parallel velocity and phase angle. Upper panel shows the ions which are eventually reflected and injected to upstream region. The color-coordinated scale shows how their velocity increase from their initial to final velocity. The final velocity is measured when the ions cross the upstream boundary at $12\lambda_s$ from the shock. The acceleration scale is noted in the upper bar. Black region means deceleration. Reflection takes place for a restricted part of the incoming ion population. On the other hand, lower Panel shows for the transmitted ions, which eventually cross the downstream boundary $10\lambda_s$. All the reflected ions are accelerated, but the transmitted ions are not always accelerated.

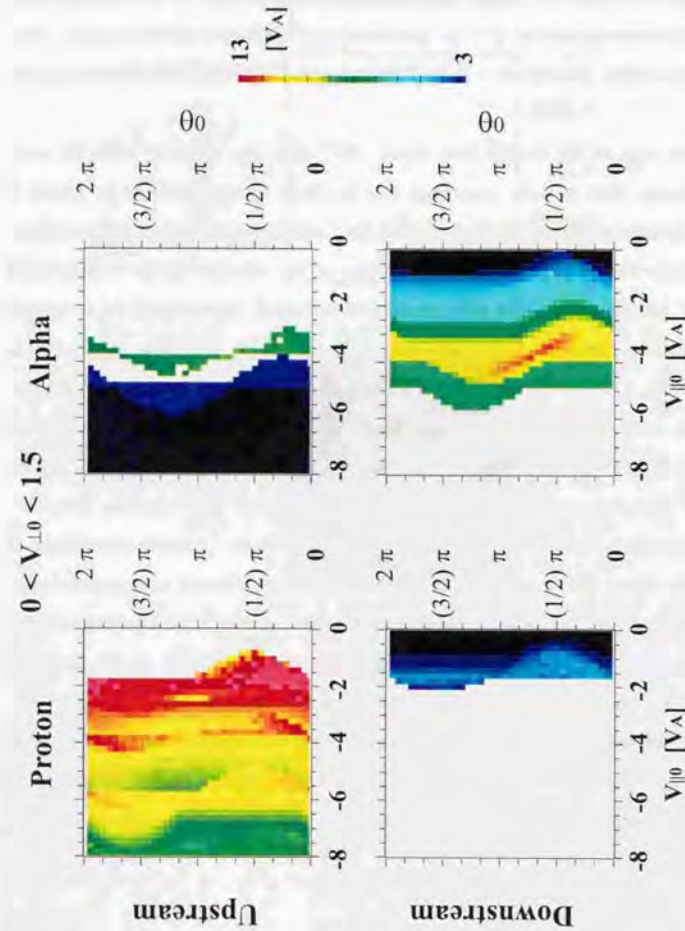


Figure 3-11. The dependence of the velocity increasing in their initial parallel velocity and phase plane with color coordinated scale for proton (left) and He^{++} (right) in the same format as Fig. (3-10) for negative initial parallel velocity. Upper (lower) panels shows the ions which eventually cross the upstream (downstream) boundary. The acceleration for He^{++} takes place in more restricted parameters than those of proton.

wind which have near $\theta \sim \pi$ (see Fig. (3-10)). So, the most of incoming ions result in the downstream ions which is consistent with the small density of the upstream diffuse ions ($\sim 1 - 2\%$ from observation) relative to solar wind ion density. The tail part of the incoming solar wind distribution which reaches to $\theta \sim \pi$, is reflected and injected to upstream region. Note that the reflection takes place at $\theta \sim 0$ for incoming ions if ambient field directs opposite direction.

In the diffuse ions of the earth's bow shock, He^{++} ions are observed with the same composition density ratio as solar wind ions and the same energy spectrum as proton if represented in energy per charge. We also calculate He^{++} trajectory in the same field condition. About acceleration, Fig. (3-11) shows the dependence of the velocity increase in their initial parallel velocity and phase plane with color coordinate scale. Left (right) Panels are for proton (He^{++}). Their initial perpendicular velocity is between 0 and $1.5 V_A$. The wave amplitude and length is 0.6 and $50 \lambda_s$, respectively. Most of He^{++} eventually cross the downstream boundary. The acceleration takes place in more restricted parameters than those of proton. The value of velocity increase for He^{++} is about 9 at $v_{\parallel 0} = -3.5 V_A$, $\theta_0 = (2/3)\pi$. The same profile between proton and He^{++} in energy per charge means that the proton speed is $\sqrt{2}$ times faster than He^{++} speed. Since the proton velocity-increase is about $10 \sim 15 V_A$, the He^{++} velocity-increasing ($\sim 9 V_A$) is reasonable values. However, since He^{++} is accelerated and injected to upstream region from the restricted parts of the initial parameters, their relative density after the acceleration at the shock become smaller than that for the source ions. About reflection, Fig. (3-12) shows the dependence on both initial parallel velocity and phase angle in the same format as Fig. (3-10). Their initial perpendicular velocity is between 2.0 and $2.5 V_A$. Most of He^{++} are not reflected at the shock surface, so that the density of He^{++} is less than the composition ratio in the solar wind. Here the injection problem has also been yet remained unsolved. About the motions of the He^{++} , we set the future works.

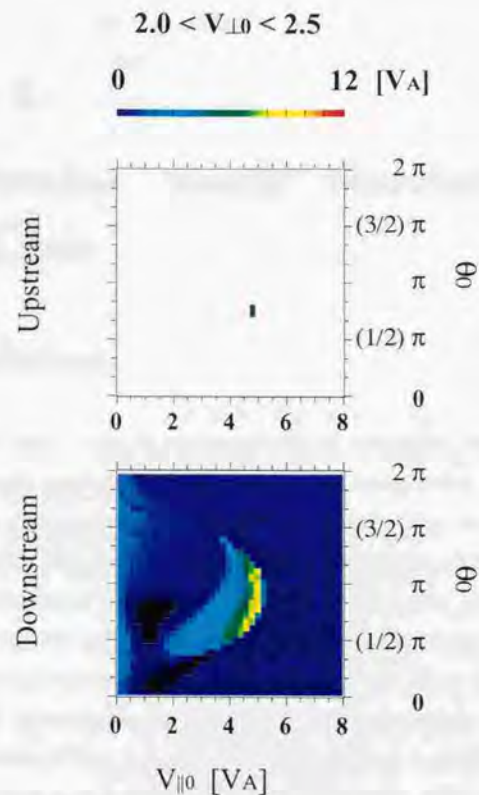


Figure 3-12. Same as Fig. (3-10) but for He^{++} . Most of particles result in downstream particles.

Chapter 4

Quasi-Parallel Shock Simulations in Hybrid Code

4.1 Introduction

After the over 30 years history of extensive studies of collisionless shocks, the physical processes at fast-mode quasi-parallel shocks remain under consideration. In contrast to the quasi-perpendicular shocks which are well defined and have sharp transition layer from upstream to downstream side, the quasi-parallel shocks show complex nature. Large-amplitude MHD waves are observed in both upstream and downstream region, and the waves often obscure the shock transition layer. Ion distributions in the upstream side are contaminated with more energetic ions backstreaming from the shock to the upstream region. In the vicinity of the quasi-parallel shock, backstreaming beams of relatively cold ions are observed [Gosling *et al.*, 1989]. The distribution of these beam ions in the velocity phase is consistent with specular reflection of the incoming ions at the shock surface [Onsager *et al.*, 1990]. On the other hand, in widely upstream region there observed so-called diffuse ion distribution which have broader pitch angle distribution and energy spectrum extending to several hundred keV [e.g. Ipavich *et al.*, 1981a].

Numerical simulations of quasi-parallel shocks have been carried by many authors. To retain the kinetic effects of ions, the most effective simulation code is the hybrid code where ions are treated as super-particles, while electrons are charge neutralizing massless fluid. Quest [1988] performed his simulations under the exactly parallel shock condition ($\theta_{BS} = 0^\circ$). He found that backstreaming ions excite the resonant electromagnetic waves. During convection by the upstream fluid, the waves are amplified and scatter the backstreaming ions. The simulations for

quasi-parallel shocks by *Kan and Swift* [1983] have shown that short-wavelength whistler waves are excited near the shock and these waves also scatter the ions. These authors have suggested that the scattering leads to the necessary dissipation at the shock.

Another interesting phenomena seen in the quasi-parallel shock simulations is the so-called *shock re-formation* which was first reported by *Burgess* [1989a]. He showed that the upstream waves steepen and are amplified as they convected to the shock. The crest newly grows to shock. *Scholer and Terasawa* [1990] have shown that when reflected ion occurs, the shock re-forms new shock in front of the old shock. The ions reflected at the old shock front are trapped between these two shocks and heated, then contribute to the thermalized downstream population.

The generation mechanisms of the high energy diffuse ion population are widely studied around the quasi-parallel shock. Now these two processes are considered (A) Leakage or (B) Acceleration. Leakage model is the leakage ions from the magnetospheric ions through magnetosheath [e.g. *Anagnostopoulos et al.*, 1986, 1998]. The magnetospheric high energy ions merely leak to upstream region without any acceleration. Acceleration model is that low energy ions are accelerated around the shock. About the origin of the low energy ions, two models are considered (1) downstream thermal leakage injection or (2) reflection of the solar wind ions. The thermal leakage injection model assumes that fraction of the shock heated solar wind ions are scattered back from the downstream region and cross the shock into the upstream region. *Lyu and Kan* [1990] have suggested in their simulations that the upstream suprathermal ions are predominantly downstream ions. In the reflection model, a portion of the incoming solar wind ions is reflected at the shock surface. *Lyu and Kan* [1993] has shown that the reflection process is dependent on the phase angle of the magnetic field in the shock tangential plane. These upstream injected low energy ions are accelerated around the shock.

One of the acceleration mechanisms is *shock drift acceleration* (SDA) process. It is mainly developed at quasi-perpendicular shock configuration [e.g. *Burgess*, 1987b]. Because of the gradient of the field intensity between upstream and downstream side, the particles drift parallel to the motional $-\mathbf{V} \times \mathbf{B}$ electric field and are accelerated. The other is *diffusive acceleration* (DA) process. In this mechanism elastically scattering process is assumed, which is due to the small-angle pitch-angle scattering by cyclotron resonance condition with the upstream waves.

The particles which are scattered back toward the shock can gain considerable energy in the shock frame. It is also assumed in this model that the scattering occurs statistically so that the ion pitch angle distribution becomes isotropic in the wave frame. Recently another model is proposed by *Scholer* [1990] and *Kucharek and Scholer* [1991]. The diffuse ions are accelerated from the incident thermal ions to suprathermal energies while staying close to the shock for a long period of time (about 50 ion gyro-periods). The accelerated ions are eventually injected to upstream region. They have suggested that ions are accelerated by the SDA process while they are staying in the vicinity of the shock surface. At a glance of the configuration of the parallel/quasi-parallel shock, the field intensity difference between upstream and downstream is not so large, and motional electric field is weak because of the small angle between \mathbf{V} and \mathbf{B} . But it is suitable in the quasi-parallel condition because, as *Kucharek and Scholer* [1991] have pointed out, the quasi-parallel shocks are locally replaced by the quasi-perpendicular shocks according to the large amplitude of the convecting upstream waves.

In Chapter 3, we have proposed another reflection process and acceleration process of incoming solar wind ions which are different from the previous studies reviewed in above paragraph. The reflection process is also concerned with the wave phase angle at the shock surface as reported by *Lyu and Kan* [1993], but the phase of the perpendicular velocity of incoming ions is also important parameters. In acceleration process, we have set a different view from DA and SDA processes for the ion motion around the shock by means of applying the phase trapping phenomena to the shock discontinuity.

Here we have performed the numerical simulations by the hybrid code where the particle motion and field variances are calculated self-consistently. The main purpose is to check the ion motions which are proposed and studied in the test particle simulations in the previous two Chapters. We check whether the following subjects are represented or not even in the self-consistent simulation system. (1) The incoming solar wind ions are reflected at the shock surface under the expected condition where the phase angle difference (θ) between wave and perpendicular velocity is around π . (2) Ions are accelerated around the shock surface by the proposed acceleration process. (3) The 'mushroom' distribution is constructed in circularly polarized wave field. The changing of the waveform from circularly wave to linear wave contributes the isotropization.

4.2 Hybrid Code Simulation

The hybrid code used here is one dimensional in space (variations only in X) and three dimensional in velocity and fields. Ions are treated as super-particles, while electrons are treated as a charge neutralizing massless fluid. Equations to be solved are,

$$\frac{\partial \mathbf{B}}{\partial t} = -\nabla \times \mathbf{E} \quad (4.1)$$

$$\mathbf{E} = -\mathbf{V}_i \times \mathbf{B} + \frac{1}{\rho} \left(\nabla \times \mathbf{B} - \frac{1}{2} \nabla P_e \right) \quad (4.2)$$

$$\frac{d}{dt} \left(\frac{P_e}{\rho^{\gamma}} \right) = 0 \quad (4.3)$$

for field and

$$\frac{d\mathbf{v}}{dt} = \mathbf{E} + \mathbf{v} \times \mathbf{B} \quad (4.4)$$

$$\frac{d\mathbf{x}}{dt} = \mathbf{v} \quad (4.5)$$

for each ion particles [e.g. Fujimoto, 1992 and references therein]. Magnetic field \mathbf{B} , electric field \mathbf{E} , electron pressure P_e , density ρ and velocity moment for ions \mathbf{V}_i are defined on grid. In this study variables are normalized in the following way magnetic field is normalized by upstream total intensity B_1 , plasma density by upstream density ρ_1 , velocity by the Alfvén speed $V_A \equiv B_1 / (\mu_0 \rho_1)^{1/2}$, pressure by $B_1^2 / (2\mu_0)$, temporal scale by inverse of ion gyrofrequency $\Omega_i^{-1} \equiv (eB_1 / m)^{-1}$, and spatial scale by ion inertia length $\lambda_i \equiv V_A / \Omega_i$.

The parameters to determine the shock system are three upstream quantities. Those are Alfvén Mach Number (M_{A1}), the ratio of plasma pressure to magnetic pressure (β_1), and shock angle (θ_{BS}) between shock normal and magnetic field direction. To produce the shock wave we have used piston method. In one dimensional system, a piston is located at the right hand end. At $\Omega_i t = 0$ the piston is pushed into the system and moving leftward (-X direction) in constant speed. Shock wave is launched in front of the piston and propagating leftward with speed V_{sh} faster than the piston speed. To simplify the calculation, we have transformed the system to the

co-moving frame with the piston (downstream rest frame) in X direction and to the normal incidence frame in shock tangential direction (upstream fluid velocity \mathbf{V}_{in} is parallel to shock normal). Ions are flowing in the system from the left hand boundary with a velocity $\mathbf{V}_{in} \equiv (M_{A1} - |\mathbf{V}_{sh}|) > 0$ and specularly reflected at the right-hand rigid wall (piston) in the $\mathbf{E} = 0$ frame. The magnetic field lies on the X-Y plane in initial stage. The ambient magnetic field directs downstream side ($B_x > 0$). (The geometry is illustrated in Fig. (4-1)). At the both boundaries, the density (ρ), bulk velocity (\mathbf{V}_i) and magnetic field (\mathbf{B}) are fixed in values satisfying the Rankine-Hugoniot relation (Appendix C). We use grid size of $\Delta X = 0.5 \lambda_i$ and time step is $\Omega_i \Delta t = 0.01$. The simulation system is $1000 \lambda_i$ long. At $\Omega_i t = 0$ we have put 200 superparticles per grid. This larger particle number enables to study of the distribution of backstreaming ions in the far upstream region.

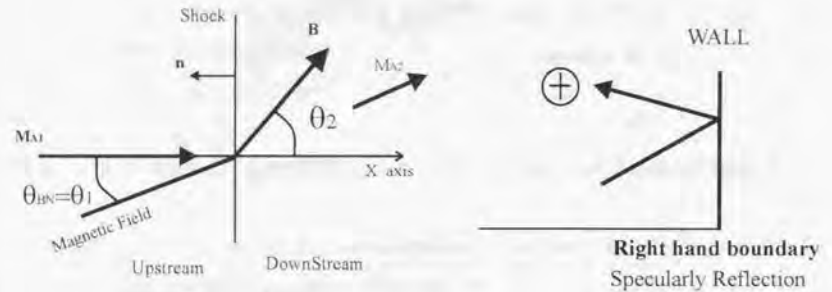


Figure 4-1. The geometry of hybrid simulation in this study. Ambient magnetic field is on X-Y plane with shock angle $\theta_1 = \theta_{BS}$ in upstream region. At the right hand boundary, particles are specularly reflected in the non-electric field ($\mathbf{E} = 0$) frame

4.3 Results

First we show the results from the nearly parallel shock case where the initial shock parameters are $\theta_{BN} = 5.0^\circ$, $M_A = 6.0$ and $\beta_1 = 1.0$ consisting of 0.9 for ions and 0.1 for electrons. Fig. (4-2) shows from top to bottom, the plasma density, and the components of tangential magnetic

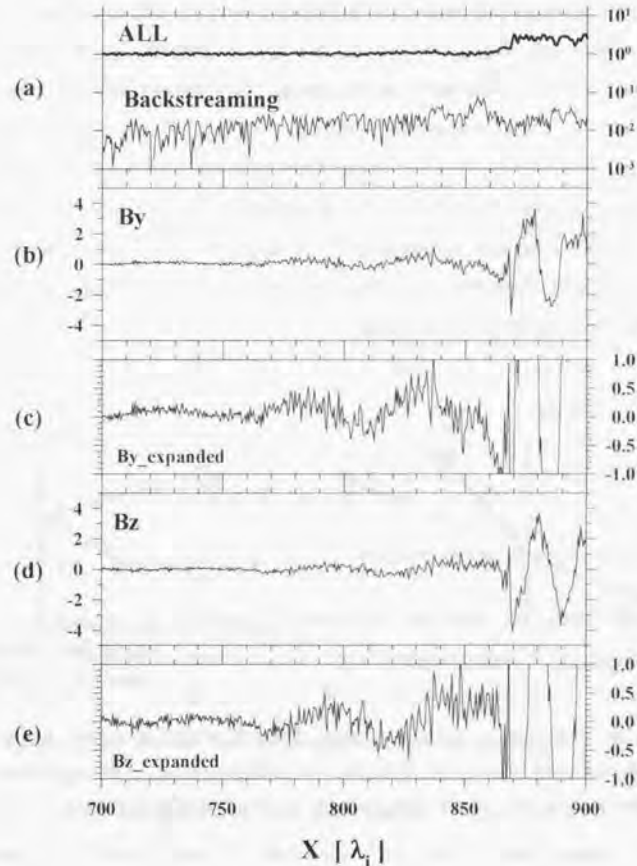
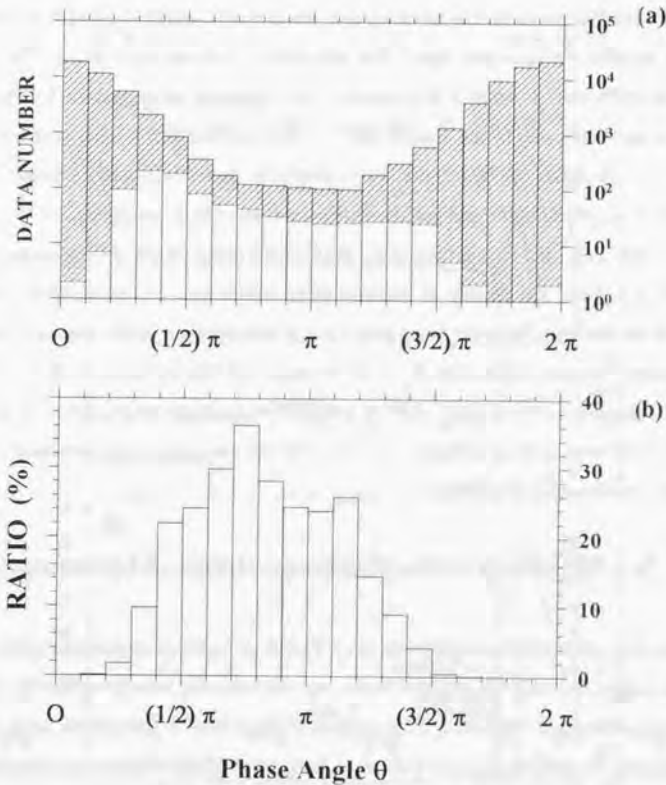


Figure 4-2. Plot of the density (Panel (a)), two components of magnetic field (Panel (b)-(e)) at $\Omega_i t = 85$. Shock is located around $868 \lambda_i$. The density are plotted for total value and for backstreaming ions. The magnetic field components are plotted in different scale for B_y (Panel (b), (c)) and for B_z (Panel (d), (e)). The magnetic wave amplitude is about 0.6 near the shock and decreasing to upstream direction.

field B_x, B_z in different scale (e.g. Panel (b) and (c) for B_y components). The upstream density is subdivided into two populations: incoming and backstreaming ion populations. Each ion is flagged when it has arrived at the shock surface. When the flagged ion has negative velocity v_x in shock frame in the upstream region, it is identified as a backstreaming ion. The shock is located around $\sim 868 \lambda_i$, which is identified by abrupt increasing of the density. Shock position is determined in each step by the density profile, where the density is N times greater than that in a far upstream region. We have chosen $N = 3$ after a try-and-error procedure. In the upstream region, large amplitude right-hand polarized waves are seen whose wave length is $50 \sim 60 \lambda_i$. The amplitude is $B_w / B_0 \sim 0.6$ at the vicinity of the shock and gradually decreasing as one goes to upstream region. The density of backstreaming ions is also decreasing. The waves are excited by the ion beam instability in the early time of simulation run or far upstream region and then they are convected toward the shock on the super-Alfvénic incoming ion flow. The wave length is consistent with the result which is obtained by the linear theory about the ion beam instability with relative beam velocity $\sim 9 \sim 10 V_A$. In the downstream the convected upstream waves are compressed and amplified.

4.3.1 Ion Reflection at the Shock and Origin of Upstream Ions

As known, a fraction of the incoming ions are reflected at the shock surface and injected to far upstream region. In chapter 3, we have shown that the reflection takes place for the incoming ions whose phase angle difference (θ) is around π . Note that θ is the phase angle between ion's perpendicular velocity (\mathbf{v}_\perp) and field wave components (\mathbf{B}_w). To check the dependence on the phase angle, individual ion velocity and upstream wave phase are recorded when the ion has passed at $1 \lambda_i$ upstream from the shock surface. Fig. (4-3) shows the ion phase angle distribution. In Panel (a), the sampled ions' number is plotted. Ions are sampled from $\Omega_i t = 80$ to 120. In white areas show the number of the ions which are reflected and injected over $12 \lambda_i$ upstream from the shock surface (hereafter RI ions). In shaded areas, the numbers of transmitted ion (hereafter TM ion) are shown which have never injected over the $12 \lambda_i$. Panel (b) shows ratio of RI ions to all incoming ion. The RI ions come from around $\theta \sim \pi$. From the Walén relation, most of the incoming ions distribute around $\theta \sim 0$ because the upstream waves



are propagating opposite direction to ambient magnetic field direction. Fig. (4-3c) shows the dependence on both parallel velocity and phase angle about the ratio. This result is consistent with the result of the top of Fig. (3-10). In the parallel shock, a portion of the solar wind ions is reflected and injected to upstream region. The process is mainly determined by the phase angle θ when the ions arrive at the shock surface.

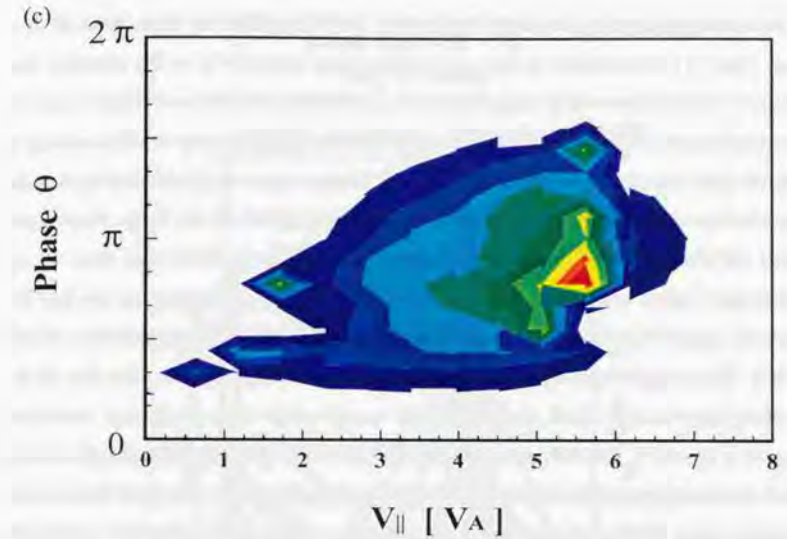


Figure 4-3. Phase angle distributions for the incoming ions which are sampled at $1\lambda_i$ upstream from the shock. (a) White areas show the number of the reflected and upstream injected ion (RI ion). Shaded areas show the number of the transmitted ion (TM ion). From the Walén relation, most of the incoming ions distribute around $\theta \sim 0$ because the upstream waves are propagating opposite direction to ambient magnetic field direction. (b) The composition ratio of RI ion to all the incoming ion. The most of RI ions come from around $\theta \sim \pi$. (c) The composition ratio of RI ion to all the incoming ion in the same format as Fig. (3-10). The maximum ratio is colored by red (~ 0.37). The reflection takes place in the restricted region, which is consistent with the result from the test particle simulation shown in Fig. (3-10).

Tracing backward the entire ion orbit in time, we can show the origin of the upstream and downstream ions. Fig. (4-4) shows the energy spectrum of the ions obtained in the upstream (left Panel) and downstream (right Panel) regions. The energy is normalized by the incoming beam energy. The lowest smooth curve in each panel shows one count level. Ion energies are sampled from $\Omega_i t = 80$ to 90 every 1. In left Panel, the distributions consist

of the upstream ions which are sampled in $20 - 120 \lambda_i$ upstream from the shock. Since $20 \lambda_i$ is larger than the Larmor radius, the just now reflecting ions are excluded in this spectrum. The red curve shows the incoming beam distribution and the black and blue curve show a part of backstreaming ions defined in previous section (backstreaming ion has ever negative velocity v_x in shock frame after it arrived at the shock surface). Blue curve shows the contribution from the ions which have ever penetrated over $10 \lambda_i$ downstream region from the shock. Black curve shows the distribution of the purely upstream ions which have *never* been over $10 \lambda_i$ downstream region from shock. From the scarcity of the blue population, we see that the upstream suprathermal ions mainly consist of reflected ions of the incoming population at shock surface. The energy of backstreaming ions extends to much higher region than that of the incoming ions. In right Panel, the distributions consist of the downstream ions which are sampled in $20 - 50 \lambda_i$ downstream region from the shock. The red curve shows the distribution of the transmitted (non-reflected) ions which have never had negative v_x in shock frame in the upstream region. Black curve shows the contribution from the ions which have ever penetrated over $12 \lambda_i$ upstream region from shock. Blue curve shows the distribution of the ions which have once had negative v_x in the upstream region but never been over $12 \lambda_i$ upstream region from shock. In other words, the ions in blue population are related with the shock dissipation process which have already well been investigated in the quasi-perpendicular shock simulations [e.g. Leroy, 1983]. These ions are reflected at the shock surface and cross the shock without real injection to the upstream region. They construct the hot part of the downstream ion distribution. It is noted that this population is different from the RI ions presented in Fig. (4-3a,b,c). RI is included in black population in each panel. The density of the black population in right Panel is much smaller than that of the other population in the downstream ions and also one order smaller than that of upstream backstreaming ions (black population in left Panel) in the same energy range. It seems to be hard for the accelerated backstreaming ions to cross and be penetrated in deeper downstream region.

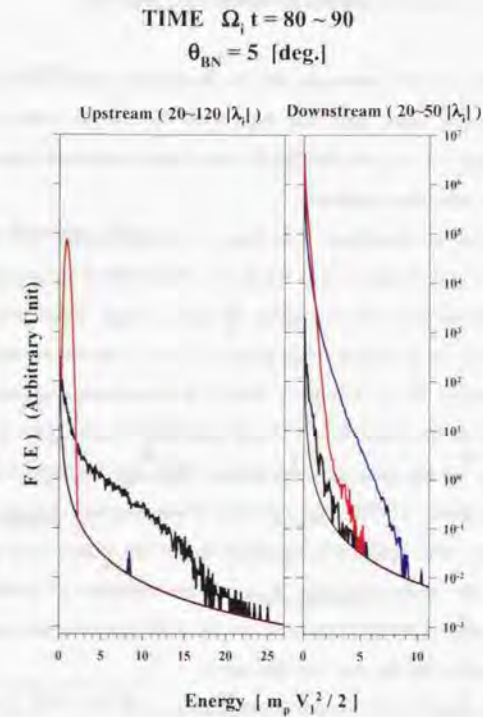


Figure 4-4. Energy spectrum in upstream and downstream regions. In left Panel (upstream region), red population is for incoming ions and black is for backstreaming ions which have never penetrated into downstream region over $10 \lambda_i$. Blue is for backstreaming ions which have ever penetrated into downstream region over $10 \lambda_i$. The origin of the upstream backstreaming ions is reflected-ions at the shock surface. In the right Panel (downstream region), red population is for non-reflected transmitted ions. Blue is for the ions which have been identified as backstreaming ion but have never penetrated into far upstream region over $12 \lambda_i$. Black is for the ions which have been identified as backstreaming ion and have ever penetrated into far upstream region over $12 \lambda_i$. The thermalization of downstream population is derived from the reflection process at the shock surface which is well established in a (quasi-)perpendicular shock region.

4.3.2 Particle Acceleration around the Shock

In previous Chapter, we have presented that the acceleration takes place near the shock by means of shock crossing many times. The large amplitude waves contribute the ions' staying around the shock. Here we have checked the position where acceleration takes place, by means of following particle orbit and its velocity.

Fig. (4-5) shows ion position (Panel (a)/(c)) and ion energy (Panel (b)/(d)) versus time for one of the eventually backstreaming/transmitting ions. The position and energy are calculated in the shock frame. The energy are normalized by the kinetic energy of incoming ions ($E_0 = M_{\infty}^2 / 2$). The negative direction in vertical axis in Panel (a) and (c) represents upstream direction. In Panel (a), an ion starts at $\Omega_i t = 0$ from $x = -430 \lambda_i$ and encounters the shock at $\Omega_i t = 78$. It stays close to the shock for about $\Omega_i t = 15$ and goes to upstream region. Its energy increases considerably during the ion stays near the shock. When the ion stays near the shock, the maximum energy is about 13 times larger than that of incoming ions. Leaving the shock region its energy decreases. After injection to upstream region, the energy stays nearly constant or slightly decreases. This energy loss may be due to the excitation of upstream waves. Most backstreaming ions show a similar behavior: a portion of the incoming ions is caught around the shock and accelerated while they stay near the shock.

To compare the results from the hybrid simulations with that from present test particle simulation, we have plotted the ion motions in the same format as Fig. (3-4) and Fig. (3-5). Fig. (4-6) shows trajectories for the same ion presented in Fig. (4-5a). From Panel (a) to (c), parallel (v_x), perpendicular ($\sqrt{v_y^2 + v_z^2}$) components of velocity, total ion velocity $|v|$ in shock frame versus relative shock position are plotted for $60 < \Omega_i t < 80$ from a part of Panel (4-5a). Panel (d) is in v_z versus v_x . The motions resemble with the results in test particle simulation (see Fig. (3-4) and Fig. (3-5)), especially, while the acceleration occurs around the shock, the perpendicular velocity is increasing (see Panel (d)). As shown in Section 3.3, the reflection (returning) process is different from the stochastic scattering process. And the perpendicular velocity increasing is not derived from the adiabatic motion by the increasing of the field intensity at the shock surface, but from the trans-riding process between upstream and downstream wave frame. In the each wave frame, the increasing/decreasing of v_x is derived

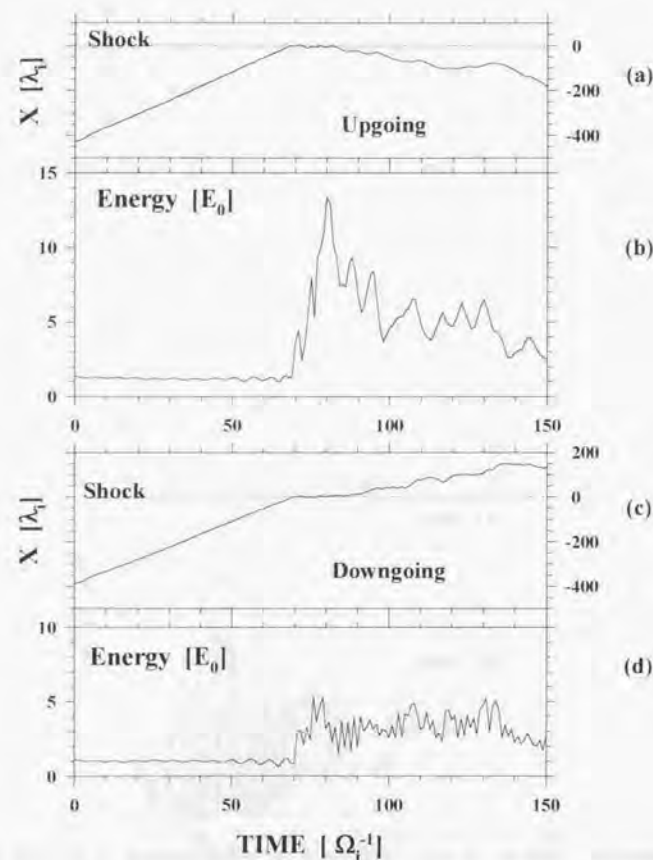


Figure 4-5. Ion trajectories for eventually injected to upstream region (Panel (a), (b)), and downstream region (Panel (c), (d)). In Panel (a) and (c), the trajectories are shown by thick curves in the shock frame (Shock is located at $X = 0$). The energy ($v^2 / 2$) is normalized by the kinetic energy of the incoming ion ($E_0 = M_{\infty}^2 / 2$). After arriving at the shock, ions are staying vicinity of the shock for several times, and leave from the shock. While their staying, the energy increases.

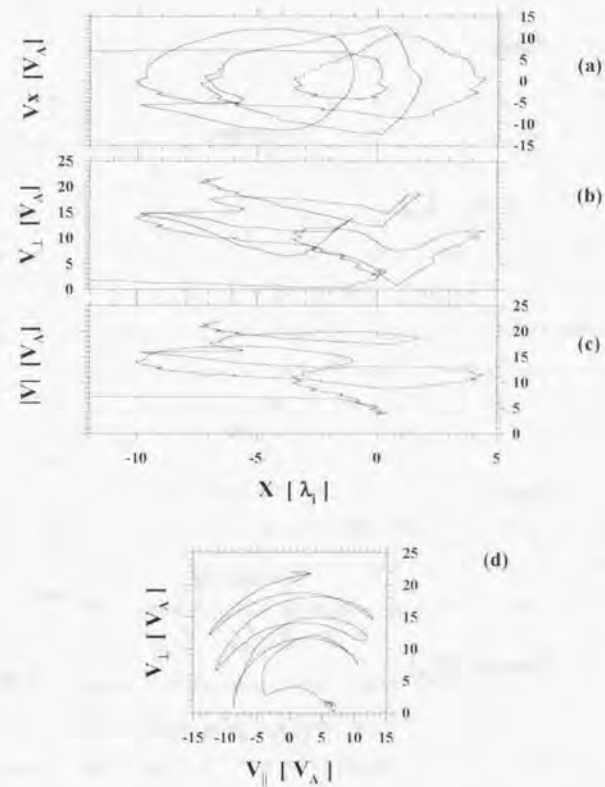


Figure 4-6. Orbit for the same ion plotted in Fig. (4-5a) and (4-5b) versus position relative to shock. Positive directs to downstream direction. From top to bottom, nearly parallel velocity v_x (Panel (a)), perpendicular velocity $v_{\perp} = (v_y^2 + v_z^2)^{1/2}$ (Panel (b)), and total velocity $|v|$ (Panel (c)) are shown. Motion in velocity space (v_{\parallel}, v_{\perp}) is shown in Panel (d). Trajectory is plotted between $\Omega_i t = 60 \sim 80$. Ion velocity is calculated in the shock frame. The parallel velocity is oscillating around $v_{\parallel} = 0$ which leads to cross the shock many times. The ion velocity is mainly increasing in perpendicular direction as shown in Panel (d). These ion motions in velocity space have good agreement with the results from the test particle simulation (compare them with Fig. (3-4) and (3-5)).

from the energy conservation in each wave frame. The shock transition width is too short to apply the adiabatic motion.

Fig. (4-7) shows the ion energies versus intervals while ions are staying in the near shock region. The energy is calculated when an ion is injected over $12 \lambda_i$ upstream ($10 \lambda_i$ downstream) from the shock surface between $\Omega_i t = 70$ and 100 , and normalized by incoming fluid energy in shock frame (E_0). Closed (open) circles show the ions which are eventually injected to the upstream (downstream) region. Note that the intervals are stacked every $\pi \Omega_i^{-1}$. Most accelerated ion gets $\sim 25 E_0$ within only 8π (4 times gyration) intervals.

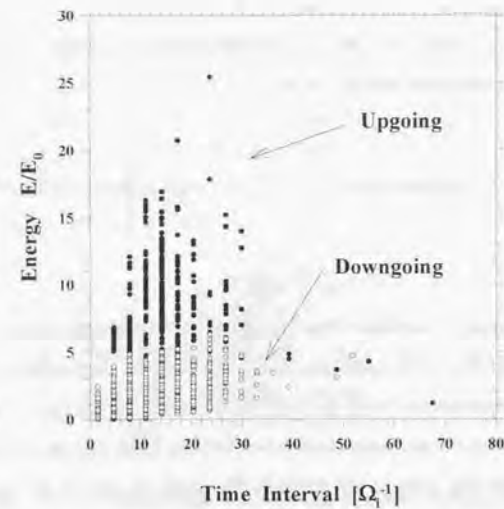


Figure 4-7. The particle energies versus intervals staying in the near shock region. The energy ($v^2 / 2$) is calculated when the ion crosses at $12 \lambda_i$ upstream for upgoing ions (closed circles) or $10 \lambda_i$ downstream for downgoing ion (open circles) and the energy is normalized by ($E_0 = M_{As}^2 / 2$). The upgoing ions are more accelerated than downgoing ions. Most accelerated particle gets $\sim 25 E_0$ within only 8π (4 times gyration) intervals.

Here we compare the acceleration time scale with the DA process by the following estimation. In the DA process, the particle spatial intensity decreases exponentially from the shock surface to upstream region. By a least square fitting method for the density profile in upstream region, shown in Fig. (4-8a), we can obtain diffusion coefficient D in Eq. (A.3) as

$$D = (5.6 \pm 0.5) 10^2 V_A^2 / \Omega, \quad (4.6)$$

in the simulation parameters and as

$$D = (2.9 \pm 0.2) \left(\frac{B_{sw}}{5 [nT]} \right) \left(\frac{N_{sw}}{5 [cc]} \right)^{-1/2} 10^{12} [m^2 / s] \quad (4.7)$$

in the upstream parameters of earth's bow shock, where B_{sw} and N_{sw} are solar wind field intensity and density

Next we estimate required time scale (Δt) for DA process. According to the standard DA theory, the average acceleration rate is given as,

$$\frac{\Delta v}{\Delta t} = \frac{r-1}{3r} \frac{U_1^2}{D} v \quad (4.8)$$

where r is the shock compression ratio (e.g. *Blandford and Ostriker*, [1978]). When $r = 4$, we get

$$\frac{\Delta v}{\Delta t} = \frac{U_1^2}{4D} v \quad (4.9)$$

Using obtained diffusion coefficient D in Eq. (4.6), the time profile of ion acceleration is plotted in Fig. (4-8b) which is the same plot as Fig. (4-7) but for total velocity $|v|$. Solid thick curve shows the acceleration time scale from the DA process using Eq. (4.9). The acceleration processes working in hybrid simulation increase ion velocity faster than the DA process. If we adopt the acceleration time scale as dot curve in Fig. (4-8b) in term of the DA process, the diffusion coefficient D must be greater as explained by dot line in Fig. (4-8a).

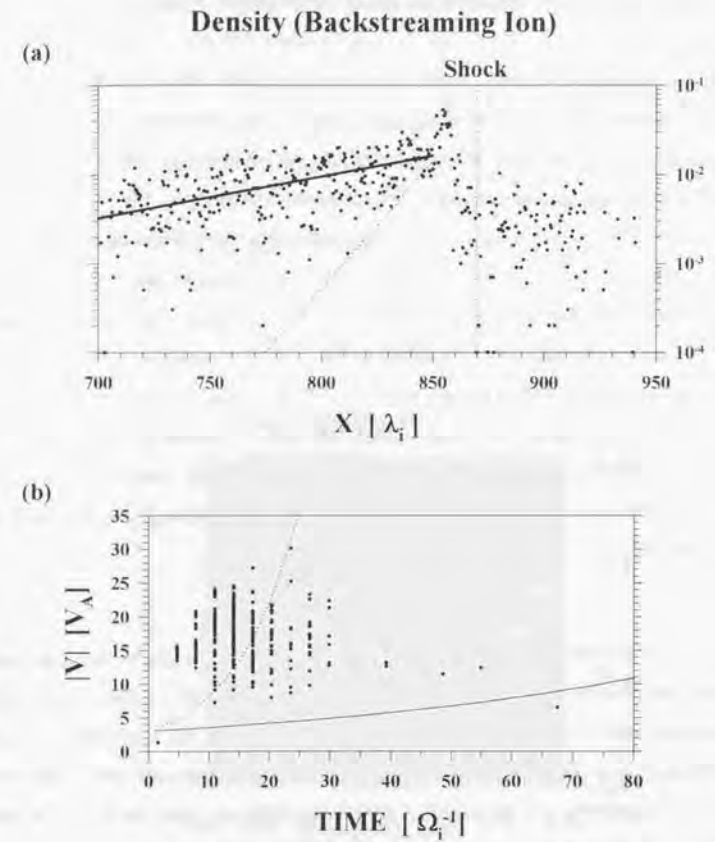


Figure 4-8. Density profile of upstream backstreaming ions (Panel (a)). Dots show the density and vertical dot line shows defined shock position. By least square fitting method, the density profile is fitted by exponential function (Eq. A.3) and shown by solid line. Panel (b) shows acceleration time in the same format as Fig. (4-7) but for velocity. Solid curve shows the estimated time scale of usual diffusive acceleration process using fitting results in solid line in Panel (a) using Eq. (4.9). If the time scale has dotted curve shown in Panel (b), the density profile of backstreaming ions have to decrease as dotted line in Panel (a).

4.3.3 Particle Distribution in the Pitch Angle Space

In Chapter 2, we have reported the pitch angle distributions of the diffuse ions in the upstream region and their relation with the upstream waveforms, that are, circularly polarized wave and linear polarized wave. In this section, we show the pitch angle distributions of the backstreaming ions and waveforms obtained in the present simulations.

First we show the characteristics of the upstream waves. Fig. (4-9) shows the wave spectrum of the magnetic field data in (ω, k) space. The field data are stored in bins of $0.5 \lambda_i$ and $0.1 \Omega_i^{-1}$ and transformed into incoming beam (solar wind) frame. The two transverse components (B_y and B_z) are decomposed into four polarization/propagation modes ($R+$, $R-$, $L+$ and $L-$) through the two-dimensional fast Fourier transforms. R (L) means right (left) hand polarized wave, and $+$ ($-$) sign means the wave propagating to the shock (upstream) direction. Intensity is displayed on a logarithmic color scale from $10^{-4.5}$ to $10^{-2.5}$. Noise level is below 10^{-5} . The solid green curves show the dispersion relation of circularly polarized waves (Whistler and ion cyclotron waves).

$$k^2 = \frac{\omega^2}{1 \pm \omega} \quad (4.10)$$

From the clearly identified spectrum form, the upstream waves show mainly monochromatic right-hand polarization and they propagate upstream direction with nearly Alfvén velocity in the incoming beam frame. Since the incoming beam is super-Alfvénic, the waves are convected toward the shock and observed in $L+$ in the shock frame by Doppler-shift effect. The wave number ~ 0.1 is consistent with the maximum growth rate of the ion beam instability. The wave amplitude in real space is about 0.6 with normalized by the upstream ambient magnetic field intensity (see Fig. (4-2)).

Fig. (4-10) shows color contour plots of the phase space density in the $V_x - V_y$ velocity plane at $\Omega_i t = 100$ in the two different region. The contour level is in arbitrary logarithmic unit. The distributions are averaged in the selected region. Each bin size is 2×2 in Alfvén velocity unit. White line in each panel shows initial magnetic field direction and red line shows averaged magnetic field direction in the selected region. In the far upstream region $200 \sim 400 \lambda_i$ away from the shock (Panel (a)), the distribution of the backstreaming ions is beam-like type.

These beam ions excite the upstream waves. Note that the nearly circular high density distribution at $V_x \sim 4.5$ is the incoming beam ion. In the near upstream region $10 \sim 100 \lambda_i$ away from the shock (Panel (b)), the distribution is not isotropic but 'mushroom' type. Panel (c) is the same as Panel (b) but excluding the incoming ions. The characteristics of distribution are the same as the observational results in the following points, (1) The cap part is well scattered ellipse distribution. (2) The stem part consists of incoming (solar wind) ions. (3) Returning hemisphere is clearly cut off.

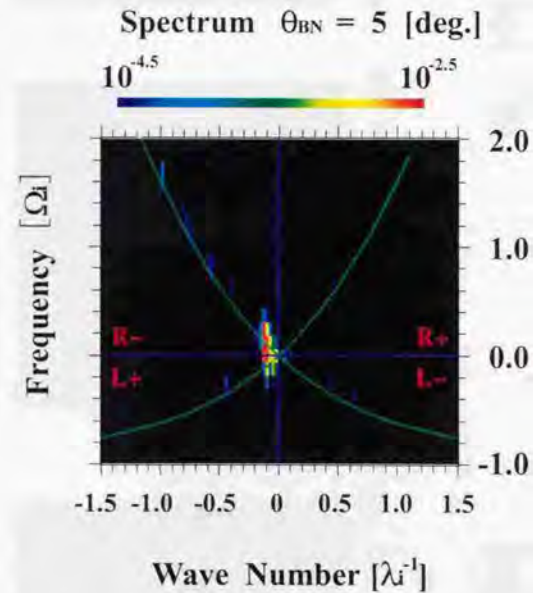


Figure 4-9. Two dimensional spectrum in wave frequency (ω) and wave number (k) plane. This is plotted in the incoming plasma frame. Each quadrant shows the wave polarity and propagating direction. R (L) means right (left) hand polarized waves. $+$ ($-$) means downstream (upstream) propagating waves. Green curves show the dispersion relation of circularly polarized waves (Whistler and ion cyclotron waves). Strong monochromatic right-hand polarized waves are observed around $k \sim 0.1$.

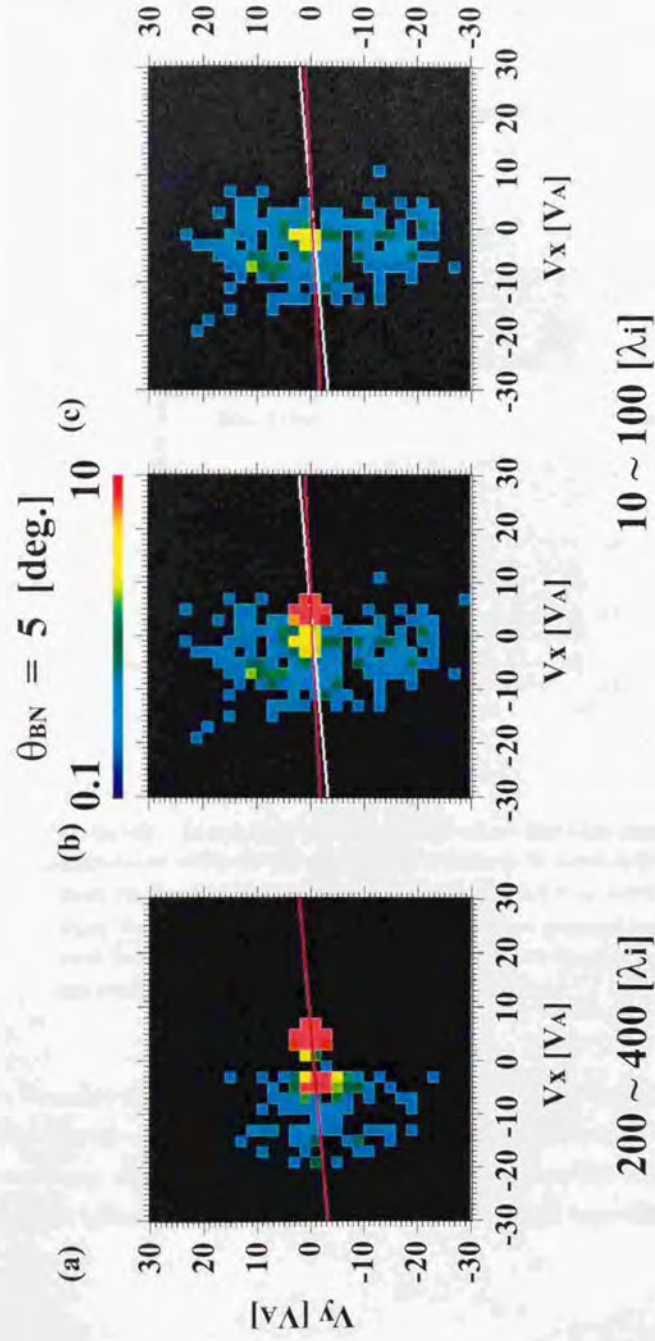


Figure 4-10. Color contour plots of the phase space density in the $V_x - V_y$ velocity plane at $\Omega_e t = 100$ in the two different regions. The distributions are averaged in the selected region. Each bin size is 2×2 in Alfvén velocity unit. White line in each panel shows initial magnetic field direction and red line shows averaged magnetic field direction in the selected region. Plotted are in the far upstream region $200 \sim 400 \lambda_i$ away from the shock (Panel (a)) and in the near shock region $10 \sim 100 \lambda_i$ (Panel (b) and (c)). Panel (c) is the same as Panel (b) but excluding the incoming particles. Density are coordinated by the color scale shown upper bar in logarithm scale. The high density population at $V_x \sim 4.5$ is incoming ions (Panel (a) and (b)). Even in the near shock region, the distribution is 'mushroom' type.

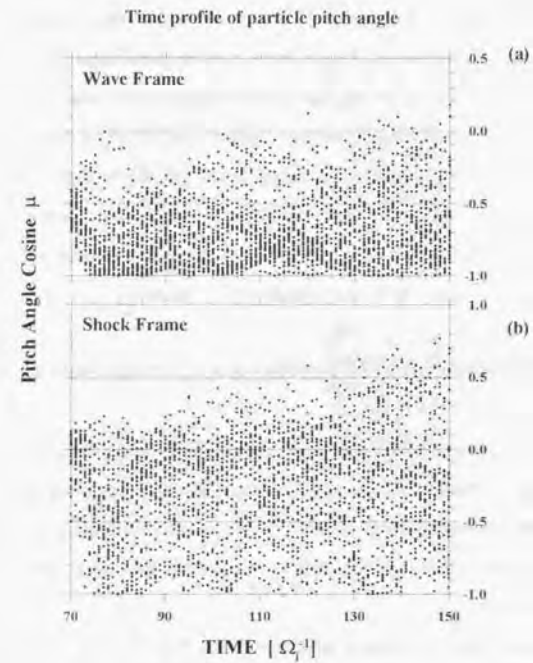


Figure 4-11. Time profile of pitch angle for selected ions. Ions which satisfy following conditions are selected: At time $\Omega_i t = 70$, (1) They are in $100 \sim 200 \lambda_i$ away from the shock. (2) They have their pitch angle cosine (μ) within $-0.7 < \mu < -0.6$ in the wave frame. The time proceeding of these selected ions' pitch angle are plotted in the wave and shock frame. The negative μ means that the parallel velocity directs to upstream. The ions seem to be limited in negative region ($\mu < 0$) in wave frame.

To explain the pitch angle scattering feature in time, Fig. (4-11) shows the time profile of pitch angle for some selected ions in the pitch angle cosine (μ) versus time plane. Note that the negative μ shows backstreaming ions because ambient magnetic field directs +X. The pitch angle (μ) is calculated in the upstream wave frame (incoming beam velocity $V_{in} +$ Alfvén

Velocity V_A) and shock frame (nearly equal with satellite observation frame). The selected ions have their pitch angle cosine (μ) within $-0.7 \leq \mu < -0.6$ in the wave frame at time $\Omega_i t = 70$ in $100 \sim 200 \lambda_i$ away from the shock. These selected ions are pitch angle changed only in a region of negative μ (Panel (a)) which results in constructing mushroom type distribution. The extension width ($\mu < 0$) is consistent with the results in Fig. (2-15). Even in the self-consistent simulation, the pitch angle scattering is limited in the half hemisphere. This is because the excited upstream wave shows nearly monochromatic shape. Since the power of these R+ or L-waves which scatter the ions extending to positive μ range, are as weak as a white noise level, the 'mushroom' distribution is the inherent result in this simulation.

4.3.4 Wave Steepening Phenomena and Distribution Type

To isotropize the upstream diffuse ion distribution, the linear polarized waves which are constructed by the co-existence of R- and L- waves are needed as investigated in Chapter 2. The well discussed exciting process of linear waves is wave steepening process [Omidi and Winske, 1990; Scholer, 1993]. In this section we present the wave steepening phenomena observed in simulations.

First we show the time proceeding of upstream waves. Fig. (4-12) shows the time profiles of y-component B_y (top) and field intensity $|B|$ (bottom) versus X for a part of the system. These profiles are plotted from $\Omega_i t = 67$ to 85 with time separation $\Omega_i t = 2$ and shock positions are plotted by thick line. As mentioned in the section 4.2, our simulations are performed in downstream frame, the created shock is leftward propagating. The upstream waves show always sinusoidal waveform and are convected to the shock. The field intensity is almost constant in the upstream region, which shows that there are no steepening edges.

Next we show the same plot for oblique propagating waves with upstream parameters, $M_{A1} = 6$, $\theta_{bn} = \theta_{in} = 30^\circ$ and $\beta_1 = 1.0$. Note that the initial magnetic field directs to downstream on the X-Y plane. Fig. (4-13) shows the time profiles of y-component B_y (top) and z-component B_z (bottom) of magnetic field versus X for a part of the system. These profiles are plotted from $\Omega_i t = 65$ to 85 with time separation $\Omega_i t = 2$. In the bottom curve, there are nearly sinusoidal waves in the upstream region (labeled by 1 and 2) with wave length

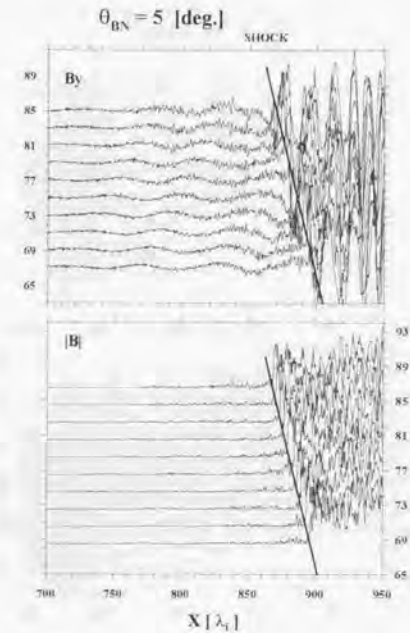


Figure 4-12. Time stack plot of B_y (top), and $|B|$ (bottom). These profiles are plotted from $\Omega_i t = 67$ to 85 with time separation $\Omega_i t = 2$. Thick line in each panel shows shock location defined by the density jump. These waves are right-hand circularly polarized waves with wave length $\sim 50 \sim 60$. The upstream waves are always circularly polarized waves, that is, no steepening wave is seen.

$\sim 50 \sim 60 \lambda_i$. These waves are again right-hand circularly polarized waves. As time elapses, these waves continue to grow in amplitude and steepen at their upstream side. At the end time, the waves form like shocklet structure. The steepening edges are located at ~ 30 and $\sim 70 \lambda_i$ upstream of the shock. Since the distance is much farther than the Larmor radius of the just reflecting ion at the shock surface, it is suggested that the steepening process is not concerned with the shock dissipation process but inherent for the oblique propagating upstream wave.

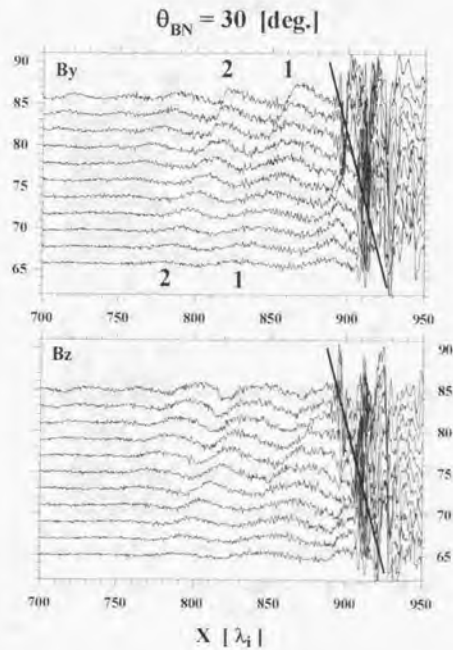


Figure 4-13. Time stack plot of B_y (top), and B_z (bottom) from run of $\theta_{BN} = \theta_{0k} = 30^\circ$ in the same format as Fig. (4-12). The labeled crests in B_y component steepened at their upstream side and at the end time the waves form like shocklet structure.

As known, the initially excited waves in upstream region are fast-mode wave which is concerned with a whistler wave, so that, the compressional components can steepen if the propagating direction is not parallel to the ambient magnetic field. Fig. (4-14) shows the B_y and B_z profiles at $\Omega_1 t = 95$ after the Fig. (4-13). In the downstream (right) side of the steepening region (e.g. between 840 and 860 λ_i), the wave characteristics have changed from circularly polarized wave to another. In contrast to the gradual decreasing of B_y component, B_z is nearly

constant which is also shown in the hodogram of B_y and B_z in lower right Panel, and we see the waveform is linear polarized form. As expected, the linear polarized waves are excited in the upstream region. This linear polarized waveform is seen in wave spectrum in Fig. (4-15) in the same format of Fig. (4-9). Again there are strong R^+ waves, and also we can see L^- waves near $k_{L^-} \sim -k_R$. On the upstream side of the steepening edge (between 820 and 840 λ_i), there are short-wave-length right-hand-polarized waves whose wave length is $\sim 3 \lambda_i$. This is a whistler waves produced by dispersion effect [Omidi and Winske, 1990, Scholer, 1993].

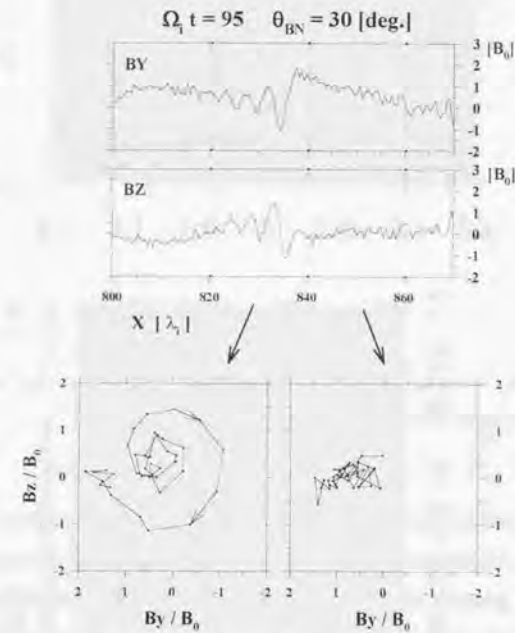


Figure 4-14. Upstream wave form at $\Omega_1 t = 95$ from run of $\theta_{BN} = \theta_{0k} = 30^\circ$ (upper two Panels) and its hodogram (lower two Panels). In the upstream side of the steepening edge, there observed short-wave-length right-hand waves. In the downstream side, these waves shows liner polarized wave form.

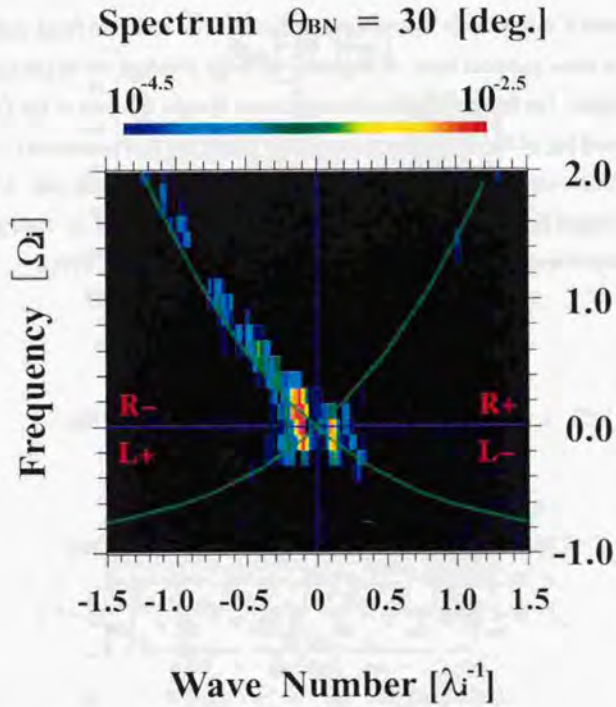


Figure 4-15. In the same format as Fig. (4-9) from run of $\theta_{BN} = \theta_{bk} = 30^\circ$. L- mode is seen in the same wave number as R-.

As explained in Chapter 2, in the linear polarized wave field, the distribution is isotropized by the waves. Fig. (4-16) shows the ion distribution in the $V_x - V_y$ in the same format in Fig. (4-10) in the far upstream region (left) and in the near shock region (right). The data are obtained at $\Omega, t = 92$. Comparing with Fig. (4-10), in the near shock region (right Panel) ions extend to larger pitch angle range and observed as nearly isotropic distribution. On the other hand, in the far upstream region the distribution shows again 'mushroom' type. Fig. (4-17) show density profiles in the pitch-angle space distributions both the $\theta_{bk} = 5.0^\circ$ (upper two Panels) and 30.0° (lower two Panels) case in the upstream wave frame and in the shock

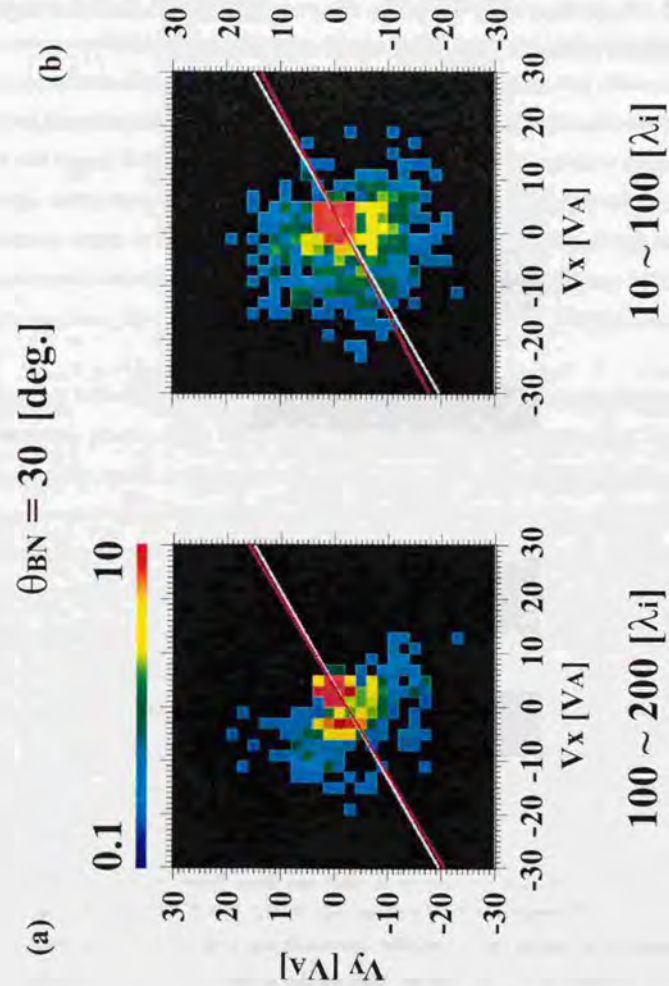


Figure 4-16. In the same format as Fig. (4-10) from run of $\theta_{BN} = \theta_{bk} = 30^\circ$. In this case the distribution in the near shock region is nearly isotropic around the magnetic field. In the far upstream region, it shows 'mushroom' type.

frame. In the larger propagating angle case (lower Panels), the broader distribution in the μ region are seen in both wave and shock frames (lower two Panels). Some ions have $\mu > 0.9$ in the wave frame. The density ratio of the negative μ ions to positive μ is 77.23 in the wave frame and 53.47 in the shock frame. The density of the backstreaming and shock returning ions are well balanced in the shock frame or observational satellite frame.

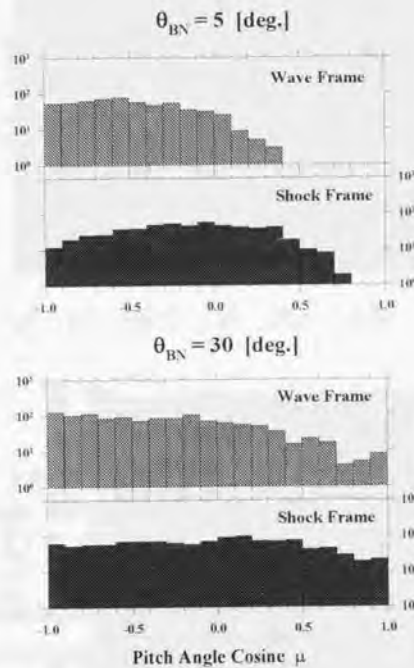


Figure 4-17. Pitch angle distributions in wave and shock frame from two runs in $\theta_{BN} = \theta_{BL} = 5^\circ$ (upper two Panels) and in $\theta_{BN} = \theta_{BL} = 30^\circ$ (lower two Panels). The negative μ means that the parallel velocity directs to upstream. In the small propagating angle case, the distribution is mainly seen in negative region. On the other hand, the large angle case, the distribution is widely extended and nearly isotropic distribution.

4.4 Summary

In one-dimensional hybrid code simulations of the quasi-parallel shocks, we have confirmed the distribution type of backstreaming ions and acceleration feature around the shock as the processes proposed in previous Chapters. Obtained 'mushroom' and nearly isotropic distribution types are determined by the waveform. In the nearly parallel propagating wave case, the wave does not show the steepening feature even in the large amplitude region near the shock, which leads that the ion distribution results in the 'mushroom' type. In the oblique propagating wave case, the waves steepen in the large amplitude region near the shock, which leads that the ion distribution results in the nearly isotropic type, because the steepening change the waveform from circularly polarized form to linear polarized form. In the far upstream region in oblique propagating case, the wave amplitude is too small to steepen, so the distribution is 'mushroom' type.

However, in the linear calculation of the ion beam instability which excite the upstream wave, the maximum growth rate is observed for the parallel propagating wave case. The steepening process hardly occurs in real upstream region. But *Hada et al.* [1987] has shown that the upstream waves are refracted into the zone where diffuse ions are observed. This result leads that the wave vector changes more oblique. On the other hand, *Scholer et al.* [1992] has shown in their two-dimensional shock simulation, the upstream waves are refracted from shock normal direction to ambient magnetic field direction with going to upstream direction. In other words, the oblique-propagating upstream waves are detected near the shock region. From these studies, it may be reasonable to set the oblique-propagation system in the one-dimensional simulation which forces the wave propagation direction to parallel to specific axis X. To investigate how the waves refract from parallel to oblique direction or opposite direction, is beyond present one-dimension simulation.

In self-consistent simulations, the upstream ions also come from a distinct portion of incoming ion population. Whether the ion is reflected and injected to upstream region or transmitted to downstream region is determined its phase angle difference (θ) at the shock surface. It is one of the necessary conditions for reflection process that the angle θ is around π (0) when the ambient field directs to downstream (upstream). This conditions are the same as the results

obtained in test particle simulation. This is mainly because the upstream waves in hybrid simulation also show large amplitude nearly monochromatic circularly polarized shape. The density of RI is expected to be determined by the temperature of incoming solar wind ion because the distribution width in the phase angle space (Fig. (4-3a)) around $\theta = \pi$ determines the density of the RI ions. The dependence, however, is not clear in our simulations (not shown) because the incoming ions are pre-heated in front of the shock surface by the instability to excite the upstream wave. When the incoming ions arrive at the shock surface, the temperature is nearly same for each simulation parameter (β).

Ion energy increases while they are staying near the shock region. The acceleration time scale is faster than the diffusive acceleration process. The velocity mainly increases in perpendicular direction. The ion trajectories in both real space and velocity space resemble with the results from test particle simulations.

Chapter 5

Conclusion

We have investigated the ion dynamics around the quasi-parallel shock region, especially the ion acceleration/scattering processes occurring at the earth's bow shock and its upstream region. Comparing the statistical analysis of observational data with the results from the numerical simulations, the importance of the ion motion in the large amplitude waves is found.

In the large amplitude nearly monochromatic wave field, the importance of the resonance type pitch angle scattering process is weak, so that, all ion motion can be determined by the scatter-free process. In this circumstance, it is a good analytical method that individual particle trajectories are numerically calculated in given wave field configuration. From this concept, we have performed test particle simulations to investigate the following three topics, (1) pitch angle changing process, (2) reflection process of the incoming solar wind ions at the shock surface, and (3) ion acceleration process around the parallel shock. The predicted motions in the test particle simulations are also confirmed by the self-consistent simulations in hybrid code in Chapter 4.

Chapter 2 has shown an observational summary for the characteristic features of non-thermal ions in the bow shock upstream region. It is shown that these ions most often show an anisotropic pitch angle distribution, occupying only the pitch angle hemisphere in the escaping direction from the shock front. This peculiar pitch angle distribution is explained in terms of the nonlinear trapping motions of ions in nearly monochromatic large amplitude MHD waves. A quantitative comparison between this nonlinear process and the standard quasi-linear pitch angle scattering process is also shown. The contribution of the wave-particle interaction process which is based on the cyclotron resonance process is weak in the earth's upstream region. These two processes are distinct each other. Because in the large amplitude monochromatic wave field, the pitch angle is merely oscillating and is not diffused. On the other

hand, the quasi-linear scenario in the small amplitude wave treats the pitch angle diffusion.

While the nearly isotropic pitch angle distribution is observed in the upstream region near the shock, the half-hemisphere distribution called the 'mushroom' distribution is frequently observed in the far upstream region. These two types of the pitch angle distribution are derived from the difference of the wave form. The circularly polarized waves make the 'mushroom' distribution and the linear polarized waves make the nearly isotropic distribution. Since the linear polarized waves can be excited from large-amplitude oblique-propagating waves by means of the wave steepening effects, the nearly isotropic distribution is frequently observed near the shock.

By applying ion motions in the large amplitude wave field to shock discontinuity we have proposed new acceleration and reflection processes. These processes are derived from the different propagation speed of MHD waves between the upstream and downstream regions of the shock front. It is found that ion motions depend not only on their initial pitch angle but also on their initial gyrophase angle, and that some of ions can be accelerated promptly up to the velocity of $\sim 10 - 20$ times of the upstream Alfvén velocity. This new acceleration mechanism is found to work much shorter time interval (a few gyroperiods) and smaller space (about 10 ion inertia length) than the standard diffusive shock acceleration mechanism does.

We have mentioned that two processes of diffusion and oscillation are distinct each other, but they are not conflict processes. The acceleration process around the shock discontinuity includes the diffusion effect with oscillation process. When the wave field is uniform, the ion motion in the velocity space is merely oscillation, so that the ion backs to the same position in velocity space after the oscillation period. When the ion crosses the shock discontinuity, the ion does not back to the same position in velocity space and the phase angle (θ) shifts to π . This shift may represent the diffusion effect. This is because many kind of waves are restricted in the shock transition layer, that is, non-monochromatic wave space. But this diffusion motion is not derived from the stochastic scattering process. The transition layer is exactly determined in our simulations.

The reflection mechanism proposed in Chapter 3 contributes to solve the "injection problem" which relates to an important question, how to produce nonthermal ions from thermal ions at astrophysical shocks. Because this process explains the production process of non-thermal diffuse ions from solar wind thermal ion population. A restrict portion of the incoming solar

wind population is reflected, accelerated and injected to the upstream region. The portion is determined mainly by the gyrophase angle.

Future works

The acceleration and reflection processes performed near the parallel shock region, however, can not describe the motions of He^{++} particles. The energy increasing shows the nearly consistent value, but most of the incoming He^{++} are not reflected and injected to the upstream region but transmitted to downstream region. When the wave length is larger than that in present case, He^{++} can be reflected, which suggests that there is a comfortable wave length for He^{++} . If there is He^{++} backstreaming beam in the upstream region, larger wave length upstream waves are excited by the same instability as proton. Recently GEOTAIL have observed such high dense He^{++} beam in the upstream region of bow shock. We set these investigation remained unsolved study.

Present simulation results are restricted in 1-dimensional case. Since the waveform strongly depends on the wave propagating angle, multi-dimensional simulation brings us important information about wave and ion distribution shape. In addition, the curved shock simulation shows the dependence on the distance from shock including the shock angle and convection effects. On the other hand, there is less modulation to the shock acceleration process shown in this thesis, even if curved shock simulation is performed. Because the displacement of ion motion in shock tangential plane is the same order of the ion Larmor radius. The curvature of the earth's bow shock is larger than ion Larmor radius. But in the other small planets, like Mars, the curvature effects sensitive modulation to ion motions.

Appendix A

Diffusive Shock Acceleration Process

A.1 Diffusion Convection Equation

When the particle mean free paths are short, it is possible to treat the spatial transport with the diffusion approximation. The diffusion-convection equation has been used to explain the spatial and energy spectrum of the suprathermal particles [Axford *et al.*, 1977; Bell, 1978a,b; Jones and Ellison, 1991 and references therein],

$$\frac{\partial f}{\partial t} + \nabla \cdot (\mathbf{U} f - \mathbf{D} \nabla f) - \frac{1}{3} (\nabla \cdot \mathbf{U}) \frac{\partial}{\partial v} (v f) = 0 \quad (\text{A.1})$$

which results from transport of the distribution function $f(x, v, t)$ under the assumption that f is nearly isotropic. We use a spatial coordinate x in the frame where the shock is located at $x = 0$. The fluid velocity is given by U_1 (U_2) for upstream $x < 0$ (downstream $x > 0$). In the steady state with $\nabla \mathbf{U} = 0$ the Eq. (A.1) for the suprathermal distribution is

$$U \frac{\partial f}{\partial x} = D \frac{\partial^2 f}{\partial x^2} \quad (\text{A.2})$$

where we assume that the diffusion coefficient D does not depend on x . This equation is easily integrated in the upstream region ($x < 0$) under the boundary condition that $f(-\infty) = f_\infty$ and f_0 at the shock front,

$$f_1(x) = f_\infty + (f_0 - f_\infty) \exp\left(\frac{U_1}{D} x\right) \quad (\text{A.3})$$

The particle intensity decreases exponentially from the shock surface.

When the shock surface is curved shape like the Earth's bow shock, a possible escape route which is diffusion off to the side of the shock is included [Eichler, 1981]. For simplicity shock is defined by a square plane at $x = 0$ within $-a < y < a$, $-a < z < a$. It is reasonable from Eq. (A.3) to

assume that in the upstream region the distribution function f is described as

$$f(x, y, z, E) = g(E) \exp(k_1 x) \cos\left(\frac{\pi y}{2a}\right) \cos\left(\frac{\pi z}{2a}\right) \quad (\text{A.4})$$

where E is particle energy and k_1 is the solution of

$$-U k_1 + D_1 k_1^2 - 2D_2 \left(\frac{\pi}{2a}\right)^2 = 0 \quad (\text{A.5})$$

Integrating Eq. (A.2) from $x = 0^-$ to $x = 0^+$ with Eqs. (A.4), (A.5) and using jump condition at the shock $\partial U / \partial x = (U_2 - U_1) \delta(x)$ we obtain,

$$\frac{2}{3} (U_2 - U_1) \frac{\partial g}{\partial \ln E} = \frac{\pi}{a} (2D_1 D_2)^{1/2} g \quad (\text{A.5})$$

Since $(2D_1 D_2) \propto E^2$,

$$g(E) \propto \exp(-E / E_c) \quad (\text{A.6})$$

where E_c is a characteristic energy. The energy spectrum of the upstream ions is described by exponential form.

Another theoretical approach for exponential spectrum is given by Lee *et al.*, [1981]. They included the energy dependence of the diffusion coefficient on particle energy, that is,

$$D_i \propto \frac{E}{q} \quad (\text{A.8})$$

where q is particle charge. This assumption is reasonable when the particle mean-free path is proportional to particle rigidity. They have shown the exponential spectrum of the diffuse ion.

A.2 Particle Interaction with Alfvén Wave

To use above diffusion approximation, the distribution function f must be nearly isotropic in velocity space. To construct the isotropic ion distribution, the wave-particle cyclotron resonant interaction is considered important.

Here we consider the pitch angle scattering rate of ion from Alfvén waves which is traveling

in one direction along the ambient magnetic field [Blandford and Eichler, 1987]. Alfvén wave frequency in the plasma rest frame is below the proton gyro frequency, $\Omega_i = eB / m$. Suprathermal ions traveling faster than Alfvén speed see the waves as magnetostatic disturbance. Since the waves are circularly polarized, there is a possible resonant interaction which results in a change in the particle's pitch angle θ_p . We transform to the wave frame where the electric field vanishes. We set the Alfvén waves as monochromatic circularly polarized waves with small amplitude B_w perpendicular to ambient magnetic field B_0 . The particle energy is conserved and so the pitch angle changes according to

$$mv \frac{d\mu}{dt} = e(\mathbf{v}_1 \times \mathbf{B}_w) \quad (\text{A.9})$$

where μ is pitch angle cosine $\mu = \cos(\theta_p)$ and \mathbf{v}_1 is perpendicular component of particle velocity. The right hand side is written as,

$$mv \frac{d\mu}{dt} = ev(1 - \mu^2)^{1/2} B_w \cos[(k\nu\mu - \Omega_i)t + \Phi] \quad (\text{A.10})$$

where Φ is initial phase angle between \mathbf{v}_1 and \mathbf{B}_w , and ion gyrofrequency $\Omega_i = eB_0 / m$. To estimate the pitch angle scattering, we calculate the averaged pitch angle diffusion coefficient $D_{\mu\mu} \equiv \langle \Delta\mu \Delta\mu / \Delta t \rangle$. Using

$$\Delta\mu \Delta\mu = \int_0^t dt' \int_0^{t'} dt'' \left[\frac{d\mu}{dt} \right]_{t'} \left[\frac{d\mu}{dt} \right]_{t''} \quad (\text{A.11})$$

and averaging over Φ , we get

$$\langle \Delta\mu \Delta\mu / \Delta t \rangle = \frac{\Omega_i^2 (1 - \mu^2)}{k\nu\mu - \Omega_i} \sin[(k\nu\mu - \Omega_i)t] \quad (\text{A.12})$$

In the limit $t \rightarrow \infty$,

$$\langle \Delta\mu \Delta\mu / \Delta t \rangle_\infty = \pi \frac{\Omega_w^2}{\nu\mu} \delta\left(k - \frac{\Omega_w}{\nu\mu}\right) \quad (\text{A.13})$$

But here is one important problem in this mechanism. The resonant k -vector increases as the pitch angles approaches 90° . No wave can describe the crossing at $\theta_p = 90^\circ$ in the small amplitude wave amplitude limit, that is, there should be no scattering between forward and

backward hemispheres in phase space. The pitch angle distribution derived from this mechanism does not result in isotropic type. The problem of scattering has been addressed by several authors [e.g. Goldstein, 1976, Jones *et al.*, 1978]. Though a resonance broadening from non-linear effects allow passage through 90° , the nearly monochromatic waves can not isotropize the ion distribution using the resonance process. In this thesis, we have also consider the pitch angle scattering phenomenon in the large amplitude Alfvén wave and found that the wave electric field can change several tens degree of ions' pitch angle within one-gyro motion even though the ions' velocity does not satisfy the cyclotron resonance condition, and the process does not have limitation at 90° .

Appendix B

Phase Bunching Mechanism

Here we consider the ion motion in large amplitude monochromatic Alfvén wave [e.g. Sudan and Ott, 1971; Matsumoto *et al.*, 1974; Hoshino and Terasawa, 1985]. First we consider phase bunching phenomenon in the case where the initial perpendicular velocity v_\perp is larger than parallel velocity v_\parallel and Alfvén velocity. From Eqs. (2.7) ~ (2.9),

$$\frac{d^2\theta}{dt^2} = \Omega v_\perp k \sin \theta \quad (\text{B.1})$$

This is a differential equation with the same form as a pendulum motion which oscillates around $\theta = \pi$ or rotates completely with frequency $\sqrt{\Omega v_\perp k}$. From energy conservation of a pendulum motion

$$\frac{1}{2} \left(\frac{d\theta}{dt} \right)^2 - \Omega v_\perp k \cos \theta = \text{const.} \quad (\text{B.2})$$

Resonant ions with v_\parallel satisfying $|v_\parallel - \omega/k| < 2\sqrt{\Omega v_\perp/k}$ are phase-trapped around $\theta = \pi$ depending on their initial phase angles θ_0 . Ions satisfying $|v_\parallel - \omega/k| > 2\sqrt{\Omega v_\perp/k}$ are rotating all phase regardless of their initial phase angles. Fig. (B-1) shows the time proceeding of phase angle θ for nearly resonant ions (Panel (a)). All ions are oscillating around $\theta = \pi$.

On the other hand, in the case where the initial perpendicular velocity is smaller than parallel velocity, phase angle θ are tightly in $(3/2)\pi$ in short time and its tube rotate around π (Panel (b)).

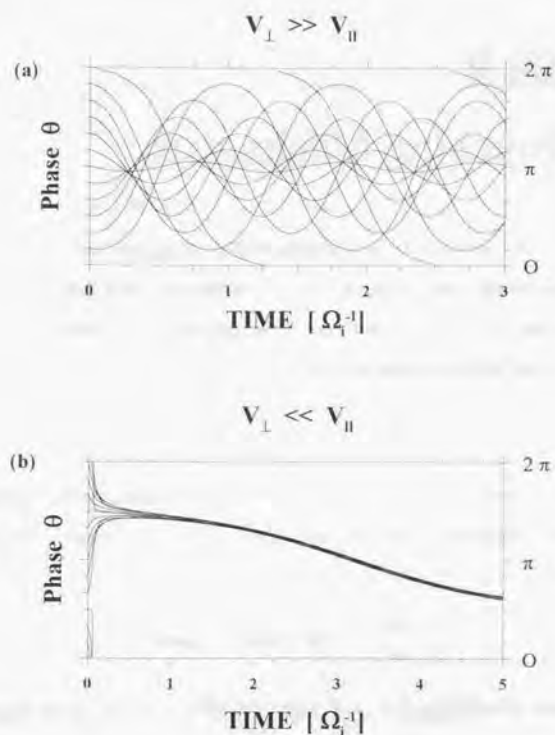


Figure B-1. The time proceeding of phase angle θ for $v_{\perp} \gg v_{\parallel}$ in Panel (a), for $v_{\perp} \ll v_{\parallel}$ in Panel (b). Although all ion is oscillating around $\theta = \pi$ in Panel (a), in Panel (b), phase angle θ is tightly in $(3/2)\pi$ in short time.

Appendix C

Rankine-Hugoniot Relations

Consider a one dimensional plane shock wave propagating steadily with constant speed into a conducting (ionized) fluid (gas). The physical values between shocked (downstream) fluid and un-shocked (upstream) fluid are determined from the conservation law. The relations between two regions are called *Rankine-Hugoniot relation* (here after R-H relation). Suppose that, in a frame moving with the shock, the fluid velocity, its mass density, pressure, magnetic field and shock angle are \mathbf{v} , ρ , P , \mathbf{B} and θ_{sh} . The spatial direction is in X axis parallel to the shock normal vector \mathbf{n} . These values are determined by the equations of *conservation of mass flux*, *momentum flux*, *energy flux*, and Maxwell equations

$$\mathbf{n} \cdot [\rho \mathbf{v}] = 0 \quad (\text{C.1})$$

$$\mathbf{n} \cdot [\rho \mathbf{v} \mathbf{v}] + \mathbf{n} \cdot \left[P + \frac{B^2}{2\mu_0} \right] - \frac{1}{\mu_0} \cdot [\mathbf{B}\mathbf{B}] = 0 \quad (\text{C.2})$$

$$\left[\mathbf{n} \cdot \mathbf{v} \left(\rho \frac{v^2}{2} + \frac{\gamma}{\gamma-1} P + \frac{B^2}{\mu_0} \right) - \frac{1}{\mu_0} (\mathbf{v} \cdot \mathbf{B}) \mathbf{n} \cdot \mathbf{B} \right] = 0 \quad (\text{C.3})$$

$$\nabla \cdot \mathbf{B} = 0 \quad (\text{C.4})$$

$$[\mathbf{E}_{\perp}] = 0 \quad (\text{C.5})$$

where $[]$ show the differences between upstream and downstream side and γ is specific heat. Here we defined another shock parameters, *Alfvén Mach number*, $M_A \equiv v_x / (B_x / \sqrt{\rho\mu_0})$ and ratio of plasma pressure to magnetic pressure $\beta \equiv P / (B^2 / 2\mu_0)$. From the above equations we obtain [Hau and Somnerup, 1989]

$$M_{A1}^2 \rho_1 = M_{A2}^2 \rho_2 \quad (\text{C.6})$$

$$\frac{B_{x1}}{\tan \theta_1} = \frac{B_{x2}}{\tan \theta_2} \quad (\text{C.7})$$

$$(M_{A1}^2 - 1) \tan \theta_1 = (M_{A2}^2 - 1) \tan \theta_2 \quad (\text{C.8})$$

$$M_{A1}^2 + \frac{\beta_1 + 1}{2 \cos^2 \theta_1} = M_{A2}^2 + \frac{\beta_2 + 1}{2 \cos^2 \theta_2} \quad (\text{C.9})$$

$$M_{A1}^2 \left[\frac{\gamma - 1}{\gamma} \frac{(M_{A2}^2 - 1)}{\cos^2 \theta_1} - M_{A2}^2 \tan^2 \theta_1 \left(\frac{\gamma - 1}{\gamma} M_{A2}^2 - 1 \right) \right] =$$

$$M_{A2}^2 \left[\frac{\gamma - 1}{\gamma} \left(\frac{\gamma + 1}{\gamma - 1} - \tan^2 \theta_1 \right) (M_{A2}^2 - 1)^2 + \tan^2 \theta_1 \left(\frac{\gamma - 1}{\gamma} M_{A2}^2 - 1 \right) (M_{A2}^2 - 2) \right] \quad (\text{C.10})$$

$$- \frac{\beta_1}{\cos^2 \theta_1} (M_{A2}^2 - 1)^2$$

where the subscript 1 denotes the component tangential to the shock and the subscript 1 and 2 denote the upstream and downstream values, respectively. The downstream plasma parameters are determined by upstream parameters $(\beta_1, \theta_1, M_{A1})$.

Appendix D

Setting for the Shock Transition Layer and Wave Transmission

D.1 Transition Layer

MHD shock transition profile is determined by following one-dimensional method. Note that only strict parallel shock case: $\theta_{BN} = 0^\circ$ is investigated. Parameters to determine the shock structure are Alfvén Mach number M_A , upstream plasma β_1 , upstream wave length λ_1 and amplitude B_{w1} . Subscript 1 (2) represents upstream (downstream) value. Shock normal direction lies on X axis and shock surface is located at $X = 0$. Upstream (downstream) region is $X < 0$ ($X > 0$). Upstream $U_1 \equiv U(-\infty)$ and downstream $U_2 \equiv U(+\infty)$ conditions of the fluid velocity are calculated by Rankine-Hugoniot relations which are presented in Appendix C. $U(x)$ is connected both side of the shock by tangent hyperbolic function

$$U(x) = \frac{1}{2} (M_A - U_2) \left(1 - \tanh((X - X_0) / E_s) \right) + U_2 \quad (\text{D.1})$$

where E_s is a shock scale length. Density $N(x)$ is calculated by a flux conservation $N(x) U(x) = N_1 U_1$. In the calculated $N(x)$, shock position is transported to $N(x) = 3$ by displacement with X_0 and then $N(x = 0) = 3$ is re-defined by the new shock position. Wave amplitude $B_w(x)$ is defined as next Section (D.2). Alfvén velocity decreases with proportional to $1 / \sqrt{N(x)}$ because of constant B_x . Wave phase velocities are $V_w^\pm(x) = U(x) \pm V_A(x)$. $+$ ($-$) sign shows upstream (downstream) propagating wave. From the decreasing of the fluid velocity $U(x)$, the pseudo wave phase velocities ($V_w^\pm(x)$) in shock frame are different in both side of the shock, V_{w1} for upstream region, V_{w2}^+ for downstream region and $V_{w2}^- < V_{w1}$. Wave number k^\pm is calculated from the wave phase velocity V_w^\pm and constant wave frequency (ω). The circularly polarized waves are described as

$$B_1(x, t) = B_w \cos(kx - \omega t) + B_w' \cos(k'x - \omega t + \phi_s) \quad (\text{D.2})$$

$$B_2(x, t) = B_w \sin(kx - \omega t) + B_w' \sin(k'x - \omega t + \phi_s) \quad (\text{D.3})$$

where ϕ_s is phase difference between upstream and downstream propagating waves at $x = 0$ and $t = 0$. Density and field intensity are normalized by the far upstream value.

D.2 Transmission of Alfvén Waves through a Fast-Mode MHD Shock

A transmission of small amplitude Alfvén wave through a fast-mode MHD shock is calculated on the respect to their amplitude [e.g. McKenzie and Westphal, 1969]. For simplicity the analysis is restricted to Alfvén mode waves with wave vectors \mathbf{k} being parallel to the ambient magnetic field vector \mathbf{B} . And the shock is referred in the normal incidence frame with parallel shock configuration. These formulae lead that \mathbf{k} , \mathbf{B} and incidence flow vector \mathbf{U} are parallel to the shock normal vector \mathbf{n} . The associated downstream waves with upstream monochromatic Alfvén mode wave are propagating to both upstream and downstream direction in the downstream flow frame. Since the downstream flow speed is generally faster than Alfvén speed, both created waves are convected to downstream direction with different phase velocity in the shock frame.

The continuity of tangential momentum and electric field across the shock surface (R-H relations) are written in

$$\left[\rho U_n U_t - \frac{B_n B_t}{\mu_0} \right] = 0 \quad (\text{D.4})$$

$$[U_n B_t - U_t B_n] = 0 \quad (\text{D.5})$$

where in unperturbed state,

$$U_n = U_\infty \quad (\text{D.6})$$

$$\mathbf{U}_t = (0, 0, 0) \quad (\text{D.7})$$

$$B_n = B_\infty > 0 \quad (\text{D.8})$$

$$\mathbf{B}_t = (0, 0, 0) \quad (\text{D.9})$$

and ρ is mass density. When the velocity and magnetic field in the upstream region are perturbed by Alfvén mode wave of $\delta\mathbf{U} = (0, 0, \delta U)$ and $\delta\mathbf{B} = (0, 0, \delta B)$, Eq. (D.4) and (D-5) are

$$\left[\rho U_\infty \delta U - \frac{B_\infty \delta B}{\mu_0} \right] = 0 \quad (\text{D.10})$$

$$[U_\infty \delta B - \delta U B_\infty] = 0 \quad (\text{D.11})$$

and the perturbations are given by Walén relation

$$\delta U^+ = - \frac{\delta B}{\sqrt{\rho \mu_0}} \quad (k > 0) \quad (\text{D.12})$$

$$\delta U^- = + \frac{\delta B}{\sqrt{\rho \mu_0}} \quad (k < 0) \quad (\text{D.13})$$

We consider the perturbations in each side of the shock in terms of their amplitudes, that is, an upstream-propagating upstream-wave with amplitude δB_1 creates downstream/upstream propagating downstream-wave (δB_2^+ , δB_2^-). Substitute Eqs. (D.12) and (D.13) into Eqs. (D.10) and (D.11),

$$\rho_1 U_{x1} \frac{\delta B_1}{\sqrt{\rho_1 \mu_0}} - \frac{B_x}{\mu_0} \delta B_1 = \rho_2 U_{x2} \left(- \frac{\delta B_2^+}{\sqrt{\rho_2 \mu_0}} + \frac{\delta B_2^-}{\sqrt{\rho_2 \mu_0}} \right) - \frac{B_x}{\mu_0} (\delta B_2^+ + \delta B_2^-) \quad (\text{D.14})$$

$$U_{x1} \delta B_1 - \frac{\delta B_1}{\sqrt{\rho_1 \mu_0}} B_x = U_{x2} (\delta B_2^+ + \delta B_2^-) - \left(- \frac{\delta B_2^+}{\sqrt{\rho_2 \mu_0}} + \frac{\delta B_2^-}{\sqrt{\rho_2 \mu_0}} \right) B_x \quad (\text{D.15})$$

and we obtain

$$\frac{\delta B_2^+}{\delta B_1} = \frac{1}{2} \left(1 - \frac{1}{\sqrt{\rho_r}} \right) \frac{U_{x1} - U_{Ax1}}{U_{x2} + U_{Ax2}} \quad (\text{D.16})$$

$$\frac{\delta B_2^-}{\delta B_1} = \frac{1}{2} \left(1 + \frac{1}{\sqrt{\rho_r}} \right) \frac{U_{x1} - U_{Ax1}}{U_{x2} - U_{Ax2}} \quad (\text{D.17})$$

where ρ_r is compressional ratio ($= \rho_2 / \rho_1$) and V_{Ax} is Alfvén speed ($= B_x / \sqrt{\rho \mu_0}$). In the transition layer (using normalized values),

$$\frac{\delta B_2(x)}{\delta B_1} = \frac{1}{2} \left(1 - \frac{1}{\sqrt{N(x)}} \right) \frac{U_1 - 1}{U(x) + V_A(x)} \quad (\text{D.18})$$

$$\frac{\delta B_2(x)}{\delta B_1} = \frac{1}{2} \left(1 + \frac{1}{\sqrt{N(x)}} \right) \frac{U_1 - 1}{U(x) - V_A(x)} \quad (\text{D.19})$$

References

- Anagnostopoulos, G. C., E. T. Sarris, and S. M. Krimingis, Magnetospheric Origin of Energetic ($E \geq 50$ keV) ions Upstream of the Bow Shock: The October 31, 1977, Event, *J. Geophys. Res.*, *91*, 3020-3028, 1986.
- Anagnostopoulos, G. C., A. G. Rigas, E. T. Sarris, and S. M. Krimingis, Characteristics of upstream energetic ($E \geq 50$ keV) ion events during intense geomagnetic activity, *J. Geophys. Res.*, *103*, 9521-9533, 1998.
- Armstrong, T. P., M. E. Pesses, R. B. Decker, Shock Drift Acceleration, in *Collisionless Shocks in the Heliosphere: Review of Current Research*, *Geophys. Monogr. Ser.*, vol. 35, edited by B. T. Tsurutani and R. G. Stone, p. 271, AGU, Washington, D. C., 1985.
- Asbridge, J. R., S. J. Bame, and I. B. Strong, Outward Flow of Protons from the Earth's Bow Shock, *J. Geophys. Res.*, *73*, 5777-5782, 1968.
- Axford, W. I., E. Lear, and G. Skadron, The Acceleration of Cosmic Rays by Shock Waves, *Proc. 15th Int. Cosmic Ray Conf.*, *11*, 132-137, 1977.
- Bell, A. R., The acceleration of cosmic rays in shock fronts 1, *Monthly Notices Roy. Astron. Soc.*, *182*, 147-156, 1978a.
- Bell, A. R., The acceleration of cosmic rays in shock fronts 2, *Monthly Notices Roy. Astron. Soc.*, *182*, 443-455, 1978b.
- Blandford, R. D., and D. Eichler, Particle Acceleration at Astrophysical Shocks: A Theory of Cosmic Ray Origin, *Physics Reports*, *154*, 1-75, 1987.

References

- Blandford, R. D., and J.P.Ostriker, Particle acceleration by astrophysical shocks, *Astrophys. J.*, 221, L29, 1978.
- Bonifazi, C. and G. Moreno, Reflected and Diffuse Ions Backstreaming From the Earth's Bow Shock 1. Basic Properties, *J. Geophys. Res.*, 86, 4397-4404, 1981a.
- Bonifazi, C. and G. Moreno, Reflected and Diffuse Ions Backstreaming From the Earth's Bow Shock 1. Origin, *J. Geophys. Res.*, 86, 4405-4413, 1981b.
- Burgess, D., Simulations of backstreaming ion beams formed at oblique shocks by direct reflection, *Ann. Geophysicae*, 5A, 133-146, 1987a.
- Burgess, D., Shock Drift Acceleration at Low Energies, *J. Geophys. Res.*, 92, 1119-1130, 1987b.
- Burgess, D., Cyclic behavior at quasi-parallel collisionless shocks, *Geophys. Res. Lett.*, 16, 345-348, 1989a.
- Burgess, D., Ion Distributions and Thermalizations at Perpendicular and Quasi-Perpendicular Supercritical Collisionless Shocks, *J. Geophys. Res.*, 94, 8783-8792, 1989b.
- Decker, R. B., and L. Vlahos, Shock Drift Acceleration in the Presence of Waves, *J. Geophys. Res.*, 90, 47-56, 1985.
- Decker, R. B., and L. Vlahos, Modeling of Ion Acceleration Through Drift and Diffusion at Interplanetary Shocks, *J. Geophys. Res.*, 91, 13,349-13,356, 1986.
- Decker, R. B., Computer Modeling of Test Particle Acceleration at Oblique Shocks, *Space Sci. Rev.*, 48, 195-262, 1988.
- Edmiston J. P., and C. F. Kennel, A parametric survey of the first critical Mach number for a fast MHD shock, *J. Plasma Physics*, 32, part 3, 429-441, 1984.
- Eichler, D., Energetic particle spectra in finite shocks: The earth's bow shock, *Astrophys. J.*, 244, 711-716, 1981.
- Elaoufir, J., A. Mangeney, T. Passot, C. C. Harvey, and C. T. Russell, Large amplitude MHD waves in the Earth's proton foreshock, *Ann. Geophys.*, 8, 297-314, 1990.
- Ellison, D. C., Monte Carlo Simulation of Charged Particles, *Geophys. Res. Lett.*, 8, 991-994, 1981.
- Ellison, D. C., Shock Acceleration of Electrons and Ions in Solar Flares, *Astrophys. J.*, 298, 400-408, 1985.
- Ellison, D. C., E. Möbius, and G. Paschmann, Particle Injection and Acceleration at Earth's Bow Shock: Comparison of Upstream and Downstream Events, *Astrophys. J.*, 352, 376-394, 1990.
- Fairfield, D. H., Bow Shock Associated Waves Observed in the Far Upstream Interplanetary Medium, *J. Geophys. Res.*, 74, 3541-3553, 1969.
- Fairfield, D. H., Average and Unusual Locations of the Earth's Magnetopause and Bow Shock, *J. Geophys. Res.*, 76, 6700-6716, 1971.
- Fermi, E., On the Origin of the Cosmic Radiation, *Phys. Rev.*, 75, 1169-1174, 1949.
- Fujimoto, M., Instabilities in the Magnetopause Velocity Shear Layer PhD thesis, Institute of Space and Astronautical Science, Kanagawa, Japan, 1992.

References

- Goldstein, M. L., A nonlinear theory of cosmic-ray pitch-angle diffusion in homogeneous magnetostatic turbulence, *Astrophys. J.*, *204*, 900-919, 1976.
- Gosling, J. T., J. R. Asbridge, S. J. Bame, G. Paschmann, and N. Sckopke, Observations of Two Distinct Populations of Bow Shock Ions in the Upstream Solar Wind, *Geophys. Res. Lett.*, *5*, 957-960, 1978.
- Gosling, J. T., M. F. Thomsen, S. J. Bame, W. C. Feldman, G. Paschmann, and N. Sckopke, Evidence for specularly reflected ions upstream from the quasi-parallel bow shock, *Geophys. Res. Lett.*, *12*, 1333-1336, 1982.
- Gosling, J. T., M. F. Thomsen, and S. J. Bame, On the source of diffuse, suprathermal ions observed in the vicinity of the Earth's bow shock, *J. Geophys. Res.*, *94*, 3555-3563, 1989.
- Hada, T., and C. F. Kennel, Nonlinear evolution of slow waves in the solar wind, *J. Geophys. Res.*, *90*, 531-535, 1985.
- Hada, T., C. F. Kennel, and T. Terasawa, Excitation of compressional waves and the formation of shocklets in the Earth's foreshock, *J. Geophys. Res.*, *92*, 4423-4435, 1987.
- Hau, L.-N., and B. U. Ö. Sonnerup, On the structure of resistive MHD intermediate shocks, *J. Geophys. Res.*, *94*, 6539-6551, 1989.
- Hoppe, M. M., C. T. Russell, L. A. Frank, T. E. Eastman, and E. W. Greenstadt, Upstream hydromagnetic waves and their association with backstreaming ion populations: ISEE 1 and 2 observations, *J. Geophys. Res.*, *86*, 4471-4492, 1981.
- Hoshino, M., and T. Terasawa, Numerical study of the upstream wave excitation mechanism, I. Nonlinear phase bunching of beam ions, *J. Geophys. Res.*, *90*, 57-64, 1985.

- Ipavich, F. M., A. B. Galvin, G. Gloeckler, M. Scholer, and D. Hovestadt, A statistical survey of ions observed upstream of the Earth's bow shock: Energy spectra, composition, and spatial variation, *J. Geophys. Res.*, *86*, 4337-4342, 1981a.
- Ipavich, F. M., M. Scholer, and G. Gloeckler, Temporal development of composition, spectra, and anisotropies during upstream particle events, *J. Geophys. Res.*, *86*, 11,153-11,160, 1981b.
- Ipavich, F. M., J. T. Gosling, and M. Scholer, Correlation between the He/H ratios in the upstream particle events and in the solar wind, *J. Geophys. Res.*, *89*, 1501-1507, 1984.
- Jones, F. K., D. C. Ellison, The plasma physics of shock acceleration, *Space Sci. Rev.*, *58*, 259-346, 1991.
- Jones, C. J., T. J. Birmingham, and T. B. Kaiser, Partially averaged field approach to cosmic ray diffusion, *Phys. Fluids*, *21*, 347-360, 1978.
- Kan, J. R., and D. W. Swift, Structure of quasi-parallel bow shock: Results of numerical simulations, *J. Geophys. Res.*, *88*, 6919-6925, 1983.
- Kokubun, S., T. Yamamoto, M. H. Acuña, K. Hayashi, K. Shiokawa, and H. Kawano, The GEOTAIL magnetic field experiment, *J. Geomag. Geoelectr.*, *46*, 7-21, 1994.
- Krauss-Varban, D., and N. Omidi, Structure of medium Mach number quasi-parallel shocks: Upstream and downstream waves, *J. Geophys. Res.*, *96*, 17,715-17,731, 1991.
- Kucharek, H., and M. Scholer, Origin of diffuse superthermal ions at quasi-parallel supercritical collisionless shocks, *J. Geophys. Res.*, *96*, 21,195-21,205, 1991.

References

- Lee, M. A., G. Skadron, and L. A. Fisk, Acceleration of energetic ions at the Earth's bow shock, *Geophys. Res. Lett.*, *8*, 401-404, 1981.
- Lee, M. A., Coupled Hydromagnetic Wave Excitation and Ion acceleration Upstream of the Earth's Bow Shock, *J. Geophys. Res.*, *87*, 5063-5080, 1982.
- Leroy, M. M., D. Winske, C. C. Goodrich, C. S. Wu, and K. Papadopoulos, The Structure of Perpendicular Bow Shocks, *J. Geophys. Res.*, *87*, 5081-5094, 1982.
- Leroy, M. M., Structure of perpendicular shocks in collisionless plasma, *Phys. Fluids*, *26*, 2742-2753, 1983.
- Lin, R. P., C. -I. Meng, and K. A. Anderson, 30- to 100-keV Protons Upstream From the Earth's Bow Shock, *J. Geophys. Res.*, *79*, 489-498, 1974.
- Lyu, L. H., and J. R. Kan, Ion Leakage, Ion Reflection, Ion Heating and Shock-Front Reformation in a Simulated Supercritical Quasi-Parallel Collisionless Shock, *Geophys. Res. Lett.*, *17*, 1041-1044, 1990.
- Lyu, L. H., and J. R. Kan, Ion Dynamics in High-Mach-Number Quasi-Parallel Shocks, *J. Geophys. Res.*, *98*, 18,985-18,997, 1993.
- Matsumoto, H., K. Hashimoto, and I. Kimura, Two Types of Phase Bunching in the Whistler Mode Wave-Particle Interaction *J. Geomag. Geoelectr.*, *26*, 365-383, 1974.
- McKenzie, J. F., K. O. Westphal, Transmission of Alfvén Waves through the Earth's Bow Shock, *Planet. Space. Sci.*, *17*, 1029-1037, 1969.

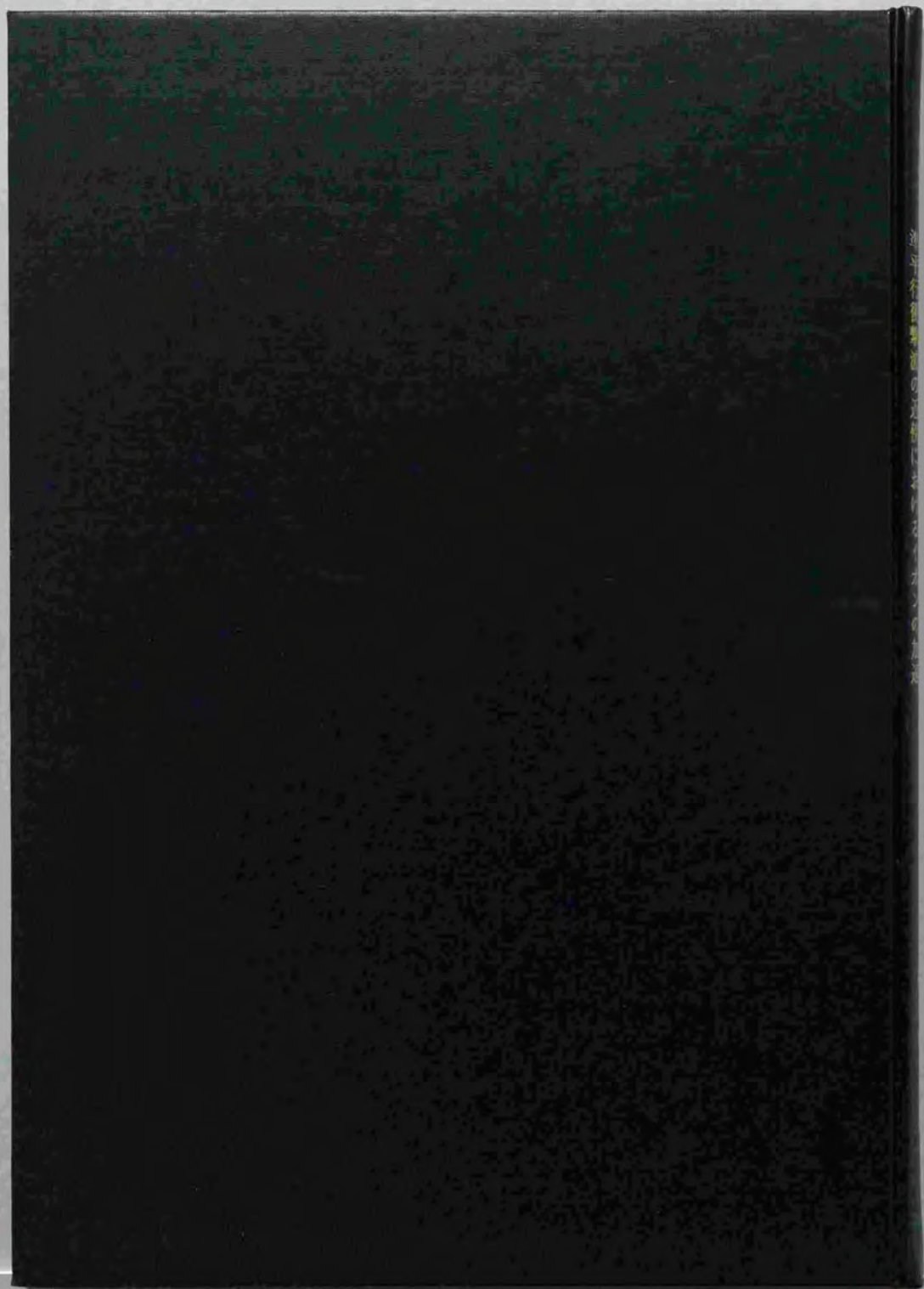
- Möbius, E., D. Hovestadt, B. Klecker, M. Scholer, F. M. Ipavich, C. W. Carlson, and R. P. Lin, A Burst of Energetic O⁺ Ions During an Upstream Particle Event, *Geophys. Res. Lett.*, *13*, 1372-1375, 1986.
- Mukai, T., S. Machida, Y. Saito, M. Hirahara, T. Terasawa, N. Kaya, T. Obara, M. Ejiri, and A. Nishida, The Low Energy Particle (LEP) Experiment Onboard the GEOTAIL Satellite, *J. Geomag. Geoelectr.*, *46*, 669-692, 1994.
- Ness, N. F., C. S. Seearce, and J. B. Seek, Initial Results of the Imp 1 Magnetic Field Experiment, *J. Geophys. Res.*, *69*, 3531-3569, 1964.
- Omidi, N., and D. Winske, Steepening of Kinetic Magnetosonic Waves Into Shocklets: Simulations and Consequences for Planetary Shocks and Comets, *J. Geophys. Res.*, *95*, 2281-2300, 1990.
- Onsager, T. G., M. F. Thomsen, J. T. Gosling, S. J. Bame, and C. T. Russell, Survey of Coherent Ion Reflection at the Quasi-Parallel Bow Shock, *J. Geophys. Res.*, *95*, 2261-2271, 1990.
- Pantellini, F. G. E., A. Heron, J. C. Adam, and A. Mangeney, The Role of the Whistler Precursor During the Cyclic Reformation of a Quasi-Parallel Shock, *J. Geophys. Res.*, *97*, 1303-1311, 1992.
- Paschmann, G., N. Scokopke, J. R. Asbridge, S. J. Bame, and J. T. Gosling, Energization of solar wind ions by reflection from the earth's bow shock, *J. Geophys. Res.*, *85*, 4689-4693, 1980.
- Paschmann, G., N. Scokopke, I. Papamastorakis, J. R. Asbridge, S. J. Bame, and J. T. Gosling, Characteristics of Reflected and Diffuse Ions Upstream From the Earth's Bow Shock, *J. Geophys. Res.*, *86*, 4355-4364, 1981.

References

- Paschmann, G., N. Sckopke, S. J. Bame, and J. T. Gosling, Observations of gyrating ions in the foot of the nearly perpendicular bow shock, *Geophys. Res. Lett.*, *9*, 881-884, 1982.
- Peredo, M., J. A. Slavin, E. Mazur, and S. A. Curtis, Three-dimensional position and shape of the bow shock and their variation with Alfvénic, sonic and magnetosonic Mach numbers and interplanetary magnetic field orientation, *J. Geophys. Res.*, *100*, 7907-7916, 1995.
- Quest, K. B., Theory and Simulation of Collisionless Parallel Shocks, *J. Geophys. Res.*, *93*, 9649-9680, 1988.
- Scholer, M., and T. Terasawa, Ion Reflection and Dissipation at Quasi-Parallel Collisionless Shocks, *Geophys. Res. Lett.*, *17*, 119-122, 1990.
- Scholer, M., Diffuse Ion at a Quasi-Parallel Collisionless Shock: Simulations, *Geophys. Res. Lett.*, *17*, 1821-1824, 1990.
- Scholer, M., and D. Burgess, The Role of Upstream Waves in Supercritical Quasi-Parallel Shock Re-formation, *J. Geophys. Res.*, *97*, 8319-8326, 1992.
- Scholer, M., M. Fujimoto, and H. Kucharek, Quasi-Parallel Shock Re-formation: Two-Dimensional Simulations, *Proc. 26th ESLAB Symp.*, 16-19, 1992.
- Scholer, M., Upstream Waves, Shocklets, Short Large-Amplitude Magnetic Structures and the Cyclic Behavior of Oblique Quasi-Parallel Collisionless Shocks, *J. Geophys. Res.*, *98*, 47-57, 1993.
- Scholer, M., and M. Fujimoto, Low-Mach Number Quasi-Parallel Shocks: Upstream Waves, *J. Geophys. Res.*, *98*, 15,275-15,283, 1993.
- Sckopke, N., G. Paschmann, S. J. Bame, J. T. Gosling, and C. T. Russell, Evolution of Ion Distributions Across the Nearly Perpendicular Bow Shock: Specularly and Non-Specularly Reflected-Gyrating Ions, *J. Geophys. Res.*, *88*, 6121-6136, 1983.
- Sudan, R. N. and E. Ott, Theory of Triggered VLF Emissions, *J. Geophys. Res.*, *76*, 4463-4476, 1971.
- Sugiyama, T., Magnetic Wave and suprathermal Ion Events Observed in the Distant Region Upstream of the Earth's Bow Shock: GEOTAIL and ISEE-3 Observations, Master thesis, Univ. of Tokyo, Tokyo, Japan, 1995.
- Sugiyama, T., T. Terasawa, T. Mukai, Y. Saito, S. Machida, T. Yamamoto, and S. Kokubun, On the Origin of the Upstream Diffuse Ion Case Studies from GEOTAIL Observations, *J. Geomag. Geoelectr.*, *47*, 1141-1145, 1995.
- Thomas, V. A., D. Winske, and N. Omidi, Re-forming Supercritical Quasi-Parallel Shocks I: One- and Two-Dimensional Simulations, *J. Geophys. Res.*, *95*, 18,809-18,819, 1990.
- Trattner, K. J., Upstream Particle Events at the Earth's Bow Shock, PhD thesis, Max-Planck-Institut für Extraterrestrische Physik, Garching, Germany, 1992.
- Trattner, K. J., E. Möbius, M. Scholer, B. Klecker, M. Hilchenbach, and H. Lühr, Statistical analysis of diffuse ion events upstream of the Earth's bow shock, *J. Geophys. Res.*, *99*, 13,389-13,400, 1994.
- Tsurutani, B. T., R. M. Thorne, E. J. Smith, J. T. Gosling, and H. Matsumoto, Steepened Magnetosonic Waves at Comet Giacobini-Zinner, *J. Geophys. Res.*, *92*, 11,074-11,082, 1987.

References

- Winske, D., and M. M. Leroy, Diffuse Ions Produced by Electromagnetic Ion Beam Instabilities, *J. Geophys. Res.*, 89, 2673-2688, 1984.
- Winske, D., and M. M. Leroy, Hybrid Simulation techniques Applied of the Earth's Bow Shock in Computer Simulation of Space Plasmas, ed. by H. Matsumoto and T. Sato, p. 225, Tokyo, Japan, 1985.
- Winske, D., N. Omidí, K. B. Quest, and V. A. Thomas, Reforming supercritical quasi-parallel shocks, 2. Mechanism for wave generation and front re-formation, *J. Geophys. Res.*, 95, 18,821-18,832, 1990.



THE HISTORY OF THE UNITED STATES OF AMERICA

